Study of low energy resonances and β-decay relevant for Nuclear Astrophysics

By

Sathi Sharma

PHYS05201604008

Saha Institute of Nuclear Physics, Kolkata

A thesis submitted to the

Board of Studies in Physical Sciences

In partial fulfillment of requirements

for the Degree of

DOCTOR OF PHILOSOPHY
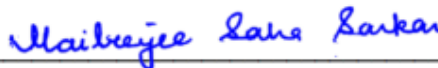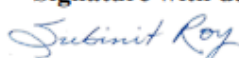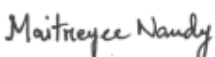
of

HOMI BHABHA NATIONAL INSTITUTE

February, 2021
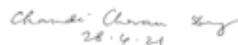
Homi Bhabha National Institute[1]

Recommendations of the Viva Voce Committee

As members of the Viva Voce Committee, we certify that we have read the dissertation prepared by **Sathi Sharma** entitled "**Study of low energy resonances and β-decay relevant for Nuclear Astrophysics**" and recommend that it may be accepted as fulfilling the thesis requirement for the award of Degree of Doctor of Philosophy.

Prof. Supratik Mukhopadhyay	*Supratik Mukhopadhyay* 28 April 2021
Chairman -	**Signature with date**
Prof. Maitreyee Saha Sarkar	*Maitreyee Saha Sarkar* 28/4/2021
Guide / Convener	**Signature with date**
Prof. Chandi Charan Dey	*Chandi Charan Dey 28.4.21*
Co-guide -	**Signature with date**
Prof. Rajdeep Chatterjee	*Rajdeep Chatterjee* 28/4/2021
Examiner -	**Signature with date**
Prof. Subinit Roy	*Subinit Roy* 28.04.2021
Member 1-	**Signature with date**
Prof. Maitreyee Nandy	*Maitreyee Nandy* 29/4/2021
Member 2-	**Signature with date**
Dr. Tumpa Bhattacharjee	Could not attend due to health problem and network issues: Communicated over E-mail
Member 3-	**Signature with date**

Final approval and acceptance of this thesis is contingent upon the candidate's submission of the final copies of the thesis to HBNI.

I/We hereby certify that I/we have read this thesis prepared under my/our direction and recommend that it may be accepted as fulfilling the thesis requirement.

Date: 28/04/2021

Place: SINP, Kolkata

Chandi Charan Dey 28.4.21	*Maitreyee Saha Sarkar 28/4/2021*
Signature	**Signature**
Co-guide (if any)	**Guide**

---

[1] This page is to be included only for final submission after successful completion of viva voce.

STATEMENT BY AUTHOR

This dissertation has been submitted in partial fulfillment of requirements for an advanced degree at Homi Bhabha National Institute (HBNI) and is deposited in the Library to be made available to borrowers under rules of the HBNI.

Brief quotations from this dissertation are allowable without special permission, provided that accurate acknowledgement of source is made. Requests for permission for extended quotation from or reproduction of this manuscript in whole or in part may be granted by the Competent Authority of HBNI when in his or her judgment the proposed use of the material is in the interests of scholarship. In all other instances, however, permission must be obtained from the author.

Sathi Sharma

DECLARATION

I, hereby declare that the investigation presented in the thesis has been carried out by me. The work is original and has not been submitted earlier as a whole or in part for a degree / diploma at this or any other Institution / University.

Sathi Sharma

List of Publications arising from the thesis

Journal

1. Characterization of an electrically cooled BEGe detector till $E_\gamma \sim 7$ MeV, **<u>Sathi Sharma</u>**, Arkabrata Gupta, Balaram Dey, M. Roy Chowdhury, A. Mandal, A. Bisoi, V. Nanal, L. C. Tribedi and M. Saha Sarkar, *Nucl. Instrum. Methods Phys. Res. A*, **2020**, *964*, 163810.

2. Study of ^{14}N(p,γ)^{15}O resonance reaction at E_p^{lab} = 278 keV, **<u>Sathi Sharma</u>**, A. Gupta, S. Das, M. Roy Chowdhury, A. Mandal, A. Bisoi, V. Nanal, L. C. Tribedi and M. Saha Sarkar, *EPJ Web of Conferences*, **2020**, *227*, 02011.

3. Proton capture resonant state of ^{15}O at 7556 keV, **<u>Sathi Sharma</u>**, Arkabrata Gupta, M. Roy Chowdhury, A. Mandal, A. Bisoi, V. Nanal, L. C. Tribedi, M. Saha Sarkar, *Phys. Rev. C*, **2020**, *102*, 024308.

4. Measurement and simulation of gamma-ray background in a low energy accelerator facility, **<u>Sathi Sharma</u>** and M. Saha Sarkar, *JINST*, **2020**, *15*, T09003.

Chapters in books

1. Measurement and simulation of Gamma-Ray Background, **<u>Sathi Sharma</u>**, M. Saha Sarkar, submitted for publication as a short book chapter in CRC press.

Conferences

1. Proton induced reactions of ^{27}Al at low energies, **<u>Sathi Sharma</u>**, Arkabrata Gupta, Sangeeta Das, Anik Adhikari, Yajnya Sapkota, Ananya Das, Rajan Paul, Dibyadyuti Pramanik, Abhijit Bisoi, S. Sarkar, and M. Saha Sarkar, *Proceedings of the DAE-BRNS Symp. on Nucl.*

Phys., **2017**, *62*, 280-281.

2.   Measurement of gamma radiation background in a low energy accelerator facility, **Sathi Sharma**, Sangeeta Das, Arkajyoti De, Sudatta Ray, Prajnaparamita Das, Hitesh Rattan, M. Saha Sarkar, *Proceedings of the DAE-BRNS Symp. on Nucl. Phys.*, **2018**, *63*, 1090-1091.

3. Shell model study of astrophysically important resonant states of ^{15}O, **Sathi Sharma** and M. Saha Sarkar, *Proceedings of the DAE-BRNS Symp. on Nucl. Phys.*, **2019**, *64*, 588-589.

Others

Journal

1. Study of radioactivity built-up and decay with singles time-stamped data, Sangeeta Das, Arkajyoti De, Balaram Dey, **Sathi Sharma**, Anik Adhikari, S. S. Alam, Arkabrata Gupta, Y. Sapkota, Ananya Das, A. Saha, Dibyadyuti Pramanik, T. Bhattacharjee, Abhijit Bisoi, S. Sarkar, M. Saha Sarkar, *JINST*, **2019**, *14*, T09006.

2. Decay spectroscopy of ^{117,118}Sn, Sangeeta Das, Anik Adhikari, S. S. Alam, **Sathi Sharma**, Suman Aich, Arkabrata Gupta, Y. Sapkota, Ananya Das, A. Saha, S. K. Dey, Dibyadyuti Pramanik, Abhijit Bisoi, Indrani Ray, D. Banerjee, Tumpa Bhattacharjee, C. C. Dey, S. Sarkar, M. Saha Sarkar, *Nucl. Phys. A*, **2021**, *1006*, 122079.

3. Interplay between single particle and collective excitation in ^{49}V, Abhijit Bisoi, Y. Sapkota, A. Adhikari, A. Gupta, A. Das, H. Ghosh, R. Rahaman, S. Sarkar, D. Pramanik, S. Das, **Sathi Sharma**, S. Ray, S. Dar, S. Nandi, S. Bhattacharya, T. Bhattacharjee, G. Mukherjee, S. Bhattacharyya, S. Samanta, S. Das, S. Chatterjee, R. Raut and S. S. Ghugre, *J. Phys.: Conf Ser.*, **2020**, *1643*, 012114.

4. Elimination of the effect of internal activity in LaCl3:Ce scintillator, D. Chattopadhyay, **Sathi Sharma**, M. Saha Sarkar, `https://arxiv.org/abs/2006.10496` (Accepted for publication in JINST).

Conferences

1. Decay spectroscopy of ^{118m}Sb, **Sathi Sharma**, Sangeeta Das, S. S. Alam, Arkabrata Gupta, Anik Adhikari, Ananya Das, A. Saha, Dibyadyuti Pramanik, Abhijit Bisoi, Indrani Ray, T. Bhattacharjee, S. Sarkar, M. Saha Sarkar, *Proceedings of the DAE-BRNS Symp. on Nucl. Phys.*, **2017**, *62*, 200-201.

2. Isomers in ^{117,118}Sn and role of neutron $1h_{11/2}$ orbit, Sangeeta Das, **Sathi Sharma**, S.S. Alam, Arkabrata Gupta, Anik Adhikari, Ananya Das, A. Saha, S.K. Dey, Dibyadyuti Pramanik, Abhijit Bisoi, T. Bhattacharjee, C.C. Dey, S. Sarkar, M. Saha Sarkar , *Proceedings of the DAE-BRNS Symp. on Nucl. Phys.*, **2017**, *62*, 84-85.

3. Response of unidirectional grown 1, 3, 5-Triphenylbenzene single crystal in neutron detection, N. Durairaj, Prithvee Nath Pandey, **Sathi Sharma**, Sangeeta Das, Sudatta Ray, R. Kumar, Debasish Saha, C. C. Dey, S. Kalainathan, M. Saha Sarkar, *Proceedings of the DAE-BRNS Symp. on Nucl. Phys.*, **2017**, *62*, 1046-1047.

4. Study of low energy proton capture resonances in ^{14}N, Rajan Paul, **Sathi Sharma**, Sangeeta Das, and M. Saha Sarkar, *Student J. Phys.*, **2017**, *6*, 151.

5. Lifetime measurement of $3/2_1^+$ state of ^{117}Sn, Sangeeta Das, Suman Aich, A. Adhikari, S.S. Alam, **Sathi Sharma**, B. Dey, Arkabrata Gupta, Y. Sapkota, A. Das, A. Saha, S.K. Dey, Dibyadyut Pramanik, D. Banerjee, T. Bhattacharjee, C.C. Dey, Abhijit Bisoi, S. Sarkar, M. Saha Sarkar, *Proceedings of the DAE-BRNS Symp. on Nucl. Phys.*, **2018**, *63*, 270-271.

6. Lifetime measurement of low lying states of ^{27}Si, **<u>Sathi Sharma</u>**, Sangeeta Das, Arkajyoti De, Rashika Gupta, A. Gupta, A. Adhikari, A. Das, Y. Sapkota, A. Saha, S. S. Alam, S. Bhattacharya, R. Banik, S. Nandi, S. Das, S. Samanta, S. Chatterjee, S. Bhattacharyya, B. Dey, D. Pramanik, A. Bisoi, T. Bhattacharjee, M. Nandy, S. Sarkar, M. Saha Sarkar, *Proceedings of the DAE-BRNS Symp. on Nucl. Phys.*, **2018**, *63*, 320-321.

7. Singles time stamped data in In-beam spectroscopy, Sangeeta Das, Arkajyoti De, B. Dey, **<u>Sathi Sharma</u>**, A. Adhikari, S. S. Alam, Arkabrata Gupta, Y. Sapkota, A. Das, A. Saha, Dibyadyuti Pramanik, D. Banerjee, T. Bhattacharjee, Abhijit Bisoi, S. Sarkar, M. Saha Sarkar, *Proceedings of the DAE-BRNS Symp. on Nucl. Phys.*, **2018**, *63*, 1144-1145.

8. Preparation and Characterization of Implanted Targets of ^{16}O and ^{24}Mg for Nuclear Astrophysics experiments, Arkabrata Gupta, Devarani Devi Ksh., G. R. Umapathy, Sunil Ojha, **<u>Sathi Sharma</u>**, Sangeeta Das, Anamika Parihari, Md. Moin Shaikh, Abhijit Bisoi, S. Sarkar, M. Saha Sarkar, *Proceedings of the DAE-BRNS Symp. on Nucl. Phys.*, **2018**, *63*, 320-321.

9. Life-time Measurement of levels in $^{160-162}$Dy nuclei, A. Adhikari, S. Das, S.S. Alam, D. Pramanik, **<u>S. Sharma</u>**, Y. Sapkota, Arkabrata Gupta, Ananya Das, A. Saha, D. Banerjee, T. Bhattacharjee, A. Bisoi, M. Saha Sarkar, S. Sarkar, *Proceedings of the DAE-BRNS Symp. on Nucl. Phys.*, **2018**, *63*, 338-339.

10. Spectroscopy of ^{160,161}Ho, A. Adhikari, D. Pramanik, S. Das, Arkabrata Gupta, Y. Sapkota, Ananya Das, **<u>S. Sharma</u>**, A. De, A. Saha, S.S. Alam, S. Das, S. Samanta, S. Chatterjee, S. Bhattacharya, R. Banik, S. Nandi, R. Raut, S.S. Ghugre, S. Bhattacharyya, G. Mukherjee, T. Bhattacharjee, A. Bisoi, M. Saha Sarkar, S. Sarkar, *Proceedings of the DAE-BRNS Symp. on Nucl. Phys.*, **2018**, *63*, 332-333.

11. Study of nuclear structure in ^{125}I, S. S. Alam, D. Banerjee, T. Bhattacharjee, A. Saha, S. W. Raja, S. Das, A. Adhikari, A. De, A. Gupta, A. Das, Y. Sapkota, **S. Sharma**, S. Dey Chaudhuri, D. Pramanik, A. Bisoi, M. Saha Sarkar, S. Sarkar, *Proceedings of the DAE-BRNS Symp. on Nucl. Phys.*, **2018**, *63*, 356-357.

12. Estimation of Relative Cross-Sections from Activation Analysis, Kshyanaprava Pradhan, Sangeeta Das, **Sathi Sharma**, Dipayan Chattopadhyay, Indrani Ray, M. Saha Sarkar, *Proceedings of the DAE-BRNS Symp. on Nucl. Phys.*, **2019**, *64*, 198-199.

13. Study of ^{24}Mg(p,γ)^{25}Al resonance reaction at lab energy Eplab = 223 keV, Arkabrata Gupta, **Sathi Sharma**, Sangeeta Das, Anik Adhikari, Anubhab Mondal, Madhushree Roy Chowdhury, Chandan D Bagdia, Lokesh Trivedi, Vandana Nanal, Abhijit Bisoi, M. Saha Sarkar, S. Sarkar, *Proceedings of the DAE-BRNS Symp. on Nucl. Phys.*, **2019**, *64*, 606-607.

14. Elimination of the effect of alpha contamination in LaCl3 scintillators by pulse shape discrimination, Dipayan Chattopadhyay, Maitrayee Saha Sarkar, **Sathi Sharma**, *Proceedings of the DAE-BRNS Symp. on Nucl. Phys.*, **2019**, *64*, 904-905.

15. Pulse Shape Discrimination and Time of Flight measurements for n/γ with CAEN digitizer, **Sathi Sharma**, Shruti De, Dipayan Chattopadhyay, Sangeeta Das, M. Saha Sarkar, *Proceedings of the DAE-BRNS Symp. on Nucl. Phys.*, **2019**, *64*, 984-985.

16. Coincidence Study between internal conversion electrons and γ-rays in ^{152}Eu, Sangeeta Das, **Sathi Sharma**, Shruti De, M. Saha Sarkar, *Proceedings of the DAE-BRNS Symp. on Nucl. Phys.*, **2019**, *64*, 988-989.

Sathi Sharma

Sathi Sharma

Dedicated to my family, teachers and friends ....

ACKNOWLEDGEMENTS

Contents

Sathi Sharma

Sathi Sharma

List of Figures

List of Tables

Chapter 10

Conclusions and future outlook

In the present thesis work, the resonant state at 7556 keV of ^{15}O has been populated using ^{14}N(p,γ) resonance reaction at an energy E_p^{lab} = 278 keV. To perform the resonance reaction, two implanted targets have been prepared using two facilities – one at SINP and the another one at TIFR, Mumbai. The implanted target produced using the isotope separator has less yield of nitrogen so that we have used the second target which was prepared at TIFR ECR machine. We have given considerable time and effort to fabricate the implanted nitrogen targets. The target was carefully characterized via several techniques at different laboratories – XPS, SEM, SIMS at SINP and RBS at IUAC, Delhi. Next, one electrically cooled Broad Energy Germanium (BEGe) detector and LN$_2$ cooled HPGe detector have been characterized from 0.122 MeV to 7 MeV using laboratory standard source, *i.e.*, ^{152}Eu and in-beam resonance reaction data of ^{14}N(p,γ)^{15}O at E_p^{lab} = 278 keV. In case of BEGe detector, only the characterization data up to 2 MeV were available in literature. So, it is first time characterized at higher energies up to 7 MeV in the present thesis work. The BEGe detector response also has been simulated in case of offline data as well as in case of in-beam data. The agreement between the experiment and simulation is

quite well (within 1σ level) in each case. All the characterization data have been used fruitfully in future for this BEGe detector for different capture reactions.

The implanted target was scanned by varying the proton beam energy from the ECRIA machine in between 278 keV to 312 keV . The implanted target used in the present experiment has energy width, $\Delta E = 21 \pm 1$ keV. As, $\Delta E >> \Gamma$ (width of the resonance), we have used the thick target approximations to determine the resonance strength ($\omega\gamma$). The value obtained from the present experiment agrees reasonably well with the literature value.

The main aim to perform the experiment is to obtain the finite lifetime (τ) or level width (Γ) of the sub-threshold resonant state of ^{15}O at 6792 keV. Here, we have adopted the DSAM technique to obtain the lifetime of the state. But, in our present measurement, we are not able to get finite lifetime of the sub-threshold state. We are able to give a lower limit to the width of this state, $i.e.$, Γ is > 0.56 eV. The present experiment actually further constrained the lifetime or energy width value of the sub-threshold state. The finite and well agreed with the literature value of the lifetime of the 5181 keV ($\tau = 10.45^{+2.07}_{-2.21}$ fs) state proves the measurement accuracy or the reliability of the present experimental setup. Thus, the facility at TIFR and the experimental arrangements used at the time of experiment can be effectively used in future to perform such kind of low energy resonances and level lifetimes or level widths.

Theoretical calculations are needed in parallel with the experiments to reduce the uncertainties in the nuclear physics inputs in calculation of stellar models. Theoretical shell model calculations have been performed long back to study the structural properties of some of these resonance states in the light mass region. There are few microscopic large basis theoretical calculations which have been done recently. So, in the present thesis work, we report on large basis shell model (LBSM) calculations of low lying energy levels, level lifetimes, proton spectroscopic factors of ^{15}O nucleus up to the resonance state at 7556 keV. The resonance state has been reproduced at 7646 keV in shell model calculation using the ZBM model space with REWIL interaction. The calculated spectroscopic factor of the resonance state agrees with the experimental value in previous literature. Another code WSPOT was used here to calculate the resonance width of the 7556 keV resonance state. The calculated width was 1.2 keV which is nearly equal to

the experimental value. So, the theoretical calculations are in agreement with the experimental results in most of the states. However, few disagreements indicate the necessity of improved interactions in the lighter mass regime. This kind of phenomenological work is really important to validate the experimental work wherever the data are available and especially in case of those reactions which are really difficult to perform in laboratory.

The work related to the study of background γ-radiation is one of most important factor before planning any astrophysical reactions at the accelerator facility. The FRENA facility is in the process of installation. So, before doing any capture reaction measurements, it is necessary to properly suppress the background γ-radiation to see the actual reaction events. In the present thesis work, we have obtained the integral count rate at different locations of the FRENA facility and compare it with two another normal nuclear physics laboratories. We have developed passive and active shielding arrangements with the present equipments in our laboratory. The shieldings are really effective in suppressing the background γ-radiation up to 3 MeV. The simulation code developed to design the shielding arrangements will be helpful in future setups at FRENA facility. We will use the shielding arrangements in the in-beam experiments at FRENA in future to eliminate the unwanted γ-ray events from the actual reaction events.

The characterization of the SUM spectrometer with laboratory standard sources have been performed at different conditions. Some observed characteristics have been resolved with the help of Monte Carlo simulation. The simulation code is in the development stage as all the properties of the detector are not resolved till now. After the proper characterization of the SUM spectrometer, we can use the high efficiency detector in measuring the β-decay of neutron rich nuclei or r-process nuclei. We can use it also to study the low cross-section capture reactions which are important in stellar environment at the FRENA facility.

Summary

The nuclear physics inputs like nuclear masses, β-decay half-lives, feeding pattern, branching ratios, reaction cross-sections at relevant stellar energies are essential for better understanding of stellar nucleosynthesis. The direct measurements at Gamow energies are difficult to perform at laboratory due to the extreme low cross-sections. Thus, the data measured at higher energies fitted and then extrapolated to Gamow energies using theoretical models like R-matrix. But these kinds of extrapolations fail severely if there exists any resonances at these energies. So, it is necessary to extend the direct measurements to look for these kinds of low energy resonances. One of the important reaction in the CNO cycle is ^{14}N(p,γ)^{15}O reaction which regulates the energy production for stars slightly more massive than the sun (M > 1.5 M$_\odot$) throughout the stable hydrogen burning on the main sequence. The reaction has several impacts in nuclear astrophysics – from neutrino production in our Sun, to age estimates of globular clusters in our Galaxy. The largest contribution to uncertainty in the CNO cycle reaction rate is due to the lifetime (τ) or energy width (Γ) of the sub-threshold resonance state of ^{15}O at 6792 keV ($E^r_{c.m.}$ = -504 keV). These kinds of measurements require proper energy calibration and resolution of the accelerator delivering the proton beam, isotopically pure impurity free targets, well characterized γ-detectors and suppression of γ-radiation background. The present thesis work is devoted to both the experimental and theoretical study of ^{14}N(p,γ)^{15}O resonance reaction at E^{lab}_p = 278 keV. The experiment was performed at TIFR, Mumbai with the proton beam from the ECR machine using an implanted ^{14}N target. In the present work, the implanted target was prepared and characterized properly before using it at the final experiment. One of the detector used in the experiment which is basically an electrically cooled Broad Energy Germanium detector, has been characterized from 0.122 MeV to 7 MeV using the laboratory standard sources and the in-beam resonance reaction data. To perform the lifetime measurement, we have adopted the Doppler Shift Attenuation Method (DSAM). The lifetime of the sub-threshold resonance state at 6792 keV as well as for two other states, *i.e.*, 6172 keV and 5181 keV of ^{15}O have been determined in the present work. In case of 6792 keV state, we cannot give any finite value, but the upper limit has been quoted in this work. The lower limit of the width (Γ) has been determined from

the relation, $\Gamma = \hbar/\tau$. Theoretical calculations also have been performed in parallel with the experimental measurements. The partial wave analysis has been used to calculate the width of the resonance state. From the analysis, we get a prediction of the proton spectroscopic factor of the 7556 keV resonance state. The Large Basis Shell Model (LBSM) calculations using the NuShellX code predicts the level lifetimes and proton spectroscopic factors of the low lying states of ^{15}O quite well in most of the cases.

The present thesis work also includes the developmental work which has been performed at SINP, Kolkata which are directly related to the future experiments in nuclear astrophysics. One low energy accelerator facility named FRENA (Facility for Research in low Energy Nuclear Astrophysics) is in the process of installation at SINP, kolkata. Before performing any dedicated low cross-section measurements at FRENA facility, it is necessary to have an idea about the background γ-radiation at the measurement places. Thus, the γ-ray background measurement has been performed to evaluate the feasibility of studying low cross-section (nanobarn to picobarn range) astrophysical reactions. Monte Carlo simulation also has been performed to evaluate the contribution of the thick concrete walls (1.2 m) in the indoor environment of FRENA halls, especially in the γ-ray spectrum below 3 MeV. The simulations also have been used here to optimize the passive shielding arrangements. The present thesis work includes the characterization of the SUM spectrometer which can be effectively used in β-decay studies of neutron rich nuclei that are produced in the fission reactors and astrophysical r-process. This SUM spectrometer can be used as a 4π- total absorption spectrometer (TAS) which basically reduces the chances of missing transitions and weak β-feeding branches (which is not possible with the conventional high resolution γ-spectroscopy technique). The SUM spectrometer has already characterized using laboratory sources like ^{137}Cs, ^{60}Co, *etc*. To understand the observed properties of the SUM spectrometer, Monte Carlo code has been developed using GEANT4 toolkit.

Overall, the developmental works will be really effective in designing the future experiments at low energy accelerator facility FRENA, Kolkata.

Chapter 1

Introduction

To understand the stellar nucleosynthesis, nuclear physics data like masses, β-decay half-lives, feeding pattern and β-decay branches, reaction cross-sections at relevant energies are essential. These informations related to stellar nucleosynthesis are very important to trace the origin and evolution of different elements and play a crucial role in constraining the theoretical models of stars [1]. Most of the stellar reactions take place far below the Coulomb barrier. So, the cross-sections are very low typically $\sim$ nanobarn to picobarn range in case of direct measurements. These kind of direct measurements are really difficult to measure in laboratory. So, in general, data which have been measured at higher energies are fitted and then extrapolated to relevant stellar energies. These theoretical extrapolations faces serious problems whenever there exist resonances at lower energies. Therefore, it is necessary to extend the limit of direct measurements to relevant stellar energies to look for these resonances and study them rigorously. The resonant capture reaction cross-section is order of magnitude higher compared to non-resonant capture (*i.e.*, direct capture) reaction cross-section. So, it is relatively easier to measure the proton capture resonances especially the stronger ones with higher strengths in the laboratory. Now, to

perform these kind of astrophysical reactions, we need several necessary things like – 1) precisely calibrated accelerator machine which can provide high beam current ($\sim \mu$A), 2) the beam should be steady over a long beam time and the energy spread of the beam has to be as minimum as possible, 3) isotopically pure, impurity free targets, 4) well characterized γ-detectors and, 5) suppression of γ-radiation background coming from natural radioactivity as well as from extraterrestrial radiation.

The nuclei heavier than iron primarily synthesized via neutron capture reactions. The neutron capture occurs through r-process and s-process in stellar sites and these processes are interspersed by β-decays. The β-decay feeding pattern, β-decay half-lives play significant roles in these astrophysical processes. The path of the r-process lies through neutron rich nuclei which are not studied very well. So, the measurement of β-decay branching ratio and well-understood level schemes will be very important in detailed predictions of the neutron capture processes. Total Absorption Spectroscopy (TAS) technique will be effective in studying these kind of processes. These TAS detectors provide almost 4π- angular coverage for the detection of γ-rays and thus have large detection efficiency compared to available high resolution γ-detectors. At Saha Institute of Nuclear Physics (SINP), we have a SUM spectrometer with six (6) large sectors of NaI(Tl) detectors which can be effectively used as a TAS detector to perform β-decay studies.

The thesis basically includes both the experimental and theoretical study of low energy resonances relevant for nuclear astrophysics and associated developmental works. In this present work, the main focus is on hydrogen (H) - burning in stellar environment which is discussed below in details.

1.1   H - burning in stars

According to the astronomers, there are two distinct stellar populations according to their ages and chemical abundances – Population I and Population II stars. They basically differ in their age and their content of metals (through which astronomers mean any element other than hydrogen and helium). Population I stars are metal rich. They are the youngest stars (including our Sun)

and can be found in the disk of the Galaxy. On the other hand, Population II stars are metal poor. They are generally found in the halo and the bulge of the Galaxy [1]. In Population I stars, the energy production mainly occurs via hydrogen burning – two hydrogen atoms fuse together to form helium. This process is known as Proton-Proton chain (PP chain). In stars which are more massive than Sun, the energy production occurs through Carbon-Nitrogen-Oxygen cycle (CNO cycle). In my present work, I will examine $^{14}N(p,\gamma)^{15}O$ reaction – one of the important hydrogen burning reaction of the CNO cycle 1. So in the next section, I will discuss about the H - burning cycles in stars in a little bit more details.

1.1.1   Proton-Proton (PP) chain

The first step in the PP chain is the fusion of two protons to form the only stable two nucleon system, *i.e.*,

$$^{1}H +^{1} H \rightarrow^{2} H + e^{+} + \nu \tag{1.1}$$

The Q-value of this reaction is 1.44 MeV. This is a weak interaction process and the cross-section to be of the order of 10^{-33} b at keV energies and 10^{-23} b at MeV energies [2]. But due to the presence of enormous number of protons, the total reaction rate is of the order of 10^{38}/s. This step is generally known as "bottleneck" as it is the slowest and least probable step in the PP chain. Now, it is very likely that the deuteron will take one proton to produce ^{3}He with Q-value of 5.49 MeV.

$$^{2}H +^{1} H \rightarrow^{3} He + \gamma \tag{1.2}$$

The ^{3}He nucleus may take one proton to produce ^{4}Li but ^{4}Li does not exist as a bound system. So, the ^{3}He nucleus wait for the another ^{3}He nucleus to combine and produce ^{4}He nucleus with a Q-value of 12.86 MeV.

$$^{3}He +^{3} He \rightarrow^{4} He + 2 \ ^{1}H + \gamma \tag{1.3}$$
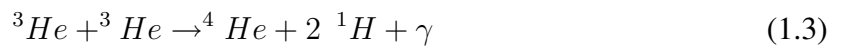
So, the net reaction is the conversion of four protons to helium. It is known as the PP I chain. The total energy released during the $4\ ^1\text{H} \rightarrow\ ^4\text{He}$ conversion is 26.7 MeV. One competing reaction with ^3He nucleus is to fuse with an α- particle to produce ^7Be nucleus in the following way,

$$^3He +^4 He \rightarrow^7 Be + \gamma \tag{1.4}$$

Now, the ^7Be either capture an e^- or fuse with a proton with 99.88% and 0.12% probability respectively (in case of solar fusion). The reactions are following:

$$^7Be + e^- \rightarrow^7 Li + \nu\ ; \qquad ^7Li +^1 H \rightarrow 2\ ^4He \tag{1.5}$$

$$^7Be +^1 H \rightarrow^8 B + \gamma\ ; \qquad ^8B \rightarrow^8 Be^* + e^+ + \nu\ ; \qquad ^8Be^* \rightarrow 2\ ^4He \tag{1.6}$$
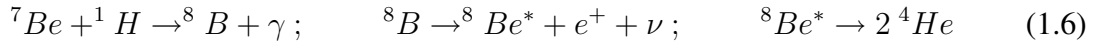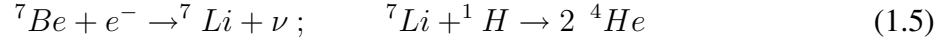
These alternate ways of conversion from $4\ ^1\text{H} \rightarrow\ ^4\text{He}$ are known as PP II and PP III chains respectively. The net reaction and net energy release are the same for these three possible ways. The reactions involved in the PP chain have been shown schematically in Fig. 1.1. The PP chain dominates at temperatures lower than 20 MK.

1.1.2   Carbon-Nitrogen-Oxygen (CNO) cycle

Stars with masses M > 1.5 $\text{M}_\odot$ burns hydrogen predominantly via CNO cycles. There are basically four CNO cycles through which hydrogen burning occurs using different isotopes of C, N and O. One such series of reactions which belong to CNO cycle 1 are:

$$^{12}C(p,\gamma)^{13}N(\beta^+,\nu)^{13}C(p,\gamma)^{14}N(p,\gamma)^{15}O(\beta^+,\nu)^{15}N(p,\alpha)^{12}C \tag{1.7}$$
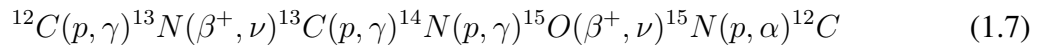
Here, the ^{12}C nucleus is neither created nor destroyed. It basically acts as a catalyst to aid in the fusion process. The net process is : $4\ ^1\text{H} \rightarrow\ ^4\text{He} + 2e^+ + 2\nu$, which is similar to the PP chain. There are three more CNO cycles which exist because both the (p,γ) and (p,α) channels are energetically allowed in case of ^{15}N, ^{17}O, ^{18}O, and ^{19}F nuclei [1]. In contrast, ^{12}C, ^{13}C, ^{14}N,

$$p + p \to {}^2H + e^+ + \nu_e \qquad\qquad p + e^- + p \to {}^2H + \nu_e$$

99.76% $\qquad\qquad\qquad\qquad\qquad\qquad$ 0.24%

$${}^2H + p \to {}^3He + \gamma$$

$\qquad\qquad\qquad\qquad$ 16.70%

83.30% $\qquad\qquad\qquad\qquad\qquad\qquad\qquad\qquad\qquad\qquad\qquad\qquad$ ~2×10⁻⁵%

$${}^3He + {}^3He \to {}^4He + 2p \qquad {}^3He + {}^4He \to {}^7Be + \gamma \qquad {}^3He + p \to {}^4He + e^+ + \nu_e$$

99.88% $\qquad\qquad\qquad\qquad\qquad$ 0.12%

$${}^7Be + e^- \to {}^7Li + \nu_e \qquad\qquad {}^7Be + p \to {}^8B + \gamma$$

$${}^7Li + p \to 2\,{}^4He \qquad\qquad\qquad {}^8B \to {}^8Be^* + e^+ + \nu_e$$
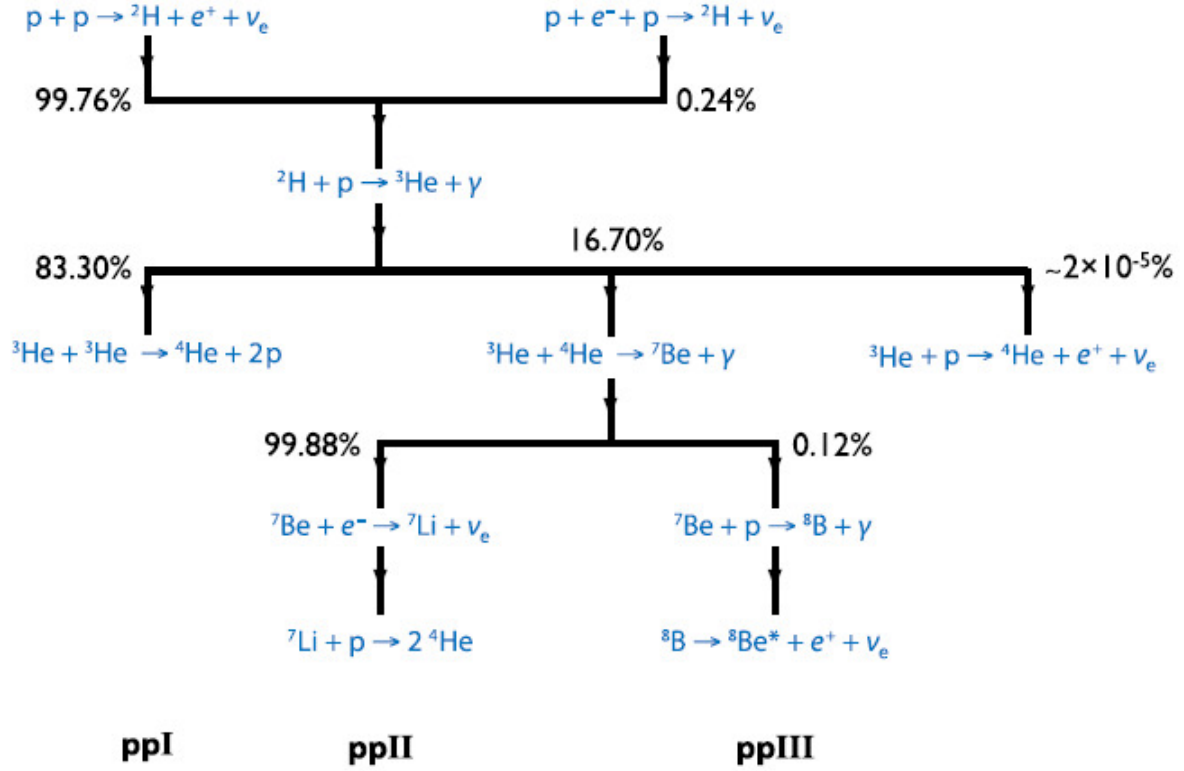
ppI $\qquad\qquad$ **ppII** $\qquad\qquad\qquad$ **ppIII**

Figure 1.1: *The diagram of the PP chain reactions and respective branching percentages between the three principal chains (PP I, PP II, PP III) for the sun (taken from Ref. [3]).*

and ^{16}O nuclei can only proceed via the (p,γ) reaction. The four CNO cycles - CNO 1, CNO 2, CNO 3 and CNO 4 are represented schematically in Fig. 1.2. The net process is same in case of all these four cycles. Now, the (p,α) and (p,γ) channels compete to each other. According to Ref. [1], the (p,α) reaction rate is faster than the (p,γ) reaction in case of ^{15}N, ^{17}O, ^{18}O, and ^{19}F nuclei over the temperature range from 0.01 GK to 10 GK. In case of ^{15}N, there is a small chance of about 1:1000, that the nucleus leaks to the CNO 2 cycle via the ^{15}N(p,γ)^{16}O reaction [1]. Although, most of the material will produce ^{12}C via the dominant (p,α) reaction. In other side, ^{16}O is transformed to ^{17}O which will be destroyed by the (p,α) reaction. It leads to the formation of ^{14}N and operation of the CNO 1 and CNO 2 cycles [1].

Now, the rate of energy production in the CNO cycle or any kind of series of reactions mainly guided by the slowest reaction. In CNO cycle 1, ^{14}N(p,γ)^{15}O reaction is the slowest reaction and it progresses at a rate nearly 1000 times slower than the next slowest reaction, *i.e.*,
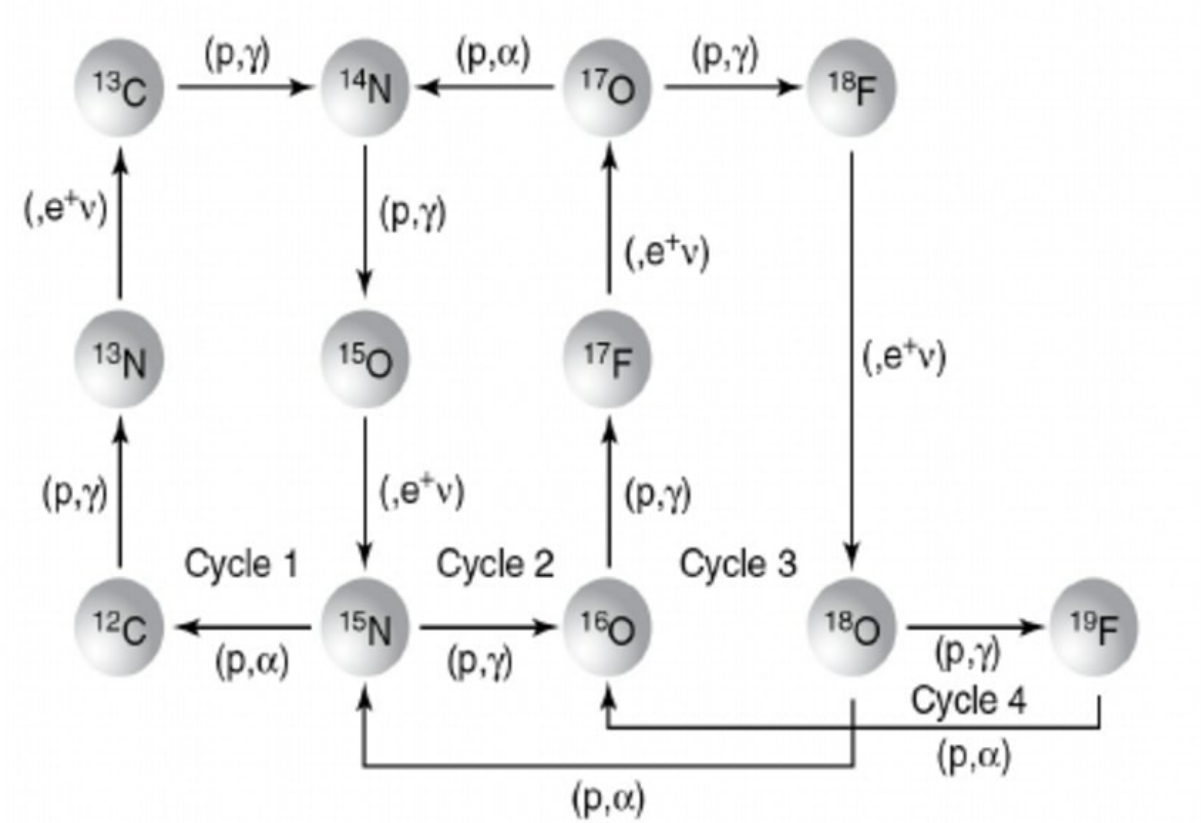
Figure 1.2: *The diagram of the CNO cycle reactions. In this present work, the interested reaction is the bottleneck reaction, i.e., $^{14}N(p,\gamma)^{15}O$ of CNO cycle 1. This picture is taken from Ref. [4].*

$^{12}C(p,\gamma)^{13}N$ [5]. The β^+- decays of unstable nuclei like ^{13}N ($T_{1/2}$=9.965 min), ^{15}O ($T_{1/2}$=122.24 s), ^{17}F ($T_{1/2}$=64.49 s) and ^{18}F ($T_{1/2}$=109.77 min) nuclei for the temperatures in hydrostatic hydrogen burning proceed at a faster rate than the competing proton capture reactions on the unstable nuclei. So, the β^+- decays of unstable nuclei do not play any important role in energy production. The slow rate of $^{14}N(p,\gamma)^{15}O$ reaction thus controls the speed at which the CNO cycle can operate.

- Now, I will discuss about some of the important physical quantities which are related to the study of nuclear reactions.

1.2 Nuclear reactions

In nuclear physics, a nuclear reaction is a process in which two nuclei collide to produce one or more nuclides. A reaction can involve more than two particles colliding to each other at the same time, but such an event is exceptionally rare (like triple alpha process). So, nuclear reactions mainly occur due to the two body interactions. The three body reactions are really complicated. The theory of nuclear reaction can be described using two fundamental forces – the electromagnetic force and the nuclear force. At first, two charged nuclei will approach each other by overcoming the Coulomb potential or the electromagnetic force. The strong interaction takes part at very short distances (≈ 1 fm $= 10^{-15}$ m). It is very difficult to know precisely about the strong interaction. So, nuclear reaction theories are developed using approximated effective potentials. Now, the physical quantities which one can obtain from the laboratory experiments are described in details below.

1.2.1 Cross-section

One of the important physical quantity influencing the reaction mechanism is known as cross-section (σ). It is a quantitative measure for the probability that the incident projectiles will interact to the target nuclei. The cross-section (σ) is generally defined as,

$$\sigma = \frac{(Number\,of\,interactions\,per\,unit\,time)}{(Number\,of\,incident\,projectiles\,per\,unit\,time)\,\times\,(Number\,of\,target\,nuclei\,per\,unit\,area)} \tag{1.8}$$

Now, the cross-section in terms of measurable laboratory quantities:

$$\sigma = \frac{(N_R/t)}{(N_b/t)(N_t/A)} \tag{1.9}$$

Here, N_R/t represents the number of reactions per unit time, N_b/t is the number of incident projectiles per unit time and N_t/A is the number of target nuclei per unit area respectively. As the cross-section physically represents the combined geometrical area of the projectile and the target nucleus, so the unit of cross-section is in terms of cm^2 or m^2. The traditional unit of cross-section is known as "barn" or "b" which is expressed as,

$$1b = 10^{-28}m^2 = 10^{-24}cm^2 \tag{1.10}$$

Typically, the measurable cross-sections are greater than 10^{-9}b. As the cross-section decreases, the challenges are increased enormously to the experimentalists to measure the cross-section precisely.

1.2.2 Astrophysical S-factor

One important parameter which has been introduced in nuclear astrophysics, is the astrophysical S-factor. The astrophysical S-factor is related to the cross-section through the relation,

$$\sigma(E) = \frac{1}{E}exp(-2\pi\eta)S(E) \tag{1.11}$$

Here, σ(E) is the reaction cross-section, E is the energy of the projectile in the centre of mass frame and $e^{-2\pi\eta}$ is the s-wave transmission probability or the Gamow factor respectively. The Gamow factor is only an approximation for the s-wave in case of projectile energies well below the height of the Coulomb barrier. Here, η is the Sommerfeld parameter and it is defined as,

$$\eta = \frac{Z_0 Z_1 e^2}{\hbar v} \tag{1.12}$$

where Z_0, Z_1, v are the atomic nos of projectile, target and the velocity of the projectile. The exponent $2\pi\eta$ can be evaluated numerically using the formula below [1],

$$2\pi\eta = 0.989534 Z_0 Z_1 \sqrt{\frac{1}{E}\frac{M_0 M_1}{M_0 + M_1}} \tag{1.13}$$

where M_0, M_1 are the atomic masses of the projectile and target in atomic mass units (a.m.u.) respectively.

In nuclear astrophysics, we generally use astrophysical S-factor instead of the cross-section of the reaction. Because S-factor is not constant but variation of S-factor with energy is less compared to cross-section as shown in Fig. 1.3. Here, for ^{3}He(α,γ)^{7}Li reaction, within the

energy range 100 keV to 1200 keV, the variation of S-factor is around 0.1 where for cross-section, this is approximately 4 orders of magnitude. So, theoretical extrapolation to low energies is subject to larger uncertainty for cross-section compared to S-factor.
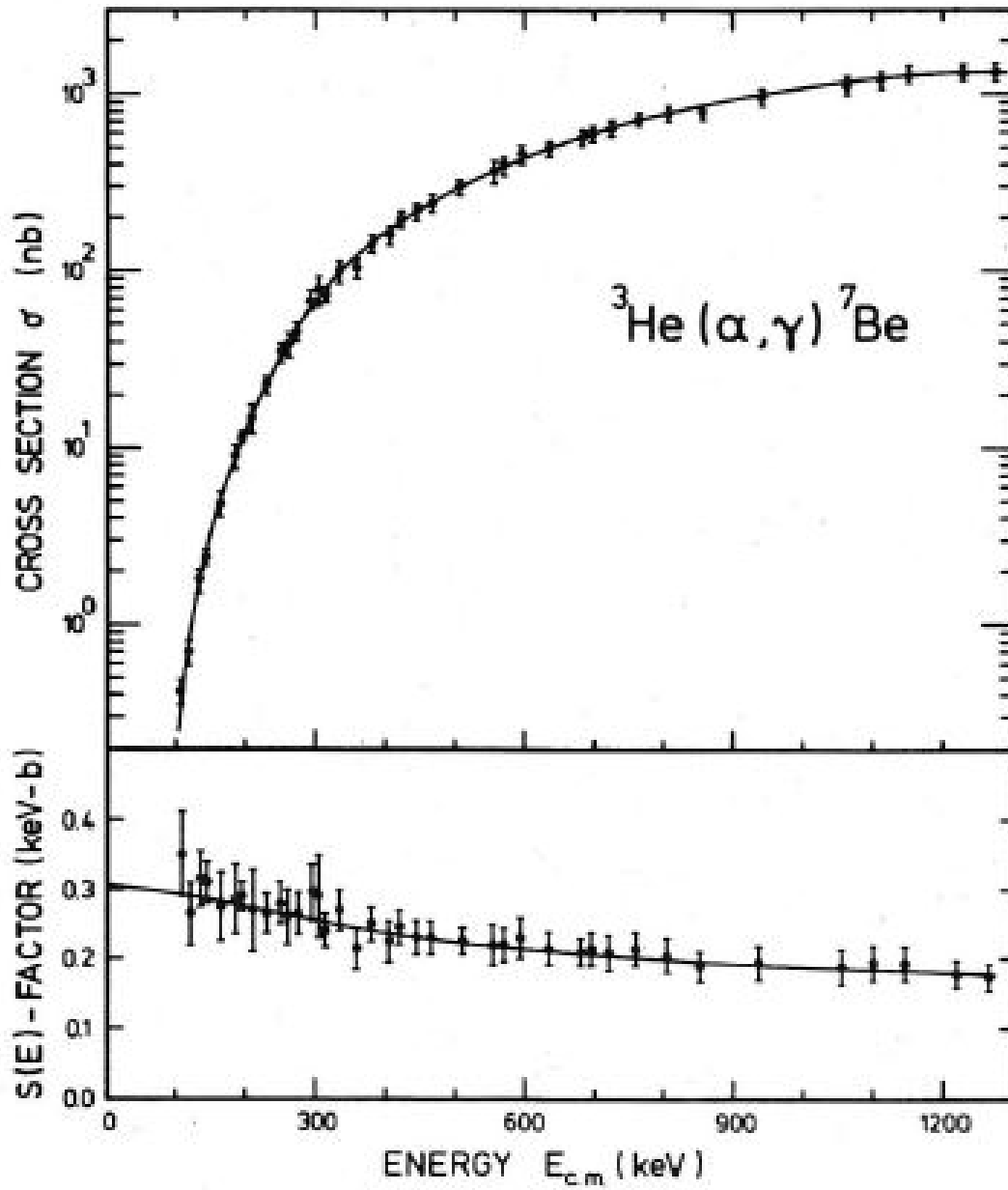
Figure 1.3: *The variation of cross-section and S-factor with respect to energy for the* $^3He(\alpha,\gamma)^7Li$ *reaction. The figure is taken from Ref. [6]. From the figure, it is clear that the variation of cross-section is very sharp compare to the S-factor when the energies are close to zero.*

1.2.3   Reaction rate

In this section, I will discuss only about the charged particle induced reaction rate. Suppose, the projectile (0) is captured by the target (1) and emits electromagnetic radiation as γ-ray. Then, this kind of reaction is known as radiative capture. Here, our main focus is on radiative capture reaction rates. Now, the nuclear reaction rate for a given reaction depends on the number densities of projectile and target, *i.e.*, N_0 and N_1, cross-section of reaction (σ) and the relative velocity (v) of the interacting nuclei 0 and 1. Thus the reaction rate (r_{01}) is given by,

$$r_{01} = N_0 N_1 \sigma(v) v \tag{1.14}$$

In stellar environment, the relative velocity between two interacting nuclei 0 and 1 is not constant. In spite of that, it is described by a probability function $\phi(v)$. Now, $\phi(v)dv$ is the probability that the relative velocity is in between v to $v + dv$ with the normalization,

$$\int_0^\infty \phi(v)dv = 1 \tag{1.15}$$

So, the Eq. 1.14 considering the distribution of relative velocities takes the form like,

$$r_{01} = N_0 N_1 \int_0^\infty v\phi(v)\sigma(v)dv \equiv N_0 N_1 < \sigma v >_{01} \tag{1.16}$$

where $< \sigma v >_{01}$ and $N_0 N_1$ are the reaction rate per particle pair and total number density of pairs of nonidentical nuclei 0 and 1. In case of identical particles, the number density of pairs is N_0^2 (where N_0 is large). So, the general expression for the reaction rate which is valid for both identical and nonidentical particles is:

$$r_{01} = \frac{N_0 N_1 < \sigma v >_{01}}{1 + \delta_{01}} \tag{1.17}$$

where δ_{01} is the Kronecker delta symbol. In stellar plasma, the particles are in thermodynamic equilibrium with each other. So, the velocity distribution can be assumed to follow the Maxwell-Boltzmann distribution, *i.e.*,

$$\phi(v)dv = \left(\frac{m_{01}}{2\pi kT}\right)^{3/2} e^{-(m_{01}v^2/2kT)} 4\pi v^2 dv \tag{1.18}$$

where m_{01} is the reduced mass of the interacting nuclei, k is the Boltzmann constant and T is the effective temperature in kelvin respectively. Now, replacing the probability distribution by Eq. 1.18, the reaction rate per particle pair becomes,

$$< \sigma v >_{01} = \left(\frac{8}{\pi m_{01}}\right)^{1/2} \frac{1}{kT^{3/2}} \int_0^\infty E\sigma(E)e^{-E/kT}dE \tag{1.19}$$

Now, it is usual practice to express the quantity $< \sigma v >$ as $N_A < \sigma v >$ in units of $\mathrm{cm^3mol^{-1}s^{-1}}$ where N_A is the Avogadro constant. So, the numerical expression for the reaction rate per particle pair is given by the equation [1],

$$N_A < \sigma v >_{01} = \frac{3.7318 \times 10^{10}}{T_9^{3/2}} \sqrt{\frac{M_0 + M_1}{M_0 M_1}} \int_0^\infty E\sigma(E)e^{-11.605E/T_9}dE \ \ (cm^3mol^{-1}s^{-1}) \tag{1.20}$$

where the centre of mass energy E is in units of MeV, the temperature T_9 in GK (T_9 = $T/10^9$ K), the relative atomic masses M_0, M_1 in a.m.u. and the cross-section σ in barn. $N_A < \sigma v >$ can be obtained numerically whenever the cross-section $\sigma(E)$ has been measured or estimated theoretically.

There are two distinct extreme cases – 1) the first case refers to cross-sections that vary smoothly with energy, *i.e.*, non-resonant cross-sections and 2) the second case where the cross-sections vary strongly in the vicinity of a particular energy, *i.e.*, resonant cross-sections. These two cases are described in details in the following sections below.

1.2.3.1 Non-resonant capture reaction rate

Non-resonant capture process is known as direct capture process. It is basically a single step process in which a projectile is captured by a target nucleus with the emission of a γ-ray. Finally, it produces a different nucleus in its bound state. In direct capture model, the projectile interacts

with the target nucleus as a single core in spite of taking the nucleons as individuals. So, the non-resonant capture process is relatively faster and the time of occurrence is of the order of 10^{-22} s. The emitted γ-ray in each transition has an energy, $E_\gamma = Q + E_{projectile} - E_x$ to form a bound state of energy E_x in the final nucleus. Here, Q-value represents the mass difference between the initial and final channels masses. The Q-value for $^{14}N(p,\gamma)^{15}O$ reaction is 7297 keV.

Now, the non-resonant reaction rate is evaluated from the Eq. 1.19. After expressing the Eq. 1.19 in terms of S-factor, it takes the form like,

$$N_A < \sigma v >_{01} = \left(\frac{8}{\pi m_{01}} \right)^{1/2} \frac{1}{kT^{3/2}} \int_0^\infty e^{-2\pi\eta} S(E) e^{-E/kT} dE \qquad (1.21)$$

If one consider the S-factor is constant, *i.e.*, $S(E) = S_0$, then the Eq. 1.21 takes the simple form,

$$N_A < \sigma v >_{01} = \left(\frac{8}{\pi m_{01}} \right)^{1/2} \frac{1}{kT^{3/2}} \; S_0 \int_0^\infty e^{-2\pi\eta} e^{-E/kT} dE \qquad (1.22)$$

The most effective energy at which the reaction takes place is determined by the convolution of Maxwell-Boltzmann distribution and the probability of tunnelling through Coulomb barrier of the interacting charged particles. The convolution results in the so called Gamow Peak as shown in Fig. 1.4, which is a function of temperature and charges of the interacting particles. The numerical expression for the most effective, *i.e.*, Gamow energy is given below,

$$E_0 = 0.122 \left(Z_0^2 Z_1^2 \frac{M_0 M_1}{M_0 + M_1} T_9^2 \right)^{1/3} \quad (MeV) \qquad (1.23)$$

where in the numerical expression M_0, M_1 are the relative atomic masses of projectile and target in units of a.m.u. The Gamow peak is generally approximated by a Gaussian distribution with a maximum probability at an energy $E = E_0$. The energy of the Gamow peak (E_0) for the $^{14}N(p,\gamma)^{15}O$ reaction at a temperature of T = 0.015 GK is 26.5 keV. The width (Δ) at which the probability takes the value of 1/e of its peak value, is given by the numerical expression:

$$\Delta = 0.2368 \left(Z_0^2 Z_1^2 \frac{M_0 M_1}{M_0 + M_1} T_9^5 \right)^{1/6} \quad (MeV) \tag{1.24}$$

So, the energy window from E_0 - $\Delta/2$ to E_0 + $\Delta/2$ is the most probable region for the thermonuclear reactions to occur (except in case of narrow resonances). The Gamow region for the ^{14}N(p,γ)^{15}O reaction at a typical temperature of T = 0.015 GK has been shown in Fig. 1.4. Now, the probability distribution factors $e^{-2\pi\eta}e^{-E/kT}$ in Eq. 1.22 is replaced by a simple Gaussian distribution. So, the Eq. 1.22 with constant S-factor looks like,

$$N_A < \sigma v >_{01} = \left(\frac{4}{3} \right)^{3/2} \frac{\hbar}{\pi} \frac{N_A}{m_{01} Z_0 Z_1 e^2} S_0 \tau^2 e^{-\tau} \tag{1.25}$$

where $\tau = \frac{3E_0}{kT}$ is a dimensionless quantity and it is numerically written as,

$$\tau = 4.2487 \left(Z_0^2 Z_1^2 \frac{M_0 M_1}{M_0 + M_1} \frac{1}{T_9} \right)^{1/3} \tag{1.26}$$

In order to calculate the non-resonant cross-section accurately two correction factors must be considered – 1) one due to the asymmetric Gamow peak which we have replaced by symmetric Gaussian peak to simplify the calculations, 2) S-factor is not constant in general. The S-factor can be expanded using a Taylor series expansion at E = 0 as,

$$S(E) \approx S(0) + S'(0)E + \frac{1}{2}S''(0)E^2 + ... \tag{1.27}$$

where S'(0) and S"(0) are first and second derivatives of the S-factor with respect to energy. They are generally obtained from fits to the experimental data. After including the corrections into the Eq. 1.25, the non-resonant reaction rate is given by,

$$N_A < \sigma v >_{01} = \left(\frac{4}{3} \right)^{3/2} \frac{\hbar}{\pi} \frac{N_A}{m_{01} Z_0 Z_1 e^2} S_{eff} \tau^2 e^{-\tau} \tag{1.28}$$

The effective S-factor in Eq. 1.28, S_{eff} is given by Fowler *et al.* [7],

$$S_{eff}(E_0) = S_0 \left[1 + \frac{5}{12\tau} + \frac{S'(0)}{S(0)} \left(E_0 + \frac{35}{36}kT \right) + \frac{1}{2} \frac{S''(0)}{S(0)} \left(E_0^2 + \frac{89}{36}E_0 kT \right) \right] \tag{1.29}$$
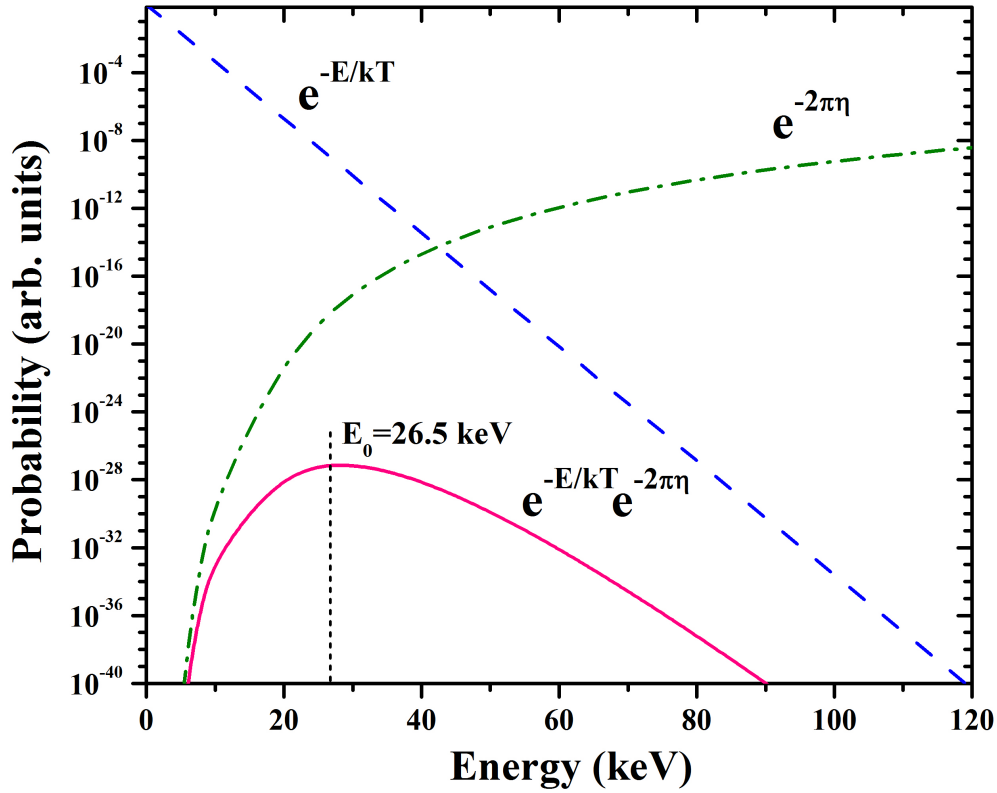
Figure 1.4: *The Maxwell-Boltzmann factor ($e^{-E/kT}$) in dashed line and the Gamow factor ($e^{-2\pi\eta}$) in dashed-dotted line versus energy have been plotted for the $^{14}N(p,\gamma)^{15}O$ reaction. The temperature is T = 0.015 GK. The product $e^{-E/kT}\,e^{-2\pi\eta}$ which is referred to as Gamow peak, is shown in solid line. The most probable energy, i.e., Gamow energy E_0 at T = 0.015 GK is 26.5 keV which has been displayed in Fig. 1.4.*

1.2.3.2   Resonant capture reaction rate

The resonant capture is a two-step process in contrast to direct capture which is a one step process. The resonant capture followed by the formation of an intermediate compound nucleus and the typical time needed for such processes is $\approx 10^{-17}$ s. The resonant capture cross-section is strongly energy dependent and can vary by many orders of magnitude over a small energy region. There are two kinds of resonances depending on the total width (Γ) – narrow resonances and broad resonances. The contributions of these two kind of resonances to the total reaction rate have been discussed in details below.
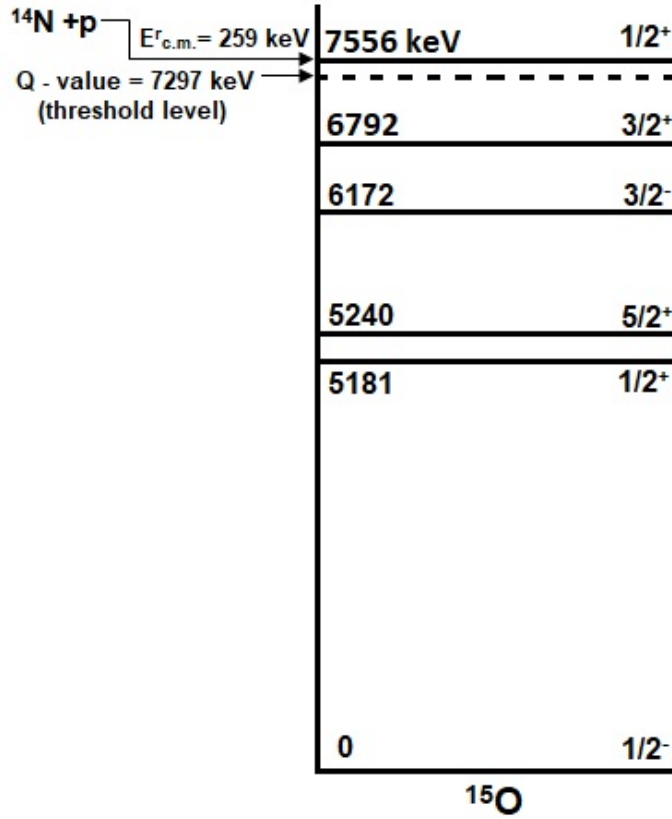
Figure 1.5: *Energy level diagram of ^{15}O up to 7556 keV state populated via $^{14}N(p,\gamma)$ resonance reaction at $E_p^{lab} = 278$ keV ($E_{c.m.}^r = 259$ keV).*

- *Narrow resonance capture reaction rate:*

  A resonance is called narrow whenever the corresponding partial widths are approximately constant over the total resonance width, *i.e.*, Γ less than a few keV [1]. The total width is generally the sum of all the partial widths of all allowed decay channels,

$$\Gamma = \Gamma_p + \Gamma_\gamma + ... \tag{1.30}$$

  In the present study, the main focus is on a narrow isolated resonance where the entrance channel, $^{14}N + p$, forms an excited state at 7556 keV in the ^{15}O compound nucleus at an energy $E_p^{lab} = 278$ keV. The energy level diagram for the $E_p^{lab} = 278$ keV narrow resonance of $^{14}N + p$ capture reaction has been shown in Fig. 1.5. The cross-section of a narrow

isolated resonance is usually given by the one level Breit Wigner formula ,

$$\sigma_{BW}(E) = \frac{\lambda^2}{4\pi} \frac{(2J+1)(1+\delta_{01})}{(2j_0+1)(2j_1+1)} \frac{\Gamma_a\Gamma_b}{(E_r-E)^2+\Gamma^2/4} \tag{1.31}$$

where j_i are the spins of target and projectile, λ is the de Broglie wavelength, J and E_r are the spin and energy of the resonance, Γ_i are the resonance partial widths of entrance and exit channel, and Γ is the total resonance width respectively. Now, the reaction rate for narrow isolated resonance is given by,

$$
\begin{aligned}
N_A < \sigma v >_{01} &= \left(\frac{8}{\pi m_{01}}\right)^{1/2} \frac{N_A}{kT^{3/2}} \int_0^\infty E\sigma_{BW}(E)e^{-E/kT}dE \\
&= \left(\frac{8}{\pi m_{01}}\right)^{1/2} \frac{N_A}{kT^{3/2}} \omega \int_0^\infty E \left(\frac{\lambda^2}{4\pi}\frac{\Gamma_a\Gamma_b}{(E_r-E)^2+\Gamma^2/4}\right)e^{-E/kT}dE
\end{aligned}
\tag{1.32}
$$

where $\omega = (2J + 1) (1 + \delta_{01}) / [(2j_0 + 1) (2j_1 + 1)]$ is known as the spin factor. For a sufficiently narrow isolated resonance, the partial widths and the Maxwell-Boltzmann factor ($e^{-E/kT}$) are nearly constant. So, one can easily replace their values at E = E_r. Thus the Eq. 1.32 looks like,

$$N_A < \sigma v >_{01} = N_A \left(\frac{2\pi}{m_{01}kT}\right)^{3/2} \hbar^2 e^{-E_r/kT}\omega\gamma \tag{1.33}$$

where, $\omega\gamma \equiv \omega\,\Gamma_a\Gamma_b\,/\,\Gamma$ which is proportional to the area under the resonance cross-section. This quantity $\omega\gamma$ is known as the *resonance strength*. From the Eq. 1.33, it is clear that the narrow resonance reaction rate depends only on the energy and strength of the resonance. The numerical expression of the reaction rate for several narrow resonances is gievn below,

$$N_A < \sigma v >_{01} = \frac{1.5399 \times 10^{11}}{\left(\frac{M_0 M_1}{M_0+M_1}T_9\right)^{3/2}} \sum_i (\omega\gamma)_i e^{-11.605E_i/T_9} \quad (cm^3 mol^{-1}s^{-1}) \tag{1.34}$$

where 'i' denotes different resonances, $(\omega\gamma)_i$ and E_i are in units of MeV and M_i are in units of a.m.u.

- *Broad resonance capture reaction rate:*

  Whenever the partial widths, de Broglie wavelength and the Maxwell-Boltzmann factor
  are not constant over the width of the resonance, then it is considered as broad resonance.
  Now, the narrow resonance formalism is no longer valid here. The Maxwell-Boltzmann
  distribution and the cross-sections are now complicated function of energy (see Ref.
  [1]). So, one should numerically solve the equation mentioned below in case of broad
  resonances,

$$N_A < \sigma v >_{01} = \sqrt{2\pi} \frac{N_A \omega \hbar^2}{(m_{01}kT)^{3/2}} \int_0^\infty e^{-E/kT} \frac{\Gamma_a(E)\,\Gamma_b(E + Q - E_f)}{(E_r - E)^2 + \Gamma^2(E)/4}\, dE \quad (1.35)$$

  where Γ_b has to be calculated at the energy available to the exit channel, *i.e.*, at the transition
  energy from the resonance level to a final state E_f. If there are transitions to several final
  states, then one should add the contributions incoherently to the total cross-section.

1.2.3.3   Total capture reaction rate

To calculate the total reaction rate, one should take all the processes contributing remarkably
to the reaction mechanism in the effective stellar energy range. At low stellar temperature and
in case of light nuclei, the density of resonances is relatively small in this energy region. So,
it is possible to resolve such kind of resonances experimentally. The narrow resonances in the
effective stellar region contributes significantly in the total reaction rate. So, they have to be
measured or determined prior to the calculation of total reaction rate. Suppose the resonances
are too weak or none of them are located in the effective stellar region. Then the high energy
wings of sub-threshold resonances, low energy wings of broad resonances and direct capture
processes dominantly contribute in the total reaction rate. If the effective energy lies in excess of
a few MeV, the number of resonances and partial widths become so large to strongly overlap
with each other. In such situation, the total cross-section gives rise to a continuum and only the
effect of energy averaged cross-section has been taken in the reaction rate calculation. So, the
general expression of the total reaction rate is (considering negligible interference effect):

$$N_A < \sigma v >_{total} = \sum_i N_A < \sigma v >^i_{narrow\ resonances} + \sum_j N_A < \sigma v >^j_{broad\ resonances}$$

(1.36)

$$+N_A < \sigma v >_{non-resonant} +N_A < \sigma v >_{continuum}$$

1.3   Aim of the present work

The focus of the present work is to prepare the implanted targets and characterize it through several techniques before using it in the experiment. Next, one electrically cooled BEGe (Broad Energy Germanium) detector and LN$_2$ cooled HPGe (High Purity Germanium) detector have been characterized using laboratory source, *i.e.*, ^{152}Eu and in-beam resonance reaction data of ^{14}N(p,γ)^{15}O at E$^{lab}_p$ = 278 keV. Then, the most important goal of the recent work is to obtain the lifetime of the sub-threshold state 6792 keV. The width (Γ_γ) of the sub-threshold resonant state at 6792 keV have been calculated using the obtained lifetime value of the state. Additionally, the resonance strength of the ^{14}N(p,γ)^{15}O resonance reaction have to be evaluated with the prepared implanted target. Theoretical calculations also have been performed to compare the experimental results with it. Codes like NuShellX [8] and WSPOT [9] have been used for the theoretical calculations.

   In the developmental part, I will discuss about the estimation of background γ-radiation present in the surrounding environment. One accelerator facility named FRENA (Facility for Research in low Energy Nuclear Astrophysics) is in the process of installation at Saha Institute of Nuclear Physics, Kolkata. The FRENA building is surrounded by a 1.2 m thick concrete wall to stop the indoor radiation to go outside. But these thick walls not only act as a shield but also as a source of internal radioactivity. So, this part of my thesis work basically involves the measurements of γ-background, different techniques developed at the laboratory to suppress the background, *etc*. It also includes the Monte Carlo simulation code which have been developed to know the effectiveness of the concrete shielding. The SUM spectrometer mentioned above has been used as a passive and active shielding for the background suppression.

The SUM spectrometer has been characterized both experimentally as well as through simulation to know its response function. This spectrometer can be utilized to study the β-decays of neutron rich nuclei efficiently.

The thesis is broadly divided in two parts – part I includes the study of ^{14}N(p,γ)^{15}O resonance reaction and part II basically incorporates the developmental works related to the low energy astrophysics experiments. Part I contains several chapters related to the motivation to study ^{14}N(p,γ)^{15}O resonance reaction, the experimental details like, accelerator machine used to perform the resonance reaction, detectors, data acquisition systems, implanted targets, target characterization processes, experimental results, theoretical models and results. Part II also contains two chapters related to the estimation and simulation of the background γ-radiation in the FRENA facility and the description of the characterization of the SUM spectrometer and its utilization to study the β-decays. Lastly, in Chapter 10, I will discuss about the conclusion of the present thesis work.

Chapter 2

Motivation

^{14}N(p,γ)^{15}O reaction is one of the important reaction of the CNO cycle which basically regulates the energy production for stars slightly more massive than the Sun (M > 1.5 M$_{Solar}$) throughout the stable hydrogen burning on the main sequence. The reaction has several consequences in nuclear astrophysics - from neutrino production in our Sun, to age estimates of globular clusters in our Galaxy. The observed low energy resonance of the ^{14}N(p,γ)^{15}O reaction is at E$_p^{lab}$ = 278 keV (E$_{c.m.}^r$ = 259 keV) which has great impact in the total reaction rate. The major contribution to uncertainty in the CNO cycle reaction rate is due to the lifetime or energy width of the sub-threshold resonance state of ^{15}O at 6792 keV (E$_{c.m.}^r$ = -504 keV). In the next sections, I will discuss about the astrophysical importance of the ^{14}N(p,γ)^{15}O reaction and review of the previous literatures which explicitly interpret the basic motive to choose this particular ^{14}N(p,γ) reaction.

2.1   Astrophysical importance of ^{14}N(p,γ)^{15}O reaction

Globular clusters (GCs) are spherical collection of stars that are orbiting the galactic core. Globular clusters are very compact due to the gravitational pull toward their centres. GCs are generally found in the halo of a galaxy and contain between 10^5 to 10^6 stars. They are much older than the less dense open clusters which are found in the disk of the galaxy. There are nearly 200 GCs which have been documented in the Milky Way and can be found at great distances ($\approx$ 300,000 light years) [10]. GCs are the best stellar clocks to constrain a lower limit to the age of the universe as they fulfil the following properties – 1) all the stars are more or less formed at the same time, 2) the population is chemically homogeneous and 3) no chance of formation of new stars, which could cover up the oldest population [11].

One of the methods of estimating the age of the GCs is to use the Hertzsprung-Russell (H-R) diagram (see Fig. 2.1) as a tool. H-R diagrams are generally used by astrophysicists to visualize stellar evolution. In Fig. 2.1, the luminosity of stars has been plotted as a function of temperature considering the Sun's luminosity as unity. In H-R diagram, the entire phase of core hydrogen burning is called the main-sequence (MS) phase which is the longest stage in a star's life. Now, one should study the correlation between the luminosity and age at the Main Sequence (MS) turn off point in H-R diagram. When the hydrogen fuel is about to run out from the core, then a star reaches the MS turn off point. The turn off is the hottest position on the main sequence and signifies the point in a star's evolution where hydrogen is exhausted in the core. Whenever a star reaches Main Sequence (MS) turn off point, energy generation changes from PP chain to CNO cycle reactions. Thus, the luminosity is mostly regulated by the ^{14}N(p,γ)^{15}O reaction rate. The luminosity of the MS turn off point decreases with the age of the globular clusters. The age of the globular cluster varies from 10 to 15 Gyr (see Ref. [13]). The current measurement of the age of the universe is 13.8 ± 0.021 Gyr [14]. So, the upper age limit of the globular cluster has to be constrained further. There are several parameters used in the computation of stellar evolution models whose estimated uncertainty can significantly affect the ages of the globular clusters. One of the important parameter amongst them is ^{14}N(p,γ)^{15}O reaction rate as it is the

bottleneck reaction of the CNO cycle [13]. This is one of the most important reason behind the study of ^{14}N(p,γ)^{15}O reaction.
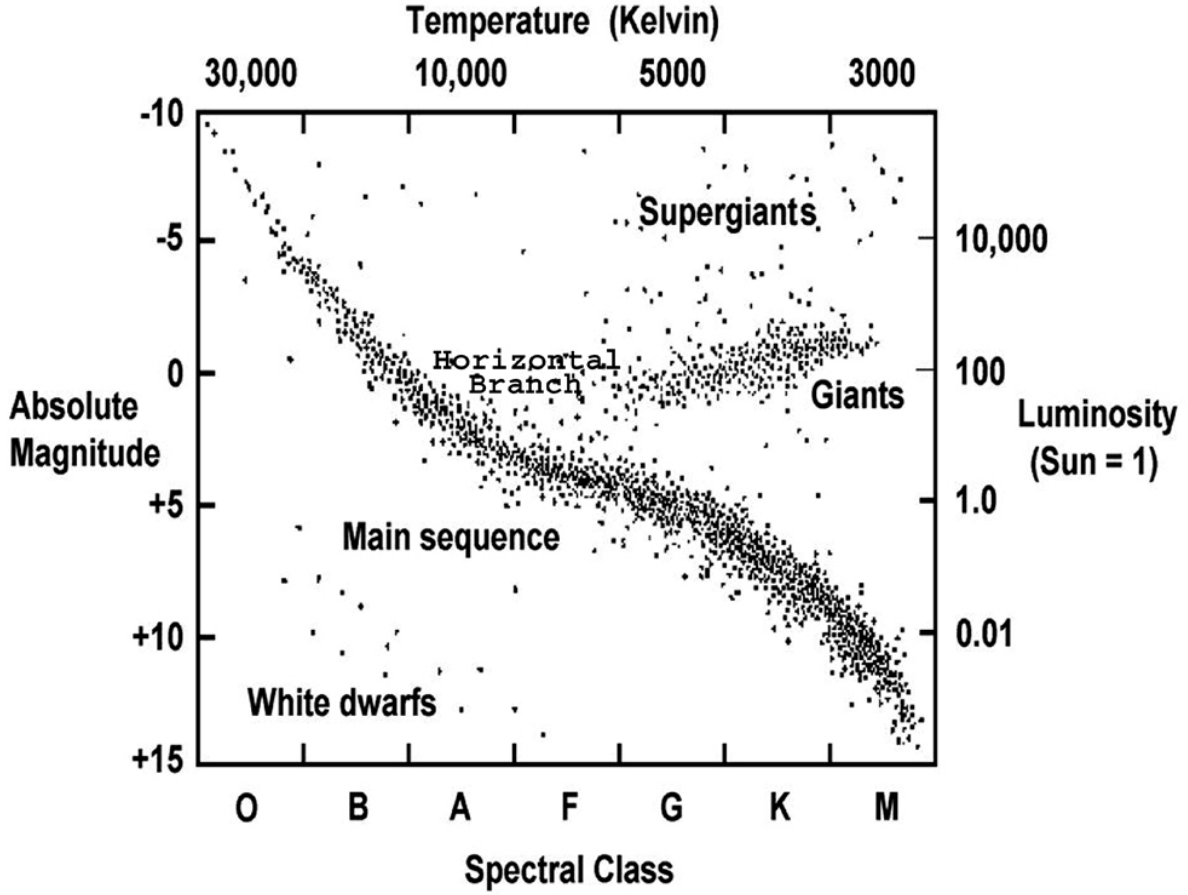
Figure 2.1: *The Hertzsprung-Russell (H-R) diagram – an important astronomical tool that helps in understanding how stars evolve over time. Here, each dot represents a star. The luminosity of stars has been plotted as a function of temperature considering the Sun's luminosity as unity. Stars are also classified by its spectral class from hottest to coolest as follows: O B A F G K M. Each major spectral classification is characterized by its own unique spectra. There are a number of new and extended spectral classes have been designated although O B A F G K and M are the stellar classifications which are commonly shown on H-R diagrams [12].*

The CNO cycle emits the neutrinos by the β-decay of ^{13}N and ^{15}O nuclei. In principle, the CNO cycle neutrino flux would determine the C and N abundances in the Sun's core. Now, the largest factor that inhibits the accuracy of CNO cycle neutrino flux rate is the uncertainty in the nuclear cross-sections ($\approx$ 7.6%) [15] and amongst them the largest uncertainty is from ^{14}N(p,γ)^{15}O reaction. So, the nuclear physics inputs related to the ^{14}N(p,γ)^{15}O reaction is desired

to be revised further to minimize the uncertainties.

2.2   Literature review of ^{14}N(p,γ)^{15}O reaction data

The capture reaction ^{14}N(p,γ)^{15}O over a wide energy range has been performed by Schröder *et al.*
[16]. According to them, the resonance at E_p^{lab} = 278 keV has great impact on the ^{14}N(p,γ)^{15}O
reaction rate. In addition, the sub-threshold resonance at $E_{c.m.}^r$ = -504 keV (*i.e.*, E_x = 6792 keV)
influence the non-resonant yields. They obtained a value of $S_{g.s.}(0)$ = 1.55 $\pm$ 0.34 keV.b which
is nearly half of $S_{tot}(0)$ = 3.20 $\pm$ 0.54 keV.b [16]. Then Angulo *et al.* [17] reanalyzed the data of
Ref. [16] using R-matrix fits. R-matrix is a phenomenological model and can be described as a
boundary value theory. In R-matrix theory, there are two separated regions – internal region, *i.e.*,
the interior of a nucleus and external region, *i.e.*, where only Coulomb interaction is present. The
observables like cross-section, S-factor are determined by matching the logarithmic derivatives
of the wave functions at the boundary [1]. However, reanalysis of the data of Ref. [16] using
R-matrix fit gives a dramatically different result. The total S-factor at zero energy $S_{tot}(0)$ is 1.8
times lower than the previous $S_{tot}(0)$ value from Ref. [16]. The discrepancy occurs due to the
radiative width of the sub-threshold 6792 keV state of ^{15}O. Now, whenever a state has larger
radiative width, *i.e.*, long energy tails, it will affect the probability of captures into other states.
To calculate the S-factor at zero energy the R-matrix analysis takes the radiative width as input
parameters. The authors of Ref. [16] performed the theoretical fit and got the value of Γ_γ = 6.3
eV of the 6792 keV state. But, the obtained value of Γ_γ in case of Angulo *et al.* is 3.6 times less
than the value mentioned in Ref. [16]. There were lots of direct measurements of the ^{14}N(p,γ)^{15}O
reaction [18, 19, 20, 21, 22, 23, 24] and also indirect measurements [25, 26, 27, 28, 29]. The
experiments performed by LUNA collaboration [21, 22] in the energy range $E_{c.m.}$ = 70-480 keV,
is still far from the Gamow energy (E_0 = 26.5 keV). The S-factor data also have been obtained
using APEX detector by S. Daigle *et al.* [5]. The S-factor evaluation and R-matrix analysis is
not directly connected to the scope of the present work. The motivtion of the present work is to
obtain the width of the sub-threshold resonance state 6792 keV as the Γ_γ of the 6792 keV state

is the largest remaining uncertainty in calculating the cross-section of the ^{14}N(p,γ)^{15}O reaction according to all the previous measurements.

Table 2.1: *The lifetime τ and width Γ_γ of the 6792 keV state in ^{15}O of the existing literatures.*

References	τ (fs)	Γ_γ (eV)	Method
1) Schröder *et al.* [16]		6.3	R-matrix fit
2) Angulo *et al.* [17]		1.75 ± 0.60	R-matrix fit
3) Bertone *et al.* [25]	$1.60^{+0.75}_{-0.72}$	$0.41^{+0.34}_{-0.13}$	DSAM
4) Formicola *et al.* [18]		0.8 ± 0.4	R-matrix fit
5) Yamada *et al.* [29]	$0.95^{+0.60}_{-0.95}$	> 0.42	Coulomb excitation
6) Marta *et al.* [23]		0.9 ± 0.2	R-matrix fit
7) Schürmann *et al.* [26]	< 0.77	> 0.85	DSAM
8) Galinski *et al.* [27]	< 1.84	> 0.44	DSAM

Now, if an excited state decays nearly with 100% probability via γ-emission, then it is easy to determine the total radiative width Γ ($\approx \Gamma_\gamma$) by measuring the lifetime of the state τ. The radiative width and lifetime of a state are related via Heisenberg uncertainty relation as, $\Gamma = \frac{\hbar}{\tau}$. The different values of Γ_γ that are either measured or derived have been tabulated in Table 2.1. The lifetime of the 6792 keV, 6172 keV and 5181 keV states have been determined by Bertone *et al.* [25] using Doppler Shift Attenuation Method (DSAM). The measured lifetime of the 6792 keV state by Bertone *et al.* [25] was $1.60^{+0.75}_{-0.72}$ fs which contained the statistical uncertainties only. According to their work, the lifetime value may increase to 3.2 ± 1.5 fs if the target density was of TaN instead of Ta. Next, Schürmann *et al.* [25] adopted the same centroid shift method described in Ref. [26] with better statistics and data at eleven different angles. But, the authors of Ref. [26] could only set an upper limit in the lifetime value ($\tau < 0.77$ fs) and an lower limit in the γ-width value ($\Gamma_\gamma > 0.85$ eV). The recent lifetime measurement of the 6792 keV state of ^{15}O was done by Galinski *et al.* [27] using inverse kinematics. To populate the excited state of ^{15}O, ^{3}He implanted target was bombarded with ^{16}O projectile beam. The beam energy was 50 MeV with maximum recoil velocity of $\beta = 0.05$. They have used the lineshape analysis with relativistic approximations in spite of centroid shift method. Finally, they have obtained an upper

limit of lifetime $\tau < 1.84$ fs which corresponds to a lower limit on the width of $\Gamma_\gamma > 0.44$ eV. So, the three lifetime measurements by different groups [25, 26, 27] gave different results (see Table 2.1). Conclusively, the central value of the lifetime of the sub-threshold state is still uncertain. Such kind of discrepencies in the previous measurements strongly motivate us to remeasure the lifetime.

Chapter 3

Experimental details

In this chapter, I will discuss about the experimental techniques, equipments and procedures that are generally applied in observations of astrophysically important reactions. At first, I will discuss about the accelerator used to perform the ^{14}N(p,γ)^{15}O resonance reaction at an energy, E_p^{lab} = 278 keV. The chapter also includes brief discussions about the target chamber, detectors and data acquisition systems.

3.1   Accelerator

An accelerator is a device which is used to accelerate and impart high kinetic energy to charge particles to produce a high energy ion beam. Such high energy beam is used in the study of nuclear scattering, reaction and other nuclear properties. At first ions are produced from the ion source and then they are accelerated depending on the terminal voltage provided at the High Voltage (HV) desk. Ion sources are of different types and its characteristics determine the limitations to a great extent of any kind of ion beam facility. Ion sources are of two types depending on the charges – positive and negative. Most widely used positive ion sources are

– electron impact ion source, arc discharge ion source, duo-plasmatron ion source, *etc*. The negative ions are produced using sputter ion source. The ECR (electron cyclotron resonance) ion sources are also used to produce high intensity beams $\sim$ mA for proton with low energy. To study nuclear astrophysics, the accelerators should have the special features like [6] –

- The beam current should be high $\sim \mu$A to mA depending on the type of reactions.

- The energy spread of the beam, *i.e.*, beam resolution should be as low as possible (~ 1 keV at several MeV ion energy) due to the presence of several narrow isolated resonances.

- The accelerator beam should be stable over a long period of time during experiment.

The accelerator facility used at the time of present experiment is described in section 3.1.1.

3.1.1   ECRIA at TIFR

The ^{14}N(p,γ)^{15}O resonance reaction at an energy, E_p^{lab} = 278 keV takes place at TIFR, Mumbai. They have a small in house ECR based Ion Accelerator (ECRIA) facility at Department of Nuclear and Atomic Physics, TIFR [30]. The ion source of the accelerator is working based on electron cyclotron resonance principle. The details about the ECR ion source has been given in section 4.3.3. The ions after extraction are focused by an electrostatic Einzel lens. Then the charge states are analyzed by a 90° bending dipole magnet (0.3 tesla). The maximum voltage of the high voltage desk is 400 kV to accelerate the ions further. The rest of the beam line is joined to the analyzing magnet by accelerating columns made of ceramic insulators. To focus the accelerated ions, a set of electrostatic quadrupole lens triplets have been used. It is followed by X-Y deflectors, Faraday cups and beam profile monitors. To minimize the high dosage of X-ray high voltage desk has been covered with aluminium coated lead shields. The schematic diagram of the accelerator has been given in Fig. 4.6. The whole arrangements have been based on LabVIEW command and control system. The accelerator has five beam lines for different measurements. We have used the 0° beam line for our measurements. The machine is previously calibrated using several narrow resonance reactions like ^{27}Al(p,γ)^{28}Si. The typical beam spread on target is 2-3 keV. The proton beam current during our experiment is 3-4 μA.
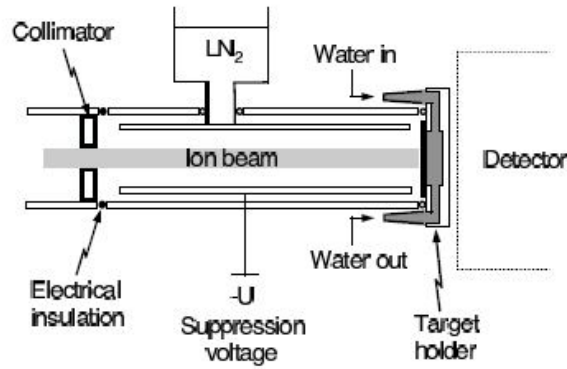
Figure 3.1: *A typical target chamber design used in radiative capture reaction studies (picture taken from Ref. [1]). The beam stop targets have been used in this kind of setup. Water cooling system is there to cool the target during ion beam bombardment. The electrical insulation is also there to isolate the chamber from the rest of the beam line to use it as a faraday cup. The copper pipe is cooled through LN_2 to reduce the build-up of contaminants (such as ^{12}C, ^{13}C, etc.). A negative voltage is applied to the copper tube to suppress the emission of secondary electrons. The small solid and open circles indicate the locations of vacuum O-ring seals.*

3.2 Target chamber

Nuclear reactions take place at a target chamber where the targets are mounted. The specific design of a target chamber depends on type of targets (*i.e.*, transmitted target, beam stopped target, *etc.*) and also on the type of detectors (*i.e.*, γ-detectors, particle detectors) used. A typical target chamber design has been shown in Fig. 3.1 (figure taken from Ref. [1]). It is basically suitable for a beam stopped target. The target backside is directly water cooled to reduce the localised heat during ion beam bombardment. LN_2 dewar is also attached with the chamber to reduce the additional build up contaminants. A negative voltage (typically -300 V) is given to a Cu tube inside the target chamber. The target chamber is completely electrically isolated from the rest of the beam line. So, it can be used as a Faraday cup for the integration of the total charge accumulated by the beam on the target.

We have used a very simple setup in our experiment. First, we have used a ceramic insulator to electrically isolate our target mounted system. The target has been mounted at the end flange (KF40) of the 0° beam line. Here, our target is of beam stop kind of target. Details about the target have been given in Chapter 4. The total charge accumulated after each run is measured using a current integrator. As the beam current is not very high ($\sim$ 3-4 μA), we do not use
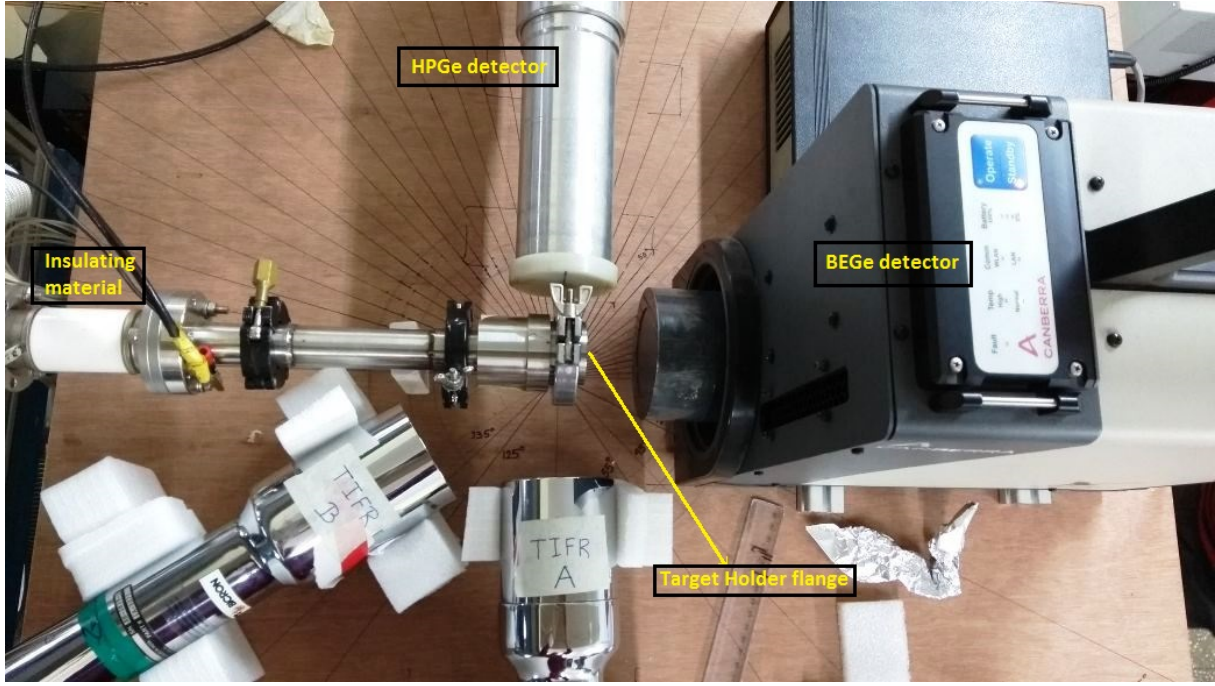
Figure 3.2: *The experimental setup which has been used to study the $^{14}N(p,\gamma)^{15}O$ resonance reaction at E_p^{lab}=278 keV. The target holder flange, 0° beam line of the accelerator, BEGe detector and HPGe detector have been shown in this figure. The insulating material which has been used to electrically isolate the target mounting system from the rest of the beam line is also marked in the figure.*

additional water cooling system. The target mounting system used in our experiment is shown in Fig. 3.2.

3.3 Detectors

One of the important equipment for detecting the nuclear reaction products (like protons, neutrons, α-particles and γ-rays respectively) is radiation detector. The interaction processes of different radiations are completely different from each other. So, the choice of detectors depends on the type of reaction products which one wants to measure. Most of the detectors produce electric charge after interaction with radiations. The electric charge produces an electrical signal due to the applied electric field [1]. A perfect detector should have the following properties – 1) high efficiency, 2) high energy and time resolution, 3) capability of handling high count rate, *etc*. But one has to compromise between detector resolution and efficiency. If high detection efficiency is required, then a price is paid in poor energy resolution [6]. Different kinds of detectors

are – semi-conductor detectors, scintillator detectors, organic detectors, plastic scintillators and proportional counters, *etc*. Semi-conductor detectors have been used widely in high resolution γ-ray spectroscopy. In nuclear astrophysics, large volume HPGe (High Purity Germanium) detectors, 4π-summing detectors (for details check Ref. [1]) are frequently used to detect γ-rays in laboratory.

- In our experiment, we have used two kinds of detectors – 1) electrically cooled Broad Energy Germanium detector (BEGe) and 2) LN_2 cooled High Purity Germanium detector (HPGe).

- The details about the two detectors like dimensions, resolution, efficiency, electronic setups have been described below one by one.

3.4 BEGe detector

The CANBERRA Broad Energy Germanium (BEGe) Falcon 5000 detector [32] is a commercially available electrically cooled detector. The Ge crystal of the BEGe detector gives a clear advantage over the HPGes. Its special electrode structure provides good energy resolution at low energy [33]. The technique of impurity doping in the Ge crystal is such that it consequences in better high energy resolution and peak shape due to improvement in charge collection. All these features intensify the efficiency and resolution at low energy while preserving good efficiency at higher energies. BEGe detectors are also capable of distinguishing between multi-site and single-site energy deposition events [34, 35, 36].

In our present work, we have used Falcon 5000 detector with Ge crystal length of 30 mm and diameter of 60 mm. It has 0.12 mm thick aluminium window. It has 18% relative efficiency (quoted by the manufacturer). The specifications about the BEGe detector are summarized in Table 3.1.

Table 3.1: *Specifications of the BEGe detector used in the present work. Table is taken from Ref. [31].*

Detector			Ge Crystal (mm)		Al window (mm)	
Make	Type	High Voltage(V)	Dia.	Length	Dist.[1]	Thick
Canberra (Mirion)	Falcon 5000 BEGe	-3700	60	30	12	0.12

[1]Distance between the crystal and the endcap.

3.4.1   Electronics setup, data acquisition and analysis

The BEGe detector has been placed at different angles, *viz.* 0°, 25°, 50°, 70°, and 90° with respect to the beamline at a distance of 5 cm from the end flange centre (target centre). The photograph of experimental setup with BEGe detector has been shown in Fig. 3.2. The BEGe detector is a complete stand-alone system with a full version of data acquisition and analysis including GENIE-2000 [37] software. It incorporates a High Voltage Power Supply (HVPS) for the detector and Digital Signal Processing (DSP) unit. The applied reverse bias voltage by the HVPS unit is -3700 V. The input pulse is processed and amplified by the DSP unit. The GENIE-2000 software acquires and analyzes spectra from Multichannel Analyzers (MCAs). The software is capable to handle several functions like MCA control, spectral display and manipulation, basic spectrum analysis and reporting [37]. The amplifier gain has been kept to a minimum value. The spectrum is chosen to have a maximum number of channels (8k). During data acquisition, it is ensured that high energy γ-rays up to 8 MeV can be seen in the spectrum. For primary data acquisition and analysis, GENIE-2000 software has been used. However, for final analysis, an offline analysis programme INGASORT [38] has been utilized. We have used ^{152}Eu (35298 (82) Bq measured on 1st June, 2011) radioactive source for low energy calibration and γ-efficiency (E$_\gamma$ = 0.122 - 1.408 MeV) response of the detector. For high energy (E$_\gamma$> 2 MeV) calibration and γ-efficiency response of the detector, the in-beam ^{14}N(p,γ)^{15}O resonance reaction data has been used. As we have used a thick flange (KF40) as the target holder (see Fig. 3.2) low energy γ-rays are attenuated substantially, even at the 0° position of the detector.

Attenuation is varied at different angular positions of the detector due to its specific design. Thus, the efficiency has been determined experimentally for all positions of the detector with standard ^{152}Eu source placed at the target position. We have acquired the data in singles mode for sufficient time to keep the statistical error minimum. We also have taken care of the contributions from room background and the beam-induced γ-ray background contributions with beam-on through a blank target frame.

3.4.2 BEGe characterization

3.4.2.1 Energy calibration

The detector is calibrated with the laboratory - standard γ-ray sources and with the in-beam spectra of resonance reaction at an angle of 90°. We have used the γ-rays emitted from a ^{152}Eu radioactive source and the resonant level in ^{15}O (7.556 MeV) [39] to calibrate the detector up to 7 MeV. The deviations from linear and quadratic fits to the calibration curves have been plotted for the BEGe detector from 0.122 MeV to 7 MeV. It is shown in Fig. 3.3. From the figure, it is clear that quadratic fit is essential for energies above 3 MeV.

3.4.2.2 Energy resolution

The full width at half maximum (FWHM) of the peak (ΔE) is defined as resolution. The important factors affecting the energy resolution of any detector depends on – 1) statistical fluctuations in the number of charge carriers generated in it following the interaction of nuclear radiation, 2) electronic noise in the pulse processing, *etc*. As the energy increases, the efficiency falls off sharply. Due to this, the statistical uncertainty in charge carrier collection is large. Thus it causes a broadening in the peak width and deterioration in energy resolution [40]. The factors majorly affecting the energy resolution (FWHM) of a γ-detector at a particular energy are – the intrinsic resolution of the detector system from the detector material properties itself and those from electronic components used to process the signal. In case of in-beam data, the additional broadening arises due to the Doppler effect when the γ is emitted by a moving nucleus. The
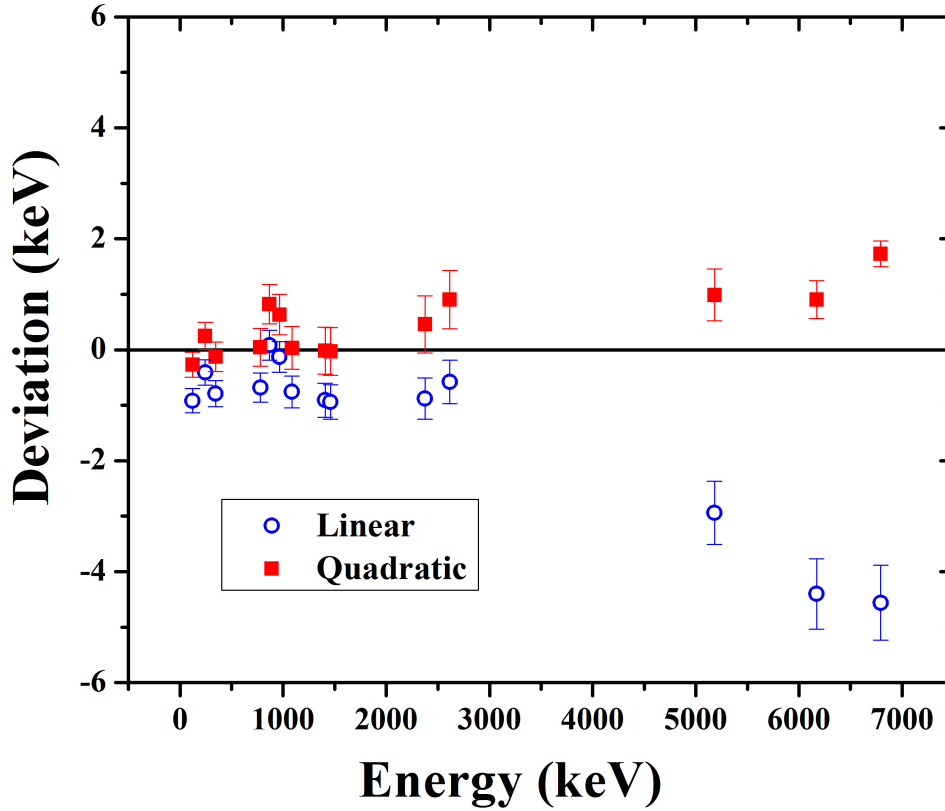
Figure 3.3: *Deviations (keV) from the linear and quadratic fit to the calibration data points of the BEGe detector are plotted (taken from Ref. [31]).*

reasons behind Doppler broadening are – 1) angular position of the detector, 2) the angular spread of recoils in the target, 3) the velocity (energy) variation of the recoils across the target, 4) the finite opening angle of the detector and 5) the proximity of the detector to the target, *etc*. The resolution determined from the radioactive source ^{152}Eu data and in-beam γ-rays emitted by the decay of the resonance state acquired at an angle of 90° are found to be different as a function of energy. The dependency also varies as a function of the angle of the detector with respect to the target position. This is nicely explained considering the lifetimes of the states corresponding to the de-excitation γ-rays which are considered here. The resonance state at 7556 keV has $T_{1/2}$ =0.99 (10) keV. The lifetimes ($T_{1/2}$s) of 5181, 6172 and 6792 keV states are reported as 5.7 (7) fs, < 1.74 fs and < 20 fs respectively [41]. At an angle of 90°, the Doppler broadening for the peaks in the in-beam spectra is maximum. Whereas, at 0°, the peaks are shifted but they have
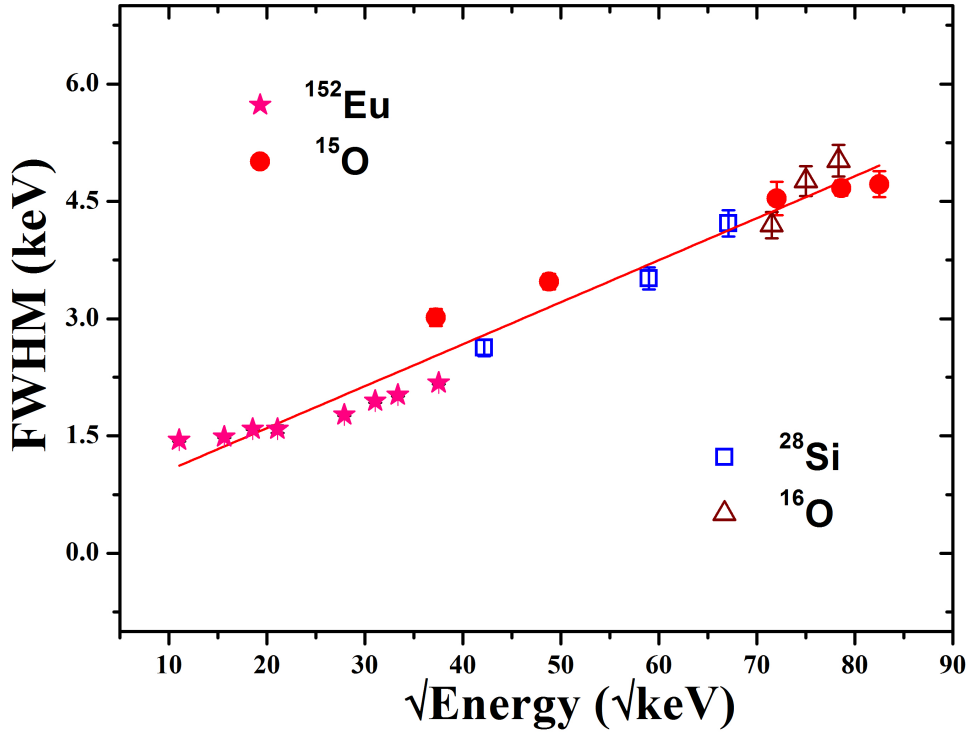
Figure 3.4: *Resolution (FWHM) vs. $\sqrt{E}$ plots for full energy peaks of (i)^{152}Eu radioactive source and (ii) in-beam γ- rays from the excited state of ^{15}O, ^{28}Si and ^{16}O with detector at 0°. The figure is taken from Ref. [31]. All the data points are fitted with a linear equation 0.52(13)+0.053(2)*$\sqrt{E}$ with reduced χ^2=0.06.*

minimum broadening. To extract the energy dependence of resolution up to $\sim$ 7 MeV, we have to eliminate the effects of additional sources in an in-beam data for broadening.

- To check for the probable noise pick-up in beam-on condition, the resolutions of background γ-rays like 1460 keV, 2615 keV, *etc.* are determined in the singles spectra acquired during the beam-on condition. It is found that these FWHMs are similar to those in the off-beam condition.

- We have analyzed the 0° data of the BEGe detector where no or minimum broadening effects are expected [42].

- Monte Carlo code has been used to estimate the broadening arising from the finite opening angle of the detector at 0° for the high energy gammas. We have found that the opening
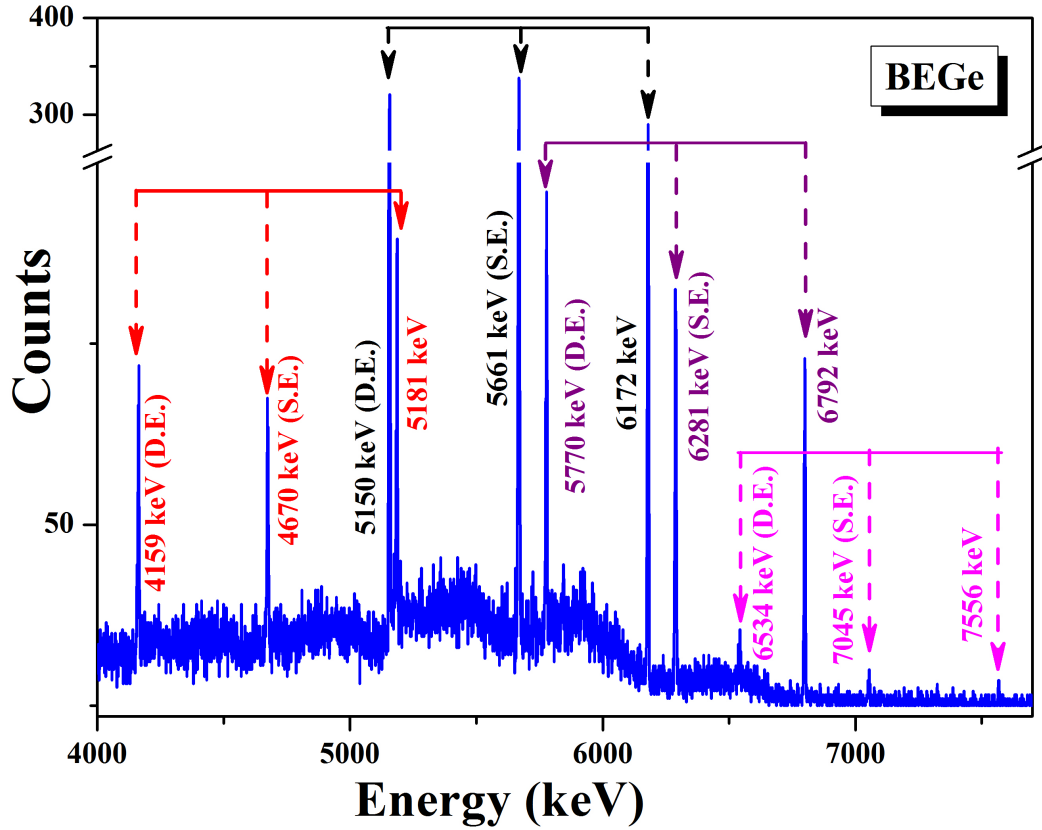
Figure 3.5: *Typical high-energy part of γ-ray spectra from $^{14}N(p,\gamma)^{15}O$ resonance reaction at $E_p^{lab} = 278$ keV for the BEGe detector. S.E. and D.E. denote single escape and double escape peaks, respectively [31].*

angle effect is less than the errors quoted in the FWHM values at higher energies.

• To validate these observations further, broadening effects due to finite lifetimes of the states, we have checked for other γ-rays arising from levels with different lifetimes like – 1) femtosecond (fs) lifetime states of ^{15}O, 2) those emitted by a picosecond (ps) excited state of ^{16}O populated via ^{16}O(p,p'γ) reaction and from states populated in ^{27}Al(p,γ)^{28}Si reaction have also been analyzed.

All these data are acquired with a BEGe detector at 0°. The details of the experiment in which ^{16}O and ^{28}Si nuclei populated, have been given in Ref. [43]. All these data points of resolution vs. $\sqrt{E}$ for the BEGe detector has been plotted in Fig. 3.4. These data points are fitted
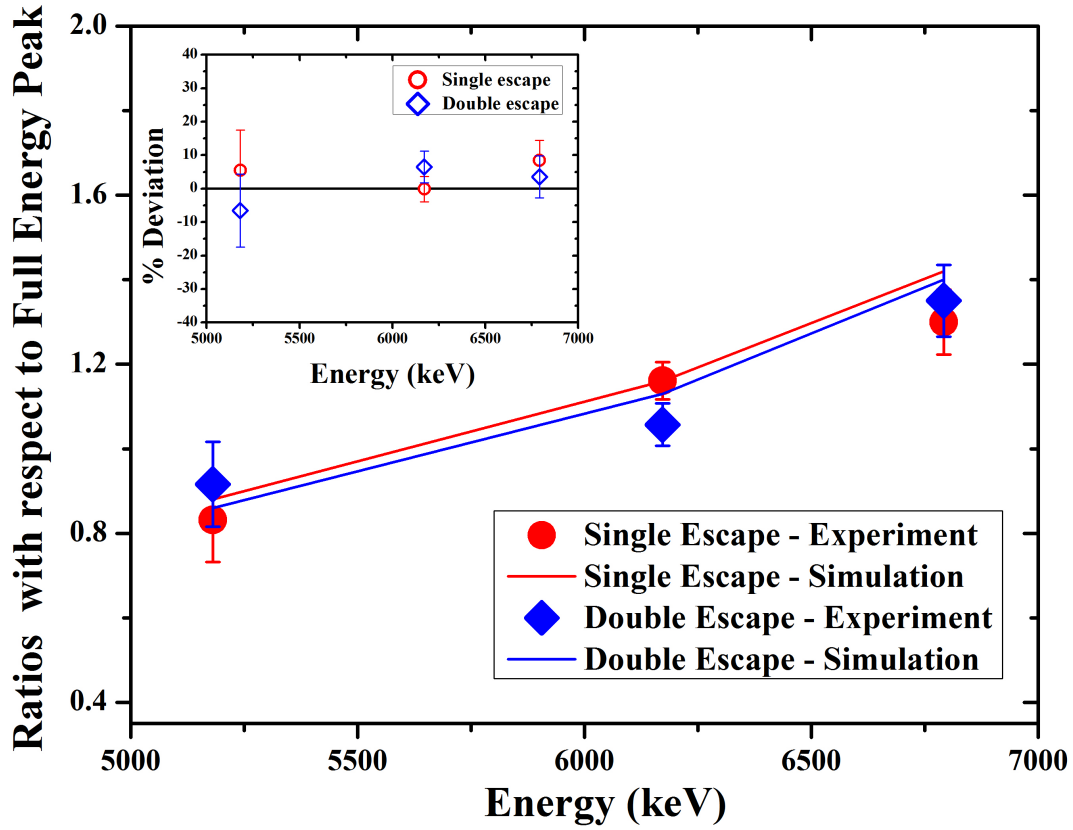
Figure 3.6: *The ratios for S.E. and D.E. with respect to F.E. as a function of γ-energy for the BEGe detector have been plotted here. The percentage deviation of the experimental value from simulation is shown in the inset figure.*

with a straight line $0.52(13)+0.053(2)*\sqrt{E}$ with a reduced $\chi^2 = 0.06$. The FWHM at 1.408 MeV of ^{152}Eu is 2.17 ± 0.02 keV. The value at around 7 MeV for in-beam spectra is 4.72 ± 0.17 keV.

3.4.2.3   Escape peaks

A typical γ-ray spectra of the high energy region for gammas emitted from the resonance state has been shown in Fig. 3.5. The single escape (S.E.) and double escape (D.E.) peaks are also marked in the figure. The ratios of the escape peaks, with respect to the full energy peak (F.E.), clearly show energy dependence. The experimental relative ratios of the escape peaks with respect to full energy peak is plotted in Fig. 3.6. The intensity of the double escape peak is higher among the three peaks (D.E., S.E. and F.E.) in the BEGe detector beyond 5 MeV.
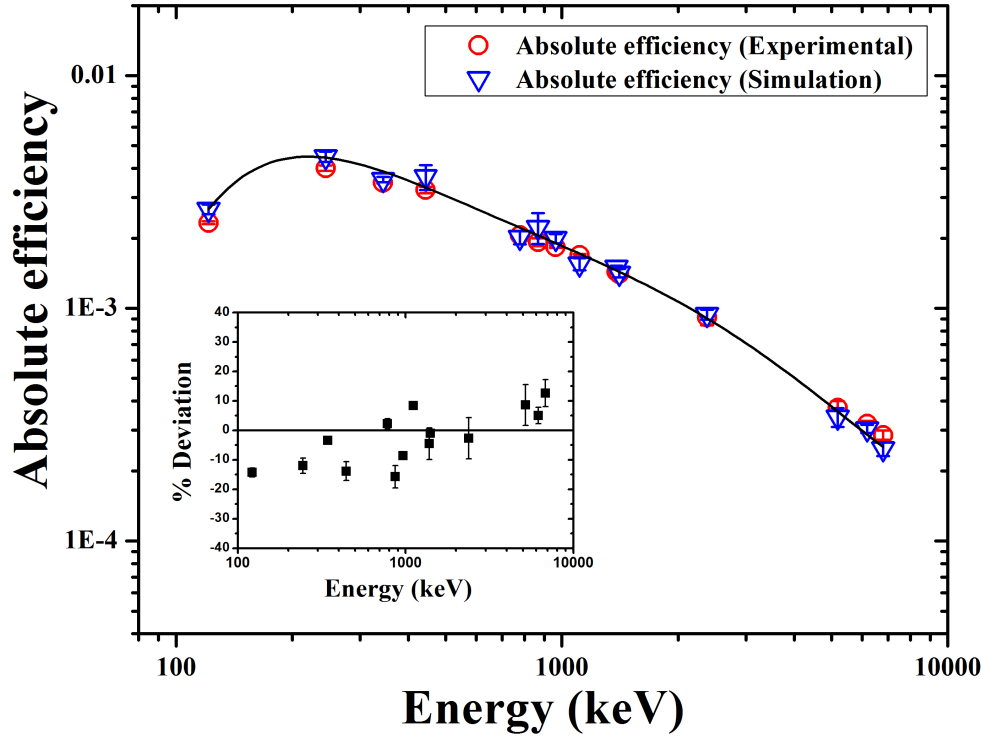
Figure 3.7: *Absolute detection efficiency as a function of energy from 0.122 MeV to 7 MeV. The source is within the target chamber here. Open red circles represent the experimental data for Falcon BEGe at an angle 50^0. The corresponding error bars have been included in the data points. The simulated data points have been plotted with symbol of open triangles, including the error bars. The solid black line represents the 5th order polynomial fit to the simulated data points. The inset shows the percent deviation of the experimental data from simulated results. The errors in the deviation plot are only from the data.*

3.4.2.4   Absolute efficiency

The absolute efficiency at low energy region has been measured using ^{152}Eu source with known activity. To estimate the efficiency at higher energy region, the intensities of γ-rays from the resonant levels in ^{15}O (7.556 MeV) [39] have been used. Now, to get the experimental absolute efficiency at higher energy, we have to normalize the efficiency data from ^{152}Eu and resonance reaction at 1.408 MeV. We have plotted the absolute efficiency as a function of energy of the BEGe detector. Here, we have used the data of the detector at an angle of 50° to minimize the angular distribution effect. The plot is shown in Fig. 3.7. From the figure, we have clearly seen the attenuation of low energy γ-rays at the target chamber. The absolute efficiencies at 6.7 and

7.5 MeV are 2.72e-04±1.19e-05 and 2.23e-04±5.08e-05, respectively.

In calculating the photopeak efficiency of a detector, coincidence summing effects become significant for large volume detectors or equivalently, for close detector-source geometries. Here, in the present experimental set up, the distance between source and detector was 6.3 cm. As the source was not too close to the detector and having comparatively small volumes, the correction due to coincidence summing is small. Coincidence summing effects are frequently apparent from a visual inspection of the (uncorrected) full energy peak efficiency curve if data are taken in close geometry. Some efficiency values will lie on a smooth curve which correspond to non-coincident photons. The other data points that are affected by coincidence summing will lie away from the curve [1]. This information helps the experimentalists to decide if corrections need to be applied in order to achieve the desired precision.

In our present set up, the efficiency data points fall in a smooth curve. This means the coincidence summing correction factor is very small or within the quoted error limit of the efficiency values. Due to this, here we neglect the coincidence summing effect.

3.5 HPGe detector

High Purity Germanium detector (HPGe) is widely used in field of γ-ray spectroscopy. The differences between an HPGe and a BEGe detector are – 1) its impurity doping mechanism, 2) crystal growth technique, 3) electrode structure and 4) its cooling mechanism, *etc*. The HPGe detector is cooled by liquid nitrogen. The BEGe detector has larger efficiency and good resolution at lower energies compared to HPGe detector but the efficiency and resolution is comparable at higher energies in case of same volume detectors [44].

In our present work, we have used a p-type coaxial HPGe detector. The Ge crystal has length of 63 mm and diameter of 54 mm. It has 30% relative efficiency (quoted by the manufacturer). The specifications about the HPGe detector are summarized in Table 3.2.

Table 3.2: *Specifications of the HPGe detector used in the present work.*

Detector			Ge Crystal (mm)		Al window (mm)	
Make	Type	High Voltage(V)	Dia.	Length	Dist.[2]	Thick
BSI[3]	p-type GCD-30 185	+2600	54	63	6	0.7

[2]Distance between the crystal and the endcap.
[3]Baltic Scientific Instrument

3.5.1 Electronics setup, data acquisition and analysis

The HPGe detector has been placed at different angles, *viz.* 90°, 120°, and 137° with respect to the beamline at a distance of 5 cm from the end flange centre (target centre). The experimental setup with HPGe detector has been shown in Fig. 3.2. The applied bias voltage is +2600 V. The experimental data have been taken using a CAEN made desktop 5780M digitizer. It has 14 bit adc with maximum channels of 16k and its sampling rate is 100 MS/s [45]. It includes two high voltage power supplies of opposite polarities (± 5 kV, 300μA). Two preamplifier power supplies with ± 12 V and ± 24 V are also attached. It is well equipped with DPP-PHA (Digital Pulse Processing-Pulse Height Analyzer) firmware. It gives not only precise energy but also timing informations. The output pulse from the detector is directly fed to the digitizer input. Then the pulse is processed by digital filter and analog to digital (A/D) converters. The digital processing is taken care by dedicated algorithms in the Field Programmable Gate Arrays (FPGAs). The PHA algorithm corrects ballistic effect and manages the pile-up of online acquisition [45]. The primary analysis has been done using MC^2 analyzer [46]. Later, we have used the INGASORT offline software [38] for further analysis.
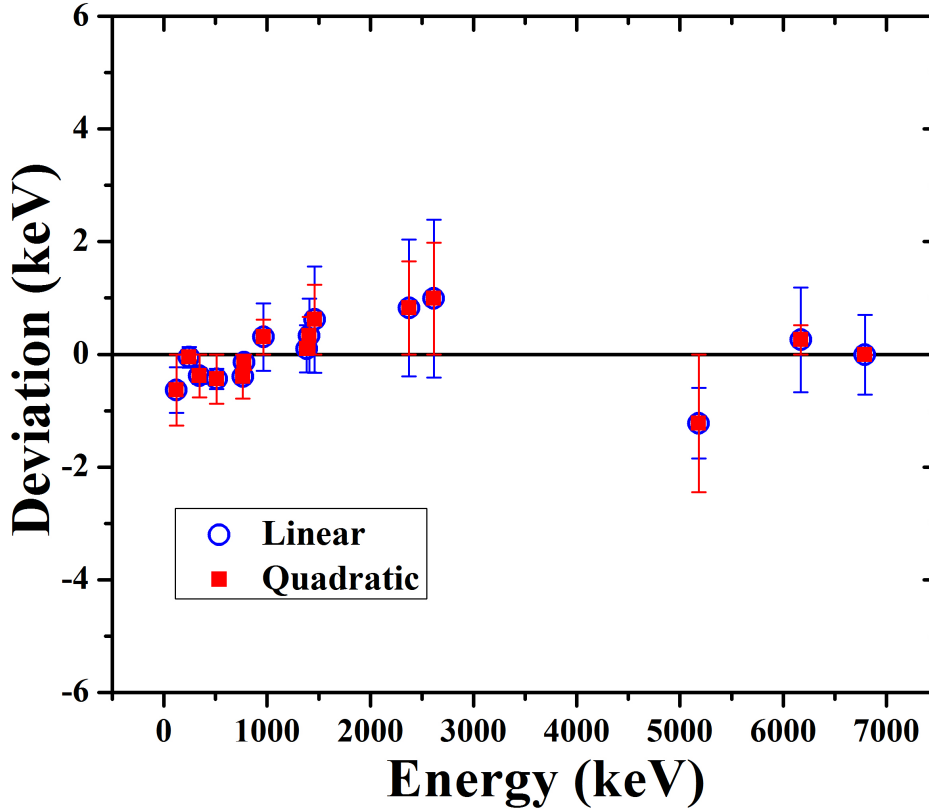
Figure 3.8: *Deviations (keV) from the linear and quadratic fit to the calibration data points of the HPGe detector are plotted.*

3.5.2 HPGe characterization

3.5.2.1 Energy calibration

The detector is calibrated using the data with a laboratory γ-ray source ^{152}Eu and the γ-rays emitted from a resonant level in ^{15}O (7.556 MeV) [39]. The in-beam data at an angle of 90° have been used for calibration. The data points are fitted using both linear and quadratic equation. The calibration plot has been given in Fig. 3.8. From the figure, it is clear that the linear and quadratic fits both are nearly equivalent in case of HPGe detector dissimilar to the BEGe detector. The deviations are similar in both cases but the error bars are less in case of quadratic fit to the data points. So, the HPGe detector follows almost linear behaviour up to 7 MeV.
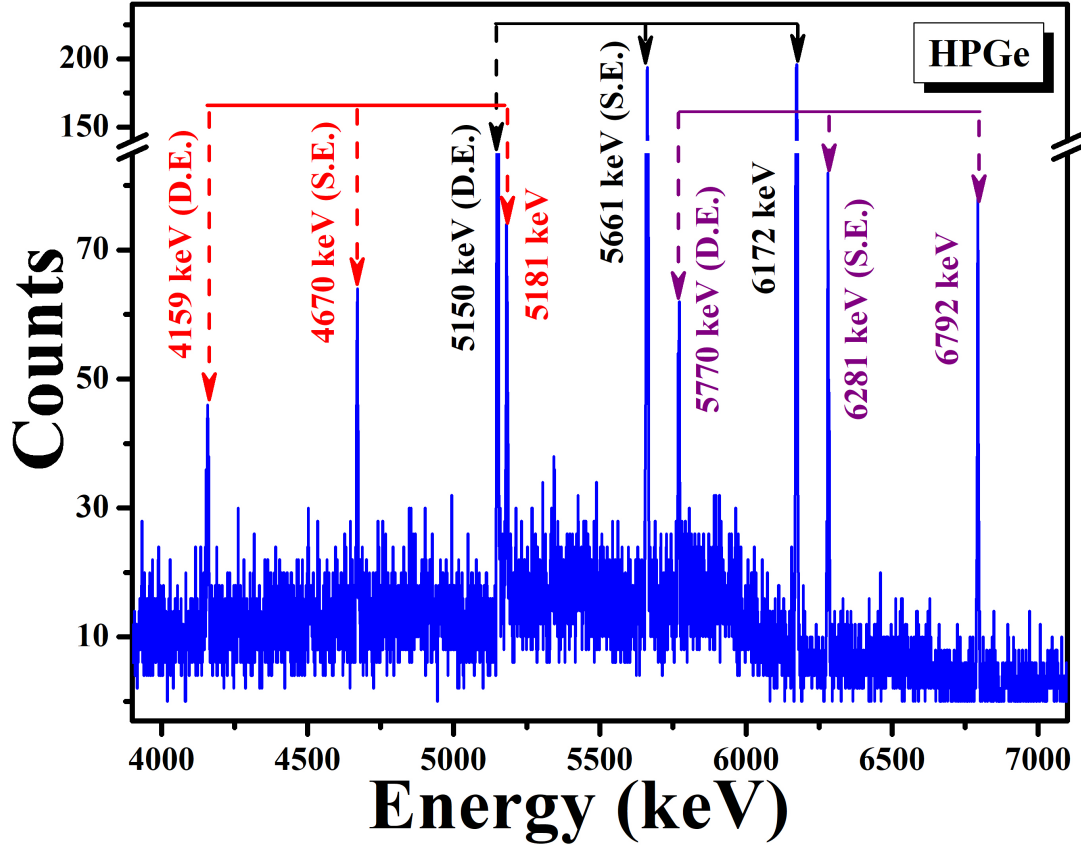
Figure 3.9: *Typical high-energy part of γ-ray spectra from $^{14}N(p,\gamma)^{15}O$ resonance reaction at E_p^{lab}= 278 keV for the HPGe detector. S.E. and D.E. denote single escape and double escape peaks, respectively.*

3.5.2.2   Energy resolution

The energy resolution of the HPGe detector is defined as similar to which is described earlier in section 3.4.2.2. In case of the HPGe detector, we do not have the 0° in-beam data which is considered to have minimum broadening. So, we have plotted the FWHM vs. $\sqrt{E}$ up to 2.615 MeV only. These data points are fitted with a straight line $0.86(8)+0.034(2)*\sqrt{E}$ with a reduced $\chi^2 = 0.01$. The FWHM at 1.408 MeV of ^{152}Eu is = 2.07±0.02 keV.

3.5.2.3   Escape peaks

In Fig. 3.9, a typical γ-ray spectra of the high energy region for gammas emitted from the resonance state has been shown. We have marked the single escape (S.E.) and double escape
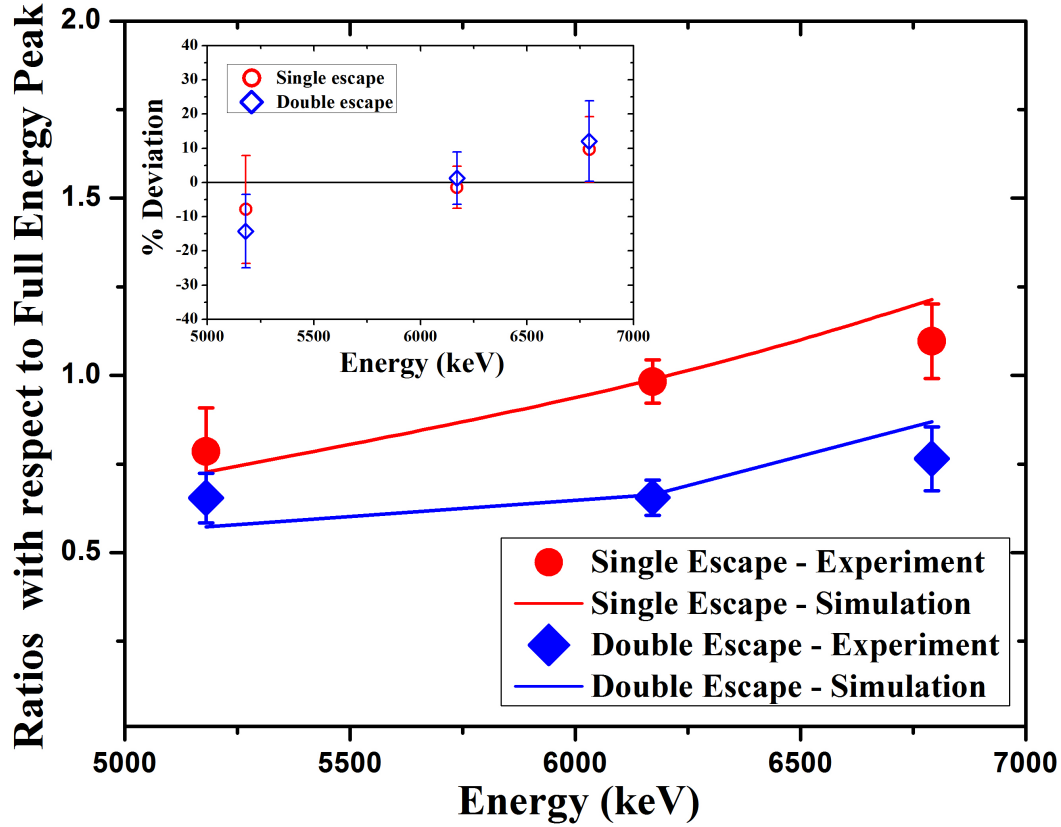
Figure 3.10: *The ratios for S.E. and D.E. with respect to F.E. as a function of γ-energy for the HPGe detector have been plotted here. The percentage deviation of the experimental value from simulation is shown in the inset figure.*

(D.E.) peaks in the figure. Here, the ratios of the escape peaks show the energy dependence (see Fig. 3.10). As the length of the Ge crystal of the HPGe detector is larger than that of BEGe detector, the intensity of the S.E. peak is higher than D.E. peak in case of HPGe detector. Another interesting fact is that the intensity of the F.E. peak is higher than S.E. and D.E. peaks in case of HPGe here (ratios $\leq$ 1 in Fig. 3.10).

3.5.2.4 Absolute efficiency

The absolute efficiency of the HPGe detector at low energy region has been determined using ^{152}Eu source with known strength. At higher energy region, the intensities of γ-rays from the resonant levels in ^{15}O (7.556 MeV) [39] have been used. The efficiency data at higher energy

have been normalized at 1.408 MeV. In case of HPGe detector, we have used the data at an angle of 120°. The typical absolute efficiency value at 6.7 MeV is 3.15e-04±7.69e-05.
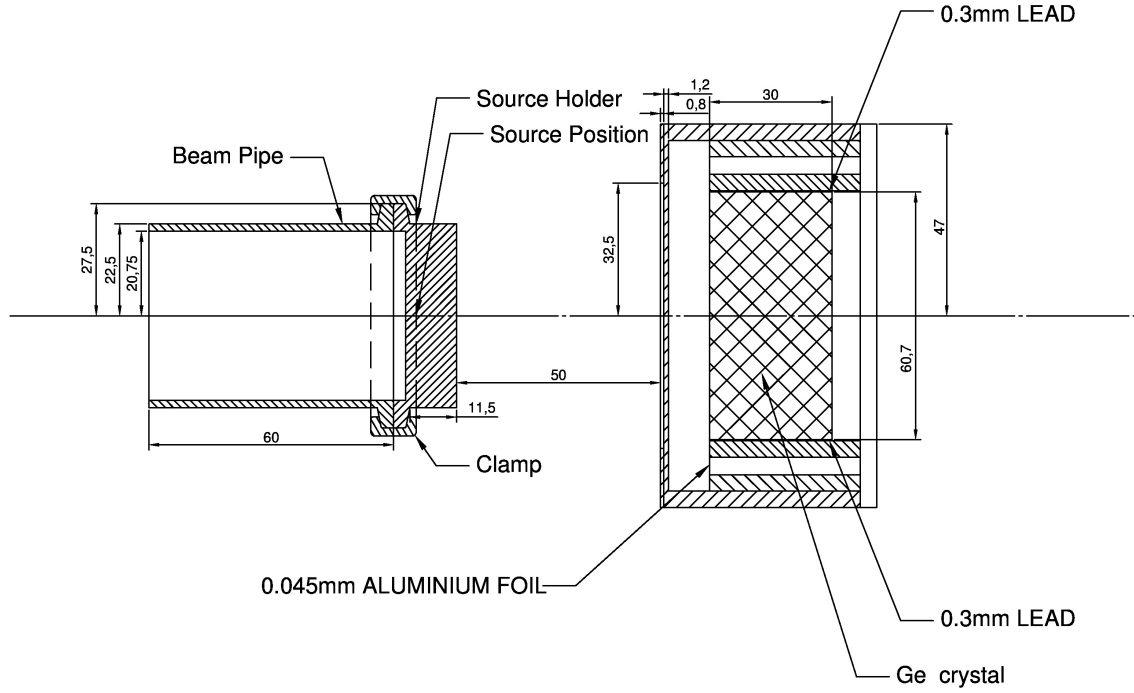
Figure 3.11: *The internal structure for holding the Ge crystal: as provided by the manufacturer for the BEGe detector, source holder, and beam pipe geometry, are shown in this figure. These specifications are used in the simulation.*

3.6   Monte Carlo simulation

In case of experimental efficiency calibration at higher energies with γ-rays emitted from in-beam resonance, we have found the beam-spot to show a shift from the centre of the target (the position of the ^{152}Eu source during off-beam measurements). Due to this reason, simulation has been done to match the ^{152}Eu and in-beam resonance data for determination of the efficiency calibration of the detector over the whole energy range including the exact experimental conditions (the target position, the target holder geometry, *etc.*).
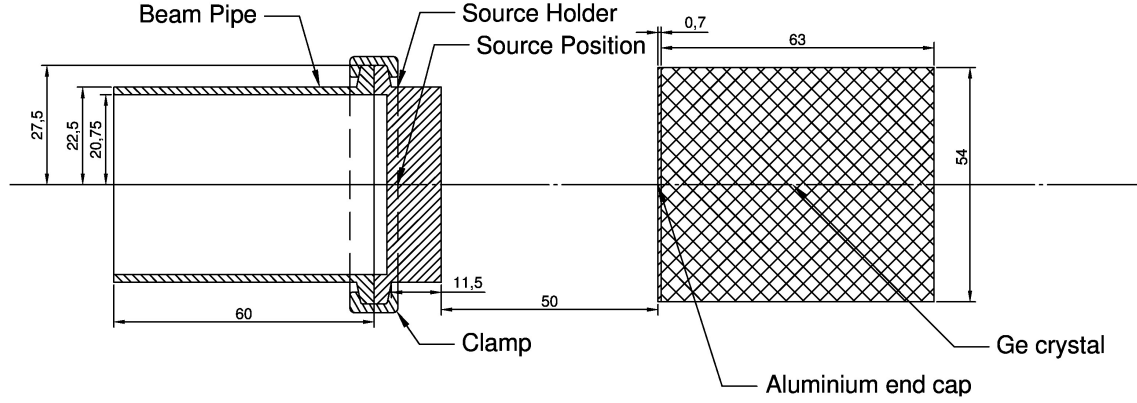
Figure 3.12: *The internal structure for holding the Ge crystal: as provided by the manufacturer for the HPGe detector, source holder, and beam pipe geometry, are shown in this figure. These specifications are used in the simulation.*

Here, we have used the Monte Carlo code GEANT4 [47] to study the response of the detectors. GEANT4 is a toolkit to simulate the passage of particles through matter. It comes pre-configured with many standard options and examples for a user to modify. The simulation has been done using a series of GEANT4 classes like detector construction, material building, particle and physics process definition, particle tracking, event action, *etc*. We have created the geometry as fully and as accurately as possible. All the beam line components like end flange, beam pipe, clamp, *etc*. are considered in detector construction class. The γ-particles are randomly generated by a particle generator G4ParticleGun. Then the γ-particles are tracked through the detector volume. To generate the energy spectra, five to ten million γ-particles are thrown isotropically on the front face of the detector. The energy deposition is recorded step-by-step using the stepping action class and finally added by the event action class. For

electrons and positrons, the process of ionization, multiple scattering and bremsstrahlung are included in the physics list class. Similarly, the photoelectric effect, Compton scattering and the pair production have been considered for γ-rays. Experimental threshold and energy resolution values are incorporated properly in the simulation to reproduce the experimental spectra.

3.6.1   Detector geometries

The BEGe detector and HPGe detector are simulated with the geometries and specifications provided by the manufacturer. The details about the internal structure of the two detectors are mentioned in Table 3.1 and 3.2. The complete geometries used in the GEANT4 simulation have been shown in Fig. 3.11 and Fig. 3.12, respectively.

3.6.2   Source holder and beam pipe geometry

Here, we have included the detailed informations in the simulation regarding the source holder, the clamp to bind it to the beam pipe and the part of the beam pipe through which the gammas have to travel to reach the detector. The same source holder and beam pipe geometry have been used in case of both the detectors. The details about the source holder and beam pipe geometry have been given in Table 3.3 and Fig. 3.11.

Table 3.3: *Specifications of the source holder and associated parts. Please see Fig. 3.11 for nomenclature.*

Item Name	Detail Specifications (cm)		
	Length	Diameter	
		Inner	Outer
Source/Target holder	1.150	0.0	2.250
Clamp	0.600	2.750	3.250
Beam pipe	6.000	2.075	2.250
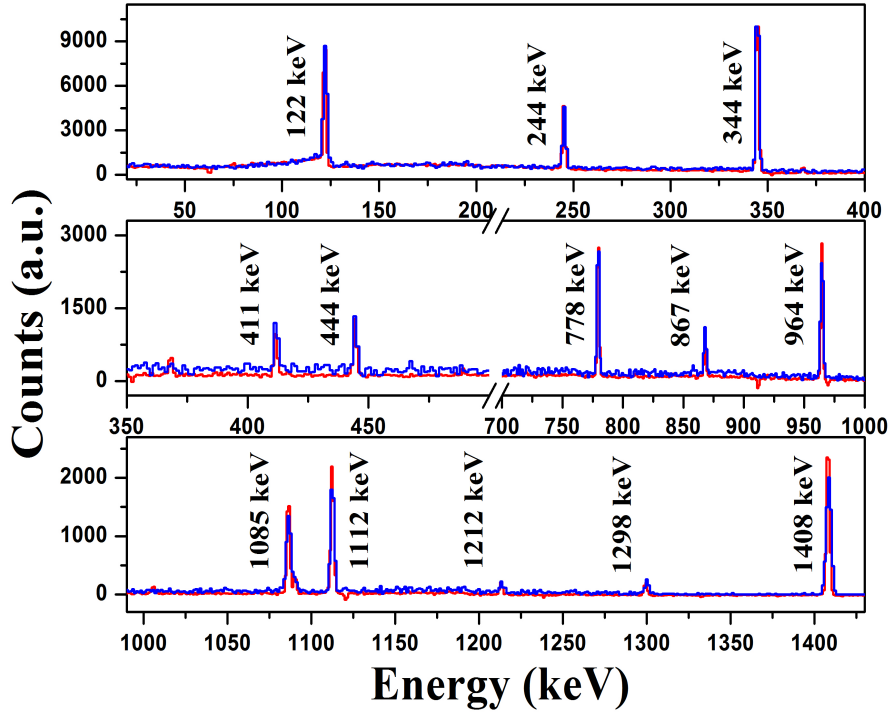
Figure 3.13: *Comparison of experimental and simulated spectra at an angle 50^0 of ^{152}Eu for the BEGe detector. The experimental and simulated spectra are drawn with red and blue curves, respectively.*

3.6.3 Comparison of experimental data with simulation results

The γ-ray spectra for BEGe detector generated from simulation with ^{152}Eu γ-ray source are shown in Fig. 3.13. Here, we have taken the intensities of γ-rays from ENSDF data library [41]. For comparison, the room background subtracted γ-ray spectra of ^{152}Eu have been plotted in Fig. 3.13. In case of HPGe detector, the simulated spectra with ^{152}Eu source have also been compared with experimental spectra (check Ref. [48]).

The γ-rays from the resonance state 7.556 MeV of ^{15}O are thrown randomly to get the simulated spectra. The BEGe in-beam resonance spectra at an angle of 50° have been compared with the simulated one in Fig. 3.14. The statistical consistency check has been performed on a point-by-point basis for the data points in Figs. 3.13 and 3.14. The statistical uncertainties of the simulated points are always within 1σ level from the experimental points.

The absolute efficiency for the BEGe detector has been determined both with experimental
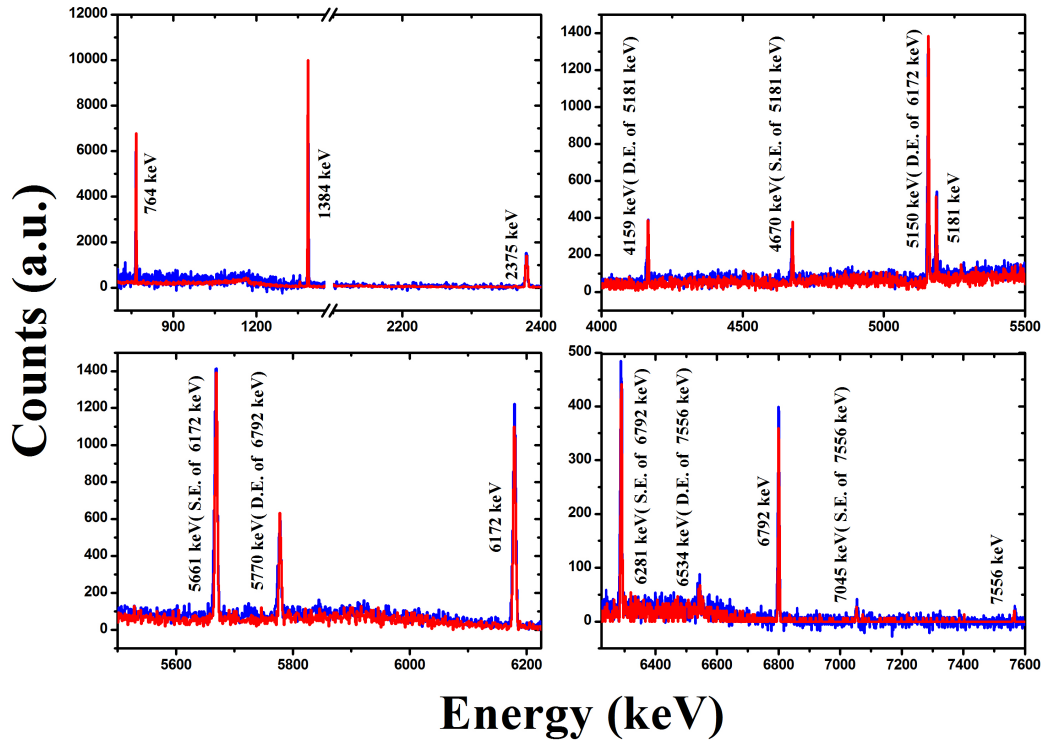
Figure 3.14: *Comparison of experimental and simulated in-beam spectra at an angle 50º for the BEGe detector. The experimental and simulated spectra are drawn with red and blue curves, respectively.*

data and via simulation over the whole energy region from 0.122 MeV to 7 MeV for the present setup. We have calculated the percentage deviations between experimental efficiencies and simulated values using the formula 3.1,

$$Deviation(\%) = (eff_{exp} - eff_{simu})/eff_{exp} * 100 \tag{3.1}$$

The plot has been shown in Fig. 3.7. The deviations are mentioned in the inset of Fig. 3.7. Finally, with the same detector configurations, absolute efficiencies of the BEGe and HPGe detector have been determined for bare point sources at 0° at a distance of 5 cm from the detector front face without any target chamber in between (see Ref. [31]).

Chapter 4

Targets

4.1 Introduction

In a laboratory, nuclear reactions take place by bombarding a suitable target with a suitable beam. Targets are one of the important parameters in nuclear physics especially nuclear astrophysics experiments. The targets have been prepared and characterized with special care and attention [1]. Mainly two kinds of targets are used in nuclear astrophysics experiments – solid targets and gaseous targets. The thickness of the solid target depends on which kind of measurements is going to take place in the laboratory. Different kinds of targets and preparation methods have been discussed in details one by one in the sections below.

4.2 Solid targets

Solid targets are mostly prepared by rolling from a pellet or a thick shit, evaporating or sputtering in vacuum onto a backing or substrate. We can also prepare a solid target by ion implantation. Depending on our requirement, target may be self-supported target or thin or thick target with

backing. Here, I briefly discuss the methods of preparing evaporated target, sputtered target and implanted target respectively.

4.2.1   Evaporated targets

Evaporated targets are frequently used in nuclear physics experiments. Many materials have been evaporated to make self-supporting targets onto a substrate such as $BaCl_2$ and NaCl, *etc*. The substrates are dissolved into the water after evaporation. In case of targets where this method is not feasible, the target materials are evaporated onto a very thin (~ 10 μg/cm^2) carbon foil. If the targets have to go through high beam current load, then one should evaporate the target material onto thick backings of high Z material with large melting points [6]. In evaporation method, we generally heat the sample material which kept in a vacuum chamber, and then the atoms are evaporated from the sample material and deposited on the substrate. After that we extracted this thin film layer from the substrate and can be used later as a target in nuclear physics or nuclear astrophysics experiments. This is known as thermal evaporation method. Instead of heating the sample material, we can also use electron gun for evaporation. A beam of electron is allowed to fall on the sample by a magnetic field following a circular path. The electron energy is then converted into heat energy after stopping in the crucible material. The target atoms are deposited in the required backing materials. The thickness of the target is determined by a quartz monitor. A schematic diagram of electron gun evaporation system is given below 4.1.

4.2.2   Sputtered targets

Sputter deposition is also a physical vapour deposition process for depositing thin films, sputtering means ejecting material from a target due to the bombardment of the target by an energetic particles and depositing it on a substrate [50]. Here the target is used as the source material and substrates are placed in a vacuum chamber and are pumped down to a prescribed process pressure. An axial magnetic field along the ions direction is also applied to increase the efficiency of the system. Because of that, it is also known as magnetron sputtering method. Sputtering starts when a negative charge is applied to the target material causing a plasma or glow discharge
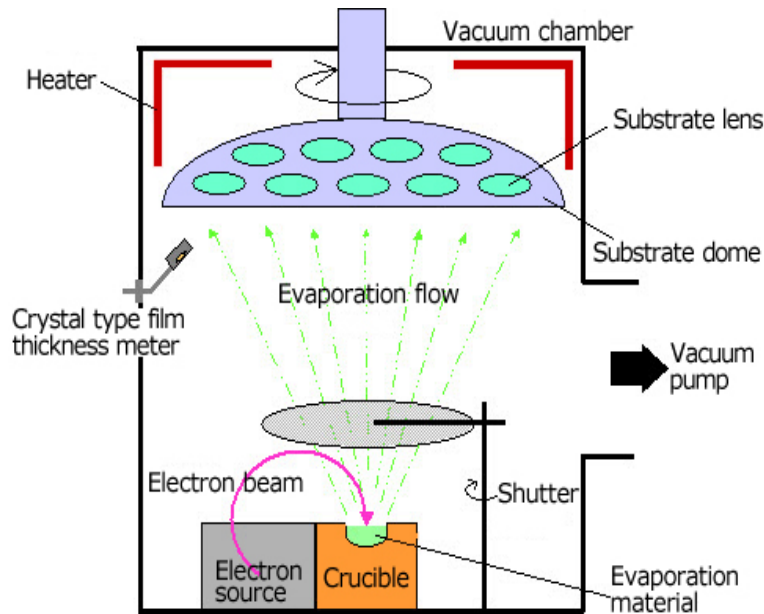
Figure 4.1: *Schematic diagram of electron gun evaporation method. The image is taken from Ref. [49].*

in the chamber. Now positive charged gas ions generated in the plasma region are attracted to the negatively biased target plate at a very high speed. This collision creates a momentum transfer and ejects atomic size particles from the target. These particles are repelled from the target and deposited as a thin film into the surface of the substrates. Then we extracted this from the substrate and used it as a target for nuclear reactions. There are some special features of the sputtering technique. Magnetron sputtering can be done in two methods – DC (direct current) sputtering and RF (radio frequency) sputtering. In DC sputtering, only conducting target materials have been used. But, in case of RF sputtering both conducting and non-conducting materials have been used. The schematic representation has been shown in Fig. 4.2.

- The stability of these targets (*i.e.*, evaporated & sputtered targets) is good but the basic problem of these solid targets is purity. So it will give high background at relatively higher energy.

- When these kinds of targets are placed over high beam load ($\sim$ several μAs) in low cross-section measurements, the target deterioration is really faster compared to implanted targets.
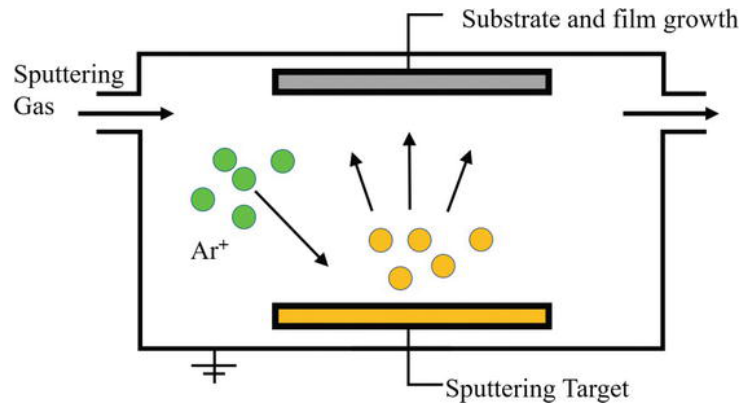
Figure 4.2: *Schematic diagram of sputtering method. The image is taken from Ref. [51].*

4.2.3 Implanted targets

In certain situations, evaporated and sputtered targets are unsuitable in nuclear astrophysics studies. To get a stable and pure solid target, implantation method has been adopted by low energy nuclear astrophysicists. Details about the implanted targets are discussed below.

4.2.4 Gas targets

Due to several advantages compared to solid targets, it is often desirable to use gas targets. One advantage is that the gas targets are chemically pure especially for noble gases like Ne. In a simple way, the gas target system is made by putting the gas in a cell with ultrathin foil windows. The cell allows only the ion beam to enter and exit and the reaction products to exit and to be detected. But in presence of entrance foil, the beam quality deteriorates due to straggling. As the foil is very thin, it ruptures due to continuous heating by the ion beam. So, it limits the gas pressure and ion beam current [6]. In presence of the window material, it induces unwanted background events also. So, the problem with gas targets in presence of thin window, has been reduced in windowless gas target system.

Windowless gas target have been developed in which the window is replaced by one or more aperture through which the beam passes. These windowless gas targets are known as differentially pumped gas target. The pressure in the target chamber is about 1 torr and approximately

(a) GAS TARGET WITH FOIL WINDOWS

(b) WINDOWLESS DIFFERENTIALLY PUMPED GAS TARGET
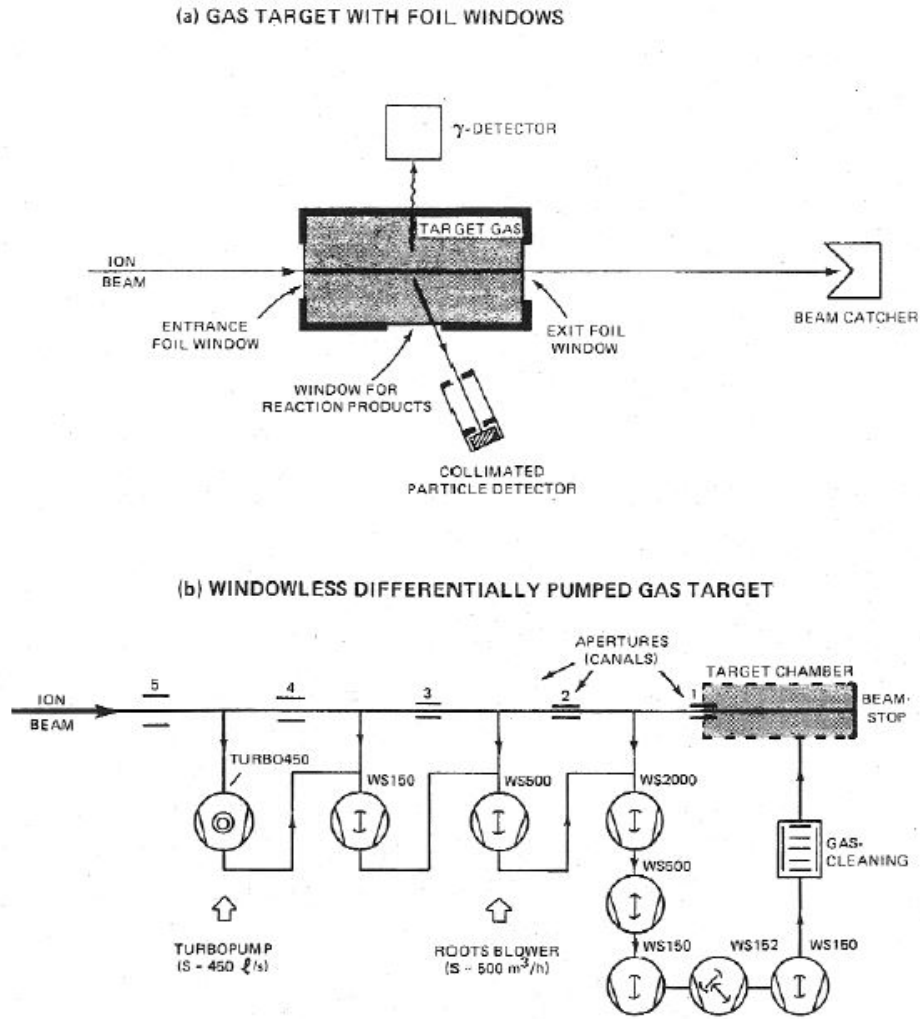
Figure 4.3: *Schematic diagram of two kinds of gas target systems – (a) gas cell with ultrathin window, (b) gas target with differentially pumped windowless system. The image is taken from Ref. [6].*

10^{-6} torr at outside of the chamber. To reduce the background reaction, we have to ensure that ion beam does not hit any of the apertures. So the aperture diameter will be greater than the beam diameter. The high pressure region of the target system should be kept as small as possible. A schematic diagram of differentially pumped gas target has been shown in Fig. 4.3. The most advanced gas target system which people are used now a days, is supersonic gas jet [52]. In this system, target gas at high inlet pressure (several torr) flows through a laval nozzle (around 1mm diameter at the neck) into a vacuumed chamber in which the static pressure is several order of magnitude lower. For such condition, the thermal energy of the gas transferred to a large extent into a kinetic energy of the collective gas flow, forming a geometrically confined supersonic jet

stream.

But with gas targets, there are two main problems –

- Sometime pure enriched gas which we want for the reaction is not commercially available. So if we used these types of gas then for high energy, background reaction will increase so it will hamper the original reaction cross-section. As example, for ^{14}N, we have a high background from ^{15}N(p,$\alpha\gamma$)^{12}C at energy E$_p$ > 0.4 MeV.

- Most of the accelerator centres do not provide such type of arrangements for using the gas target facility.

4.3   Implanted targets

As mentioned earlier due to certain limitations with evaporated and sputtered targets and also with gas targets, implanted targets are frequently used in nuclear astrophysics experiments. Implanted targets are isotopically pure and enrich and they are really stable under long time high current ion beam bombardment. In case of implantation, the target ions are accelerated. These accelerated ions are mass separated by using an electromagnetic ion separator. Then only isotopes of interest are projected onto a suitable backing. Finally, target nuclei are implanted into the backing. The voltage of acceleration determines the ion range in the substrate and it also ensures the effective target thickness. During the implantation process, the backings are water cooled due to high beam current. There are few limitations in case of implanted target which are mentioned below –

- It is not possible to make the target thickness large enough in implantation process due to sputtering from the backing material.

- The range and mobility of the implanted ions inside the substrate, the number of incident ions per unit area, and the substrate temperature limits the thickness of the implanted target.

4.3.1 Target backings

In case of charged particle reaction, the target materials are deposited on some backing except self-supporting and gaseous targets. Some requirements for the backing materials are – (a) the backing does not provide any unwanted events under ion beam bombardment, (b) the surface area of the backing material should be large enough to dissipate heat as quickly as possible, *etc*. These are general criteria for backings used in any evaporated and sputtered targets. In nuclear physics, we generally select heavier elements as a backing material because of its high stopping power ($-dE/dX$) and also for having higher Coulomb barrier leading to lower reaction yield at a particular energy. But in case of implanted targets, even for higher atomic number (Z) value which one is the best choice depends on several factors.

The basic criteria of a good backing are that it has low sputtering yield and high saturation value. The materials which are generally used as substrate for ion implantation are tantalum (Ta), gold (Au) and copper (Cu), *etc*., due to their high Z value and high melting points and especially low sputtering yield. Now, one can use the software TRIM [53] to calculate the sputtering yield for any pair of implanted ion and substrate. Here, as an example we have plotted the sputtering yield of ^{14}N on Ta, Au and Cu respectively. The plot is given below (see Fig. 4.4). We can see that for Ta, sputter yield is much smaller than Au and Cu. Now in the case of saturation limit of the ions, it varies inversely with the sputtering yield. So less sputter yield means higher saturation limits of the incoming ions. So, for ^{14}N ions, Ta has higher saturation limits and low sputtering yield than Au and Cu. Because of that, we can use Ta as backing material. In many of the other targets also Ta is used as a backing material because of its lower sputter yield and higher saturation limits. There are also some cases where people use another material like Au instead of Ta. Because, in this case, Au produced least amount of beam induced background than Ta.

- Here, we have used Ta backings with thickness 0.30 (5) mm. The size of the Ta backing is 2.5 cm $\times$ 2.5 cm.
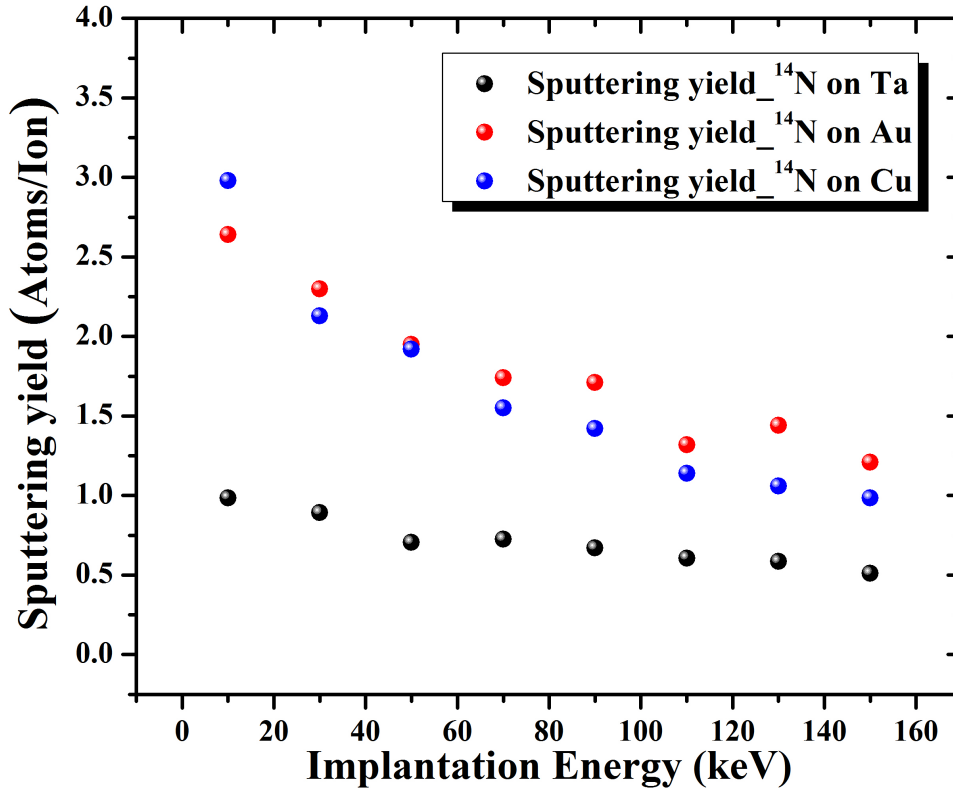
Figure 4.4: *Sputtering yield as a function of implantation energy varying substrate materials. The figure is plotted with the help of TRIM [53] simulation software. In case of ^{14}N, the sputtering yield is very low for Ta compared to Au and Cu. So, we have chosen Ta as the backing material for implantation.*

4.3.2 Implantation energy

Depending on the implantation energy, the spatial distribution of implanted ions changes onto the substrate surface and inside layers. The implanted ion distribution also depends on Z of both the implanted ion and substrate material. To decide about the implantation energy, we have used the TRIM [53] software to plot the ion distribution vs. depth inside the substrate as a function of implantation energy. So, we have calculated the ion distribution of ^{14}N onto Ta backing with varying energy from 40 - 140 keV. The variation of spatial distribution of implanted ions vs. depth as a function of energy has been shown in Fig. 4.5. At very low implantation energy (40 keV), the ions are distributed close to the backing surface and the sputtering yield is high (see Fig. 4.4). The thickness is typically 1000 A^o according to the TRIM simulation. So to get a thick
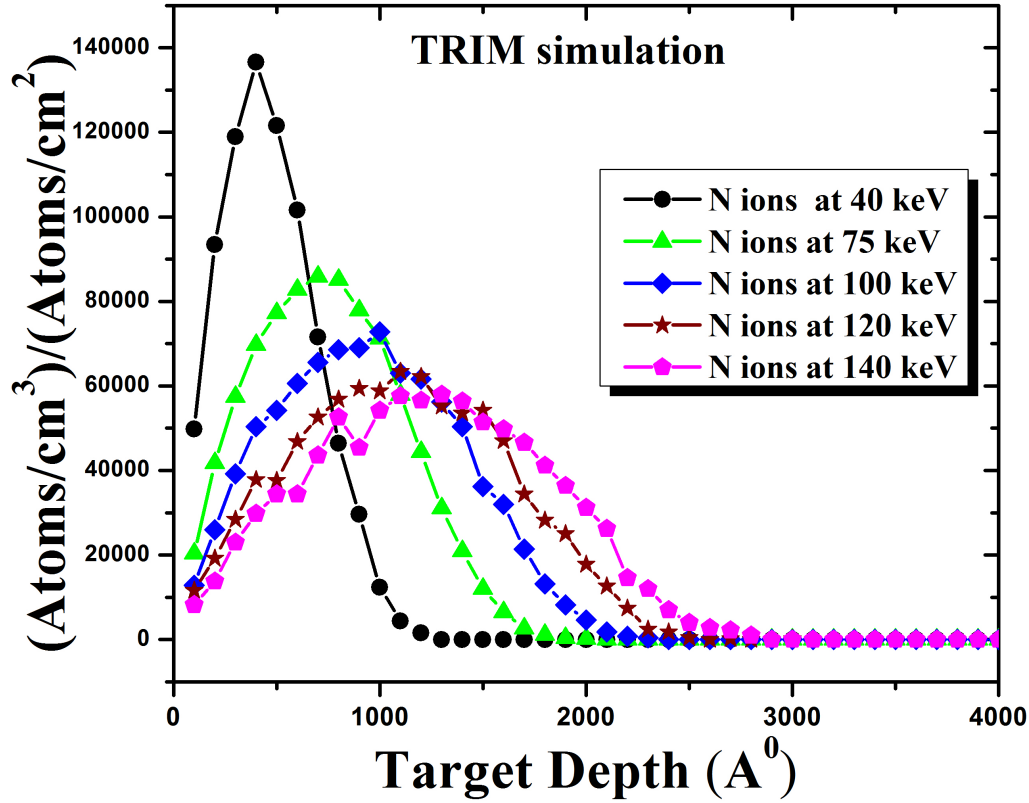
Figure 4.5: *Implantation profile of ^{14}N onto Ta backing as a function of implantation energy. The implantation energy is varied from 40 keV to 140 keV. From the figure, it is clear that the implantation profile becomes flat and broad with the increase of energy. We have chosen 50 keV and 75 keV energies for two implantation respectively.*

target we have to use higher beam energy. But there also some limitations–

- If we increase the beam energy, ion density on the surface of the target will decrease. We can see that from ion distribution curve. So it will reduce the reaction rate.

- At higher energy it may be possible that there may be some reaction occur which will induce some impurity in the target.

So, the best way to increase the thickness of the target is the implantation with dual energies which is discussed in detail in Ref. [54, 55]. Here, we do not go into details of dual energy implantation.
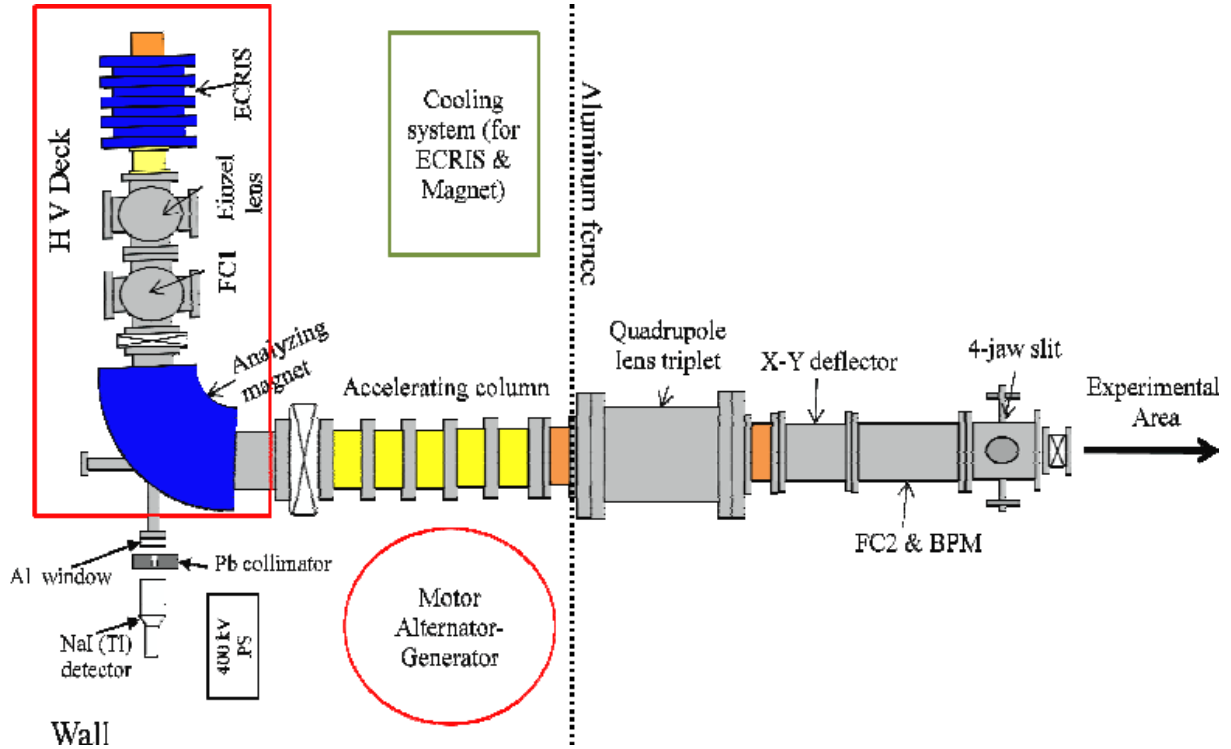
Figure 4.6: *Schematic diagram of TIFR-ECRIS ion implanter with the extended beam line. The image is taken from Ref. [30].*

- In our case, we have chosen the implantation energies of 50 keV (target I) and 75 keV (target II) for two separate implantations.

- One target is prepared using ECR source and another one using an isotope separator cum implanter [56] at Saha Institute of Nuclear Physics (SINP), Kolkata. Here, we will discuss in details about the ECR ion source below.

4.3.3   ECR ion implanter

Electron Cyclotron Resonance (ECR) ion sources are capable of producing low energy and highly charged ions. Due to this reason, they are widely used as an ion implantation source. At Tata Institute of Fundamental Research (TIFR), Mumbai, they have installed an ECR Ion Source (namely ECRIS) which consists of a Cu plasma chamber. The ECR ion source has been shown in Fig. 4.6. It consists of a permanent magnet with axial dipole and closed structure hexapolar radial magnetic fields. The magnetic field becomes minimum at centre of the plasma chamber

and that is known as the min B configuration. The microwave frequency is 14.5 GHz with maximum output of 500 W. The magnetic field of resonance at this frequency is 0.51 Tesla. The maximum voltage of extraction is 30 kV. Gases are introduced through two electrically controlled inlet valves. The extracted ions are followed by focusing Einzel lens and a 90° bending dipole magnet. The maximum high voltage applied to the deck is 400 kV. For the N_2 ion, all the charge states from 1^+ to 7^+ are available. Vacuum maintained in the plasma chamber and beam line is typically 10^{-8} to 10^{-9} mbar. The additional details have been mentioned in Ref. [30].

4.3.4 Implantation of ^{14}N

First target has been made at SINP using ^{14}N$^+$ ions with energy 50 keV (target I). The beam spot diameter is 2 mm. The implantation time is 2 hour. The implantation dose is 10^{17} atoms/cm^2. The typical current of the machine at that time is $\sim \mu$A.

Table 4.1: *Details of the two implaned ^{14}N targets.*

Place	SINP, Kolkata	TIFR, Mumbai
Instrument	Isotope separator	ECR source
Specifications	E$_{max}$=200 keV	E$_{max}$=400 keV
	I$_{beam} \sim \mu$A	I$_{beam} \sim 40\mu$A
Ion beam	^{14}N$^+$	^{14}N^{3+}
Beam energy	50 keV	75 keV
Backing	Tantalum (Ta)	Tantalum (Ta)
Backing Thickness	0.30 (5) mm	0.30 (5) mm
Implanted dose	10^{17} atoms/cm^2	7.8×10^{17} atoms/cm^2
Beam spot diameter	2 mm	2.54 cm
Implantation time	2 hour	1.5 hour

In case of second target, ^{14}N^{+3} ions from the ECR source at an energy of 75 keV (target II) are implanted onto Ta backing. Typical beam spot diameter is 2.54 cm. The ion beam is rastered throughout the Ta surface to scan the backing surface. The time duration for implantation is 1.5 hour. The typical current for ^{14}N is 40 μA. The total charge accumulated during the implantation is calculated from the Faraday cup reading. The implantation dose is 7.8×10^{17} atoms/cm^2.

The details of the two implanted target is given in tabular form in Table 4.1.

Chapter 5

Target characterization

In this chapter, I will discuss different characterization processes generally used to characterize the implanted targets. In order to use implanted targets in nuclear astrophysics experiments, the distribution profile of implanted ions in the backing should be known precisely. This profile depends on the type of implanted ion, the backing material, the implantation energy and the implantation dose. It is also important to identify the impurities present at different depths of backing material and quantify them accordingly. The characterization process is mainly of two types – 1) surface characterization and 2) bulk characterization. The surface morphology of the target and backing has been studied using surface characterization processes like X-ray Photoelectron Spectroscopy (XPS), Scanning Electron Microscopy (SEM), *etc*. The bulk properties of the target like stoichiometry, energy thickness are determined using bulk characterization processes like Rutherford Backscattering Spectroscopy (RBS), depth profiling, *etc*. These techniques are described in details in the sections below.

5.1   Surface characterization

Surface characterization is necessary to know about the contaminants in the implanted targets. As, one should try to remove the contaminant elements to minimize the number of unwanted events in low cross-section measurements.

5.1.1   X-ray Photoelectron Spectroscopy (XPS)

X-ray Photoelectron Spectroscopy (XPS) technique is used to identify the contaminants within the target material and also the target compositions. When X-ray falls on the target material each element produces a characteristic set of XPS peaks at particular binding energy values that directly identify each element that exists in or on the surface of the material being analyzed. These characteristic spectral peaks correspond to the electron configuration of the electrons within the atoms, e.g., 1s, 2s, 2p, 3s, *etc*. The number of detected electrons in each of the characteristic peaks is directly related to the amount of element within the XPS sampling volume. A typical XPS spectrum is a plot of the number of electrons detected (sometimes per unit time) versus the binding energy of the electrons detected. The experimental XPS spectrum with incident 1486.6 eV (Al K$_\alpha$) X-ray is shown in Fig. 5.1. Here, no special treatment has done with the implanted target (target I) like – ethanol cleaning or argon flushing before implantation.

In the figure, the electron kinetic energy is converted to the binding energy of the electron orbital from which it is liberated. After comparing the observed peaks in the spectrum with the reference values compiled by NIST database [57], concentrations of C, O, N, Na, F and Ta have been obtained. These elements are present in pure forms or as compounds as shown in Table 5.1. We found that 15.53% Ta is present as metallic Ta and remaining 84.47% Ta is existing as Ta$_2$O$_5$. Here, for the target II we clean the Ta backing with ethanol and take special care to reduce contamination before implantation at TIFR. The XPS results for the two targets are listed in Table 5.1 below. From the table, it is clear that special efforts should be taken to produce oxygen and carbon reduced implanted targets.
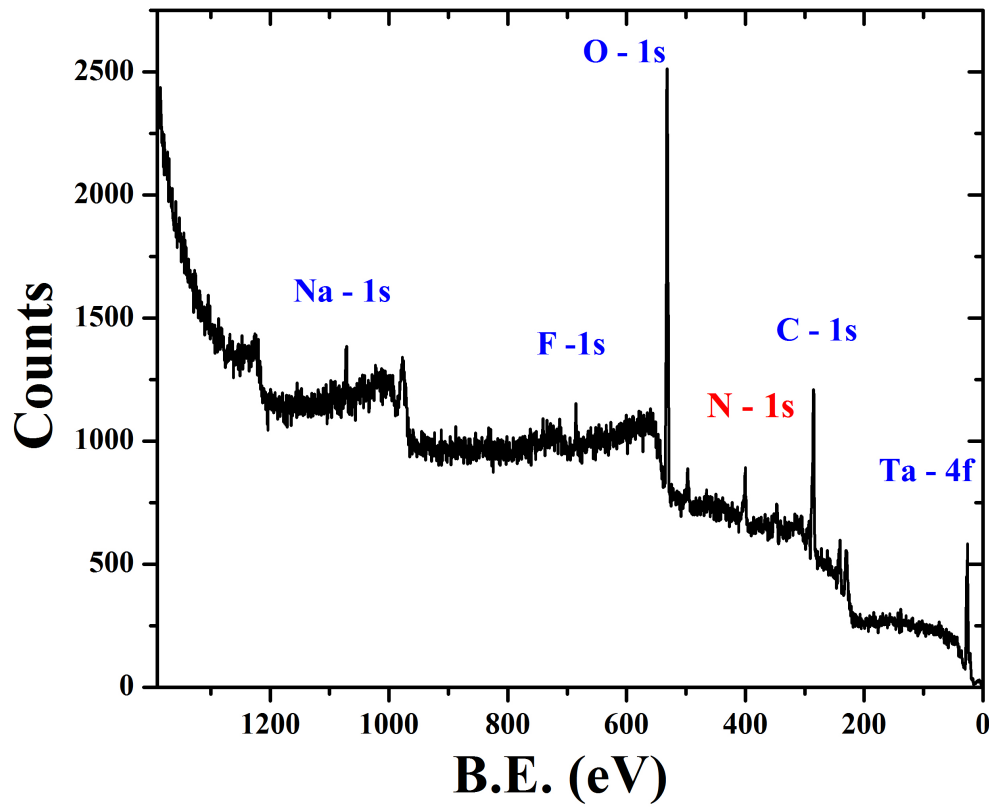
Figure 5.1: *A typical XPS spectrum with target I.*

Table 5.1: *XPS results for the two targets.*

Target I		Target II	
Elements	Relative (%) present in sample	Elements	Relative (%) present in sample
O	37.0	O	21.4
N	6.0	N	12.4
C	40.0	C	21.5
Ta	4.0	Ta	33.9
Na	7.0	Na	-
F	6.0	F	-
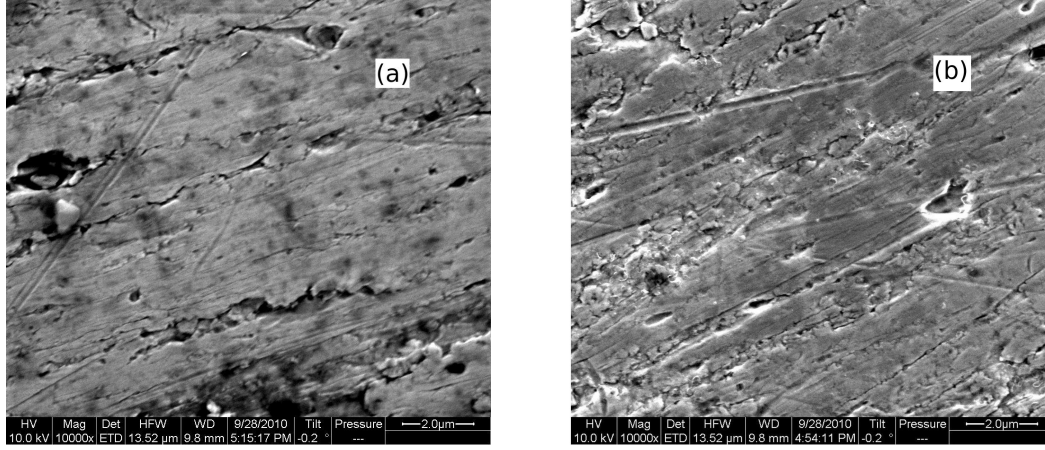
Figure 5.2: *SEM images of ^{14}N implanted target – (a) before implantation, (b) after implantation. The knobbly surface after implantation ensures the presence of implanted ions on Ta substrate.*

5.1.2   Scanning Electron Microscopy (SEM)

A Scanning Electron Microscope (SEM) is a type of electron microscope that images a sample by scanning it with a high energy beam of electrons in a raster scan pattern. The electrons interact with the atoms that make up the sample producing signals that contain information about the sample's surface topography, composition and other properties. Our second ^{14}N implanted target (target II) has been characterized by SEM at SINP, Kolkata [58]. The SEM images are shown in Fig. 5.2. From the figure, it is clear that the surface which is smooth before implantation, becomes knobbly after the implantation process.

5.1.3   Secondary Ion Mass Spectroscopy (SIMS)

Secondary Ion Mass Spectroscopy (SIMS) is a technique, used to analyze the composition of solid surfaces by sputtering the surface of the specimen with a focused primary ion beam. In our case, The SIMS measurement has been done specially to identify the impurities present inside the backing material and their yield distributions inside the backing material. From XPS measurements, it has been found that we have impurities like C, O, F and Na on the target surface. So, in the present experiment, we mainly focus on these impurities. The yield distributions of these impurities with sputtering time which is basically proportional to the target depth is shown in Fig. 5.3. The target surface has been sputtered with 5 keV caesium (Cs) ions. The typical ion
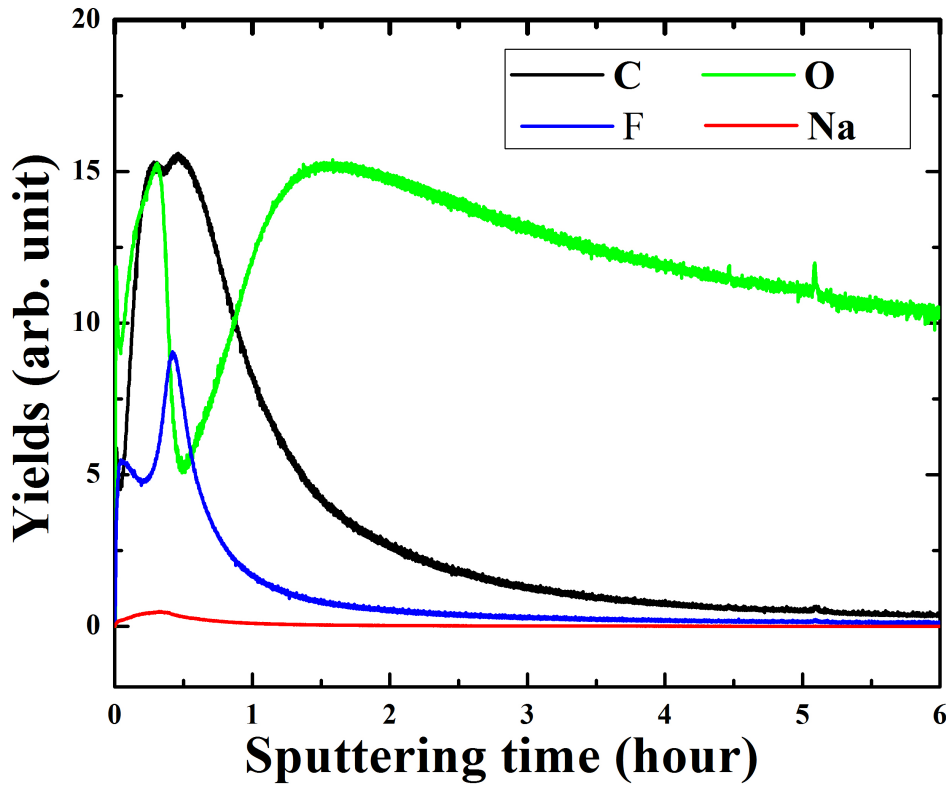
Figure 5.3: *Yields distributions of different impurities inside the backing material. After a sufficient time of Cs sputtering, the impurities like C, F and Na go away from the target. But it is really difficult to remove the oxygen impurity from the target.*

beam current was 40 nA. The result shows that the amount (proportional to the yield) of C, F and Na sharply decreased with time (*i.e.*, depth) [59]. However, even after 6 hours of sputtering, large amount of oxygen has been found inside the target. So before doing ion implantation, effort will be made to remove the oxygen impurity from the backing material.

5.2 Bulk characterization

Bulk characterization is necessary to know about the bulk properties like target stoichiometry, target energy thickness, *etc*. Here, we mainly discuss about the two processes like – Rutherford Backscattering Spectroscopy (RBS) and depth profiling (or yield curve) using nuclear resonance
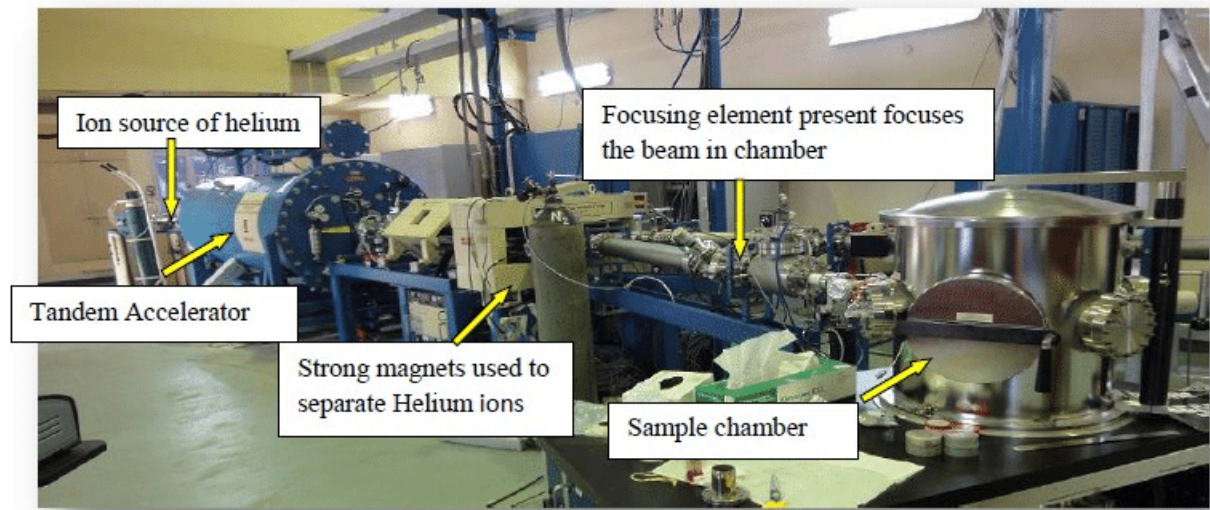
Figure 5.4: *RBS facility at IUAC, Delhi. The figure is taken from the Ref. [61].*

reaction. They are discussed one by one below.

5.2.1   Rutherford Backscattering Spectroscopy (RBS)

Rutherford Backscattering Spectroscopy (RBS) is based on collisions between atomic nuclei and derives its name from Lord Ernest Rutherford, who in 1911 was the first to present the concept of atoms having nuclei. It involves measuring the number and energy of ions in a beam which backscatter after colliding with atoms in the near surface region of a sample at which the beam has been targeted [60]. When the particles are backscattered from the elements, the energy of the backscattered particles depends on the elements from which they have scattered. There is much greater separation between the energies of particles backscattered from light elements than from heavy elements, because a significant amount of momentum is transferred from the incident particle to a light target atom. As the mass of the target atom increases, less momentum is transferred to the target atom and the energy of the backscattered particle asymptotically approaches the incident particle energy. This means that RBS is more useful for distinguishing between two light elements than it is for distinguishing between two heavy elements. So, RBS has good mass resolution for light elements, but poor mass resolution for heavy elements.

Now, we discuss about the experimental RBS techniques to measure the target composition,
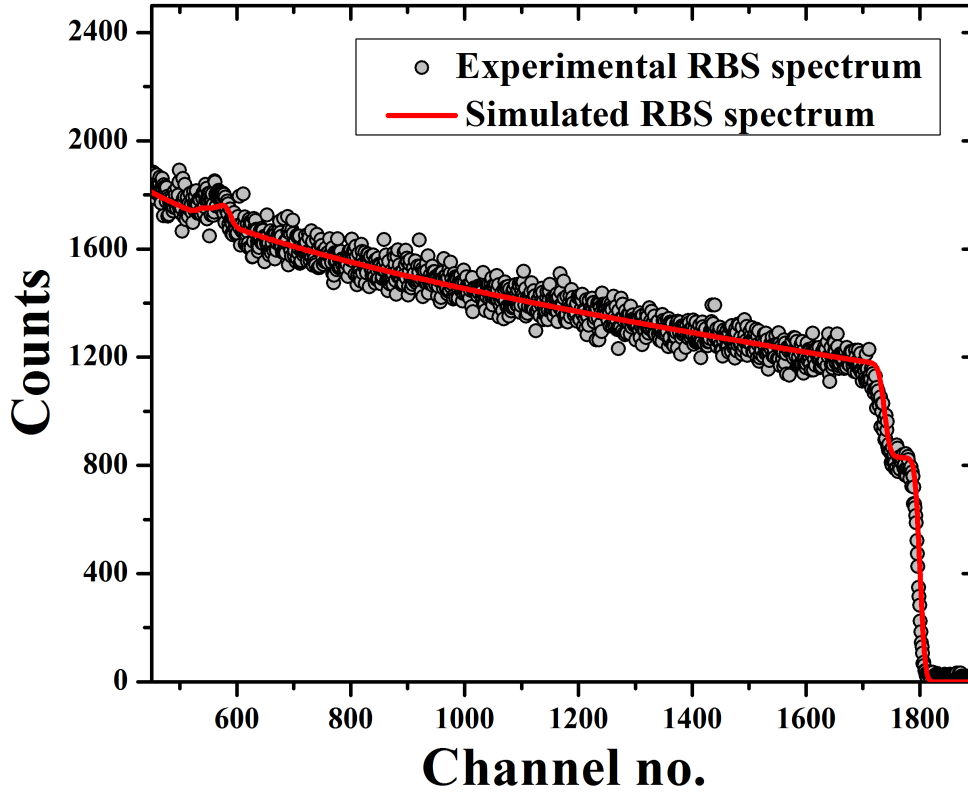
Figure 5.5: *A typical RBS spectrum of implanted target at an energy of $^4He^{2+}$ ions with 3.682 MeV. The SIMNRA fit [62] is shown in solid red line.*

i.e., the stoichiometry of the implanted target as it is an important parameter in nuclear reaction measurements. RBS has been performed at Inter University Accelerator Centre (IUAC), Delhi with the target II. The experimental setup is shown in Fig. 5.4. The $^4He^{2+}$ ions with energy 3.65 - 3.70 MeV from 1.7 MV Pelletron accelerator has been used to do the RBS measurements. Typical beam current is 12.2 nA. The scattered He ions are detected by a Si Surface Barrier Detector (SSBD) placed at 160° with respect to the beam line. RBS spectra are taken for the ^{14}N implanted on Ta and also for the bare Ta. The experimental spectrum at 3.682 MeV has been fitted with SIMNRA software [62]. The best fit of the spectrum has been obtained with the Ta/N ratio of 0.667(33) with reduced $\chi^2 = 1.0$. The experimental spectrum with SIMNRA fit has been shown in Fig. 5.5.
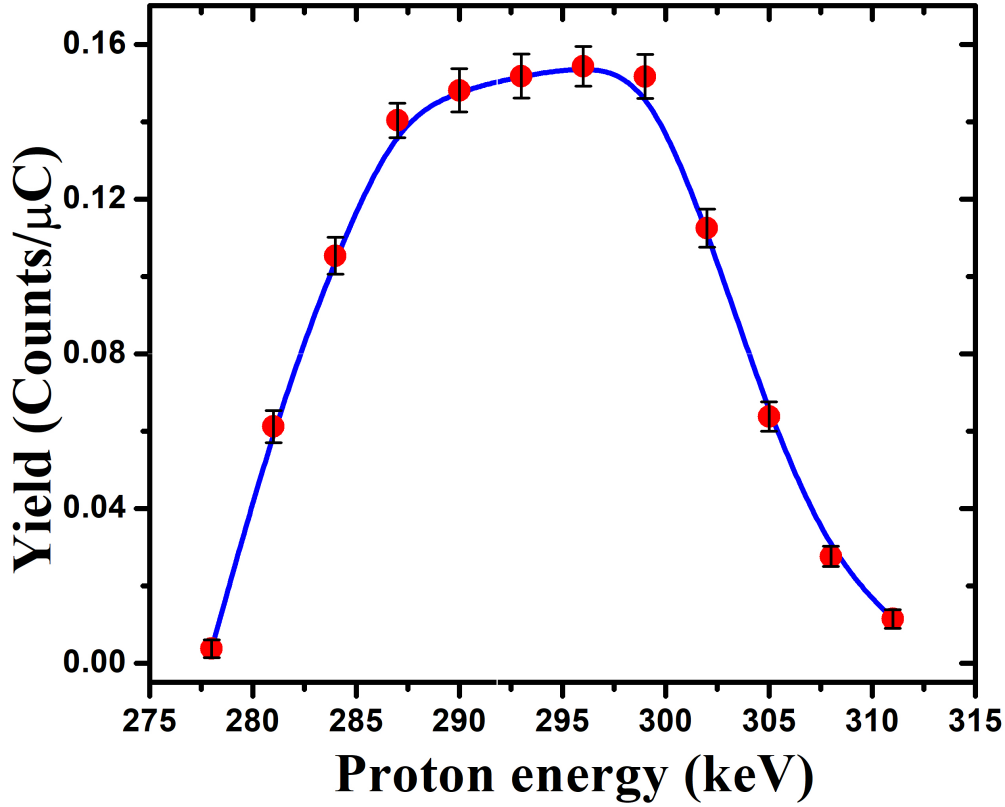
Figure 5.6: *Measured yield curves of the E_p^{lab} = 278 keV resonance on the ^{14}N implanted target using proton beam from the ECR ion accelerator [30].*

We also use another technique to determine the stoichiometry of the target. Here we use the plateau heights of the RBS spectrum to determine the stoichiometry. The stoichiometry is calculated using the formula as described in Ref. [5],

$$\frac{n}{m} = \frac{\epsilon_{Ta}}{\epsilon_N}\left[\frac{H_{Ta}}{H_{Ta_mN_n}} - 1\right] \tag{5.1}$$

Here, ϵ_{Ta} and ϵ_N are the stopping powers of 3.682 MeV ^{4}He^{2+} ions in tantalum and nitrogen respectively. The stopping powers used in Equation 5.1 are calculated from the SRIM 2013 computer software [53]. The backscattering yield from the Ta and Ta$_m$N$_n$ samples have been extracted from the plateau heights H$_{Ta}$ and H$_{Ta_mN_n}$ in the surface barrier detector energy spectra. From our measurement, the stoichiometry is, $\frac{n}{m}$ = 1.5 $\pm$ 0.1, *i.e.*, Ta/N ratio is 0.667, which is

similar to the target used by Daigle *et al.* [5] in a previous work.

The stoichiometry values obtained in two different methods are consistent with each other.

5.2.2 Depth profile or Yield curve

Target profiles or yield curves are used to measure the thickness of the active target region. We have measured the target thickness using the narrow resonance of ^{14}N(p,γ) at an energy E_p^{lab} = 278 keV. The width of the resonance is 0.99 ± 0.10 keV [63]. The proton beam is accelerated by ECR ion accelerator at TIFR, Mumbai [30]. The beam energy has been varied from 278 keV to 312 keV to get the depth profile of the implanted ions. We have plotted the yield at different proton energies. The yield is defined as the photopeak area of the most intense primary γ-ray of ^{15}O (*i.e.*, 1384 keV) populated in the resonance reaction devided by the total accumulated charge during each run. The plot has been shown in Fig. 5.6. The flat plateau of the target profile confirms the target uniformity over the active target region. From the target profile, the energy thickness of the target is determined which is actually equal to the FWHM of the profile. The obtained target thickness is 21 ± 1 keV.

5.2.2.1 Comparison of experimental depth profile with simulation

The implantation depth profile has been simulated using the TRIM simulation software [53]. Now, to compare the experimental yield profile with the TRIM simulation, we have expressed the proton energy in terms of linear thickness using the stopping power (-dE/dx) value obtained from SRIM 2013 software [53]. At first, the depth profile has been obtained with the RBS measured Ta/N ratio – 0.667 (Ta:N = 0.4:0.6). But interestingly, the profile is much wider than the simulated profile. So, we have tried to match the experimental profile by varying the ratio of Ta/N. Although by using stopping power of $\simeq$ 278 - 312 keV proton in bare Ta, the experimental yield profile varies from simulated profile especially at the falling edge part [64] (see Fig. 5.7). Next, a quick ion implantation calculator named SUSPRE [65] which has been developed by University of Surrey, Guildford, UK has been used. The experimental profile nicely matches with the SUSPRE calculated profile with bare Ta [64]. So, the target density is basically similar to
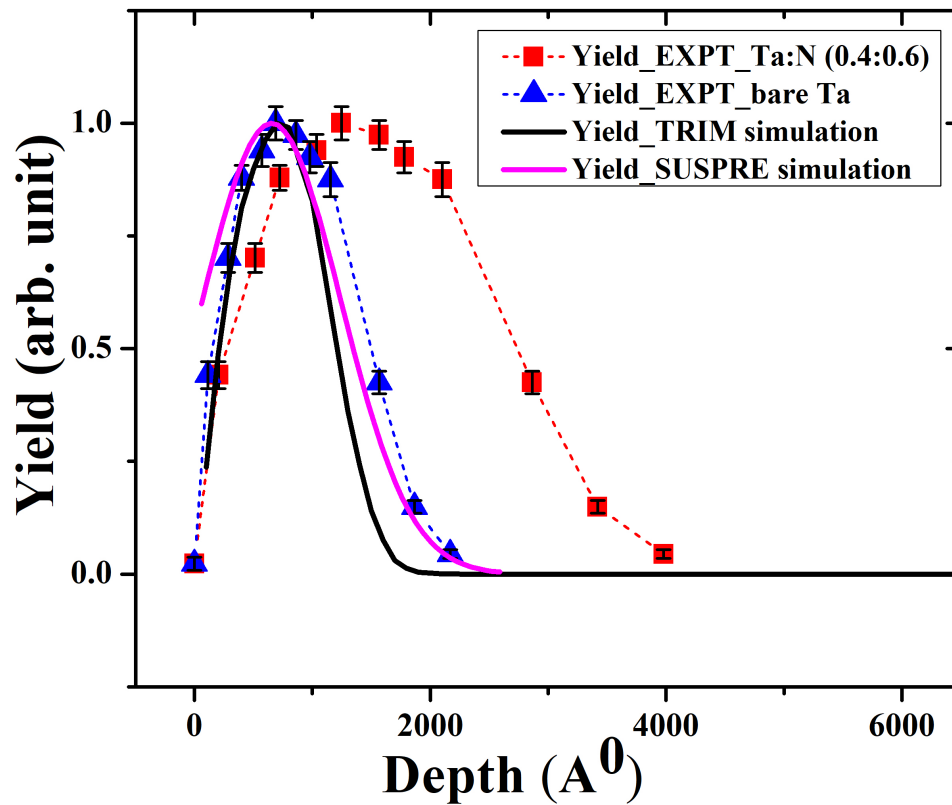
Figure 5.7: *Comparison of experimental depth profile of implanted ions with simulation using SRIM and SUSPRE software. The experimental data points are shown with error bars including only statistical errors.*

that of pure Ta, indicating the occupation of nitrogen atoms within the Ta lattice at the interstitial positions instead at the substitutional positions.

Chapter 6

Experimental results

From ^{14}N(p,γ)^{15}O resonance reaction data at E$_p^{lab}$= 278 keV, two important experimental informations have been obtained in the present work. They are – a) the resonance strength ($\omega\gamma$) of E$_x$ = 7556 keV state in ^{15}O and b) the lifetimes of the excited states of ^{15}O populated in the present resonance reaction by analyzing the centroid shifts of the associated Doppler shifted γ-rays.

6.1   Resonance strength ($\omega\gamma$)

Resonance strength ($\omega\gamma$) is a very important parameter to determine the reaction rate for resonance. In experiment, what is directly measured are experimental yields rather than the absolute cross-sections or resonance strengths. Then, from the experimental yields, one can obtain the absolute resonance strength from the thick target plateau heights. Also, one can simply obtain the resonance strengths and cross-sections relative to some absolute, carefully measured, standard resonance strength or cross-section [1]. Here, the absolute resonance strength has been obtained directly from the thick target plateau height which is described in details below.

6.1.1   Yield curve analysis

As already discussed in the section 5.2.2, the implanted target has been scanned with proton energy 278 keV to 312 keV in steps of 3 keV using the ECRIA [30] machine at TIFR. The BEGe detector was placed at 0° at a distance of 1.7 cm from the target centre at the time of experiment. The yield of a reaction at a particular incident energy is defined as,

$$Y = \frac{N_{reaction}}{N_{beam}} = \frac{N_{peak}}{B N_{beam} W \eta_{peak}} \tag{6.1}$$

where, $N_{reaction}$ is the total number of reactions that occurred and N_{beam} is the total number of incident projectiles. B, N_{peak}, W and η_{peak} are the branching ratio (probability of emission of that particular γ-ray per reaction), the total number of photons emitted by the state excited by the reaction (given by the area under the corresponding photopeak), the angular correlation, and the detector efficiency, respectively, for a specific nuclear transition. Here, the photopeak area under the 1384 keV γ-ray has been utilized to get the yield curve including all the necessary factors mentioned in Eq. 6.1. The yields have been plotted as a function of incident proton energies in Fig. 5.6.

From the yield plot, the estimated energy thickness (ΔE) of the implanted target is $\simeq 21 \pm$ 1 keV which is much larger than the energy width (Γ) of the resonance. So, for such a thick target, the resonance strength can be determined using the height of the plateau region in the yield curve. The resonance strength ($\omega\gamma$) and maximum yield for a thick target is related through the equation,

$$\omega\gamma = \frac{2\epsilon_r}{\lambda_r^2} Y_{max,\Delta E \to \infty}, \tag{6.2}$$

where, λ_r^2 is the corresponding de Broglie wavelength and ϵ_r is the effective stopping power at the resonance energy. For determining the resonance strength, effective stopping power at the resonance energy (ϵ_r) for Ta has been used in the present work as we have determined the density of implanted target similar to that of pure Ta by comparing the experimental yield profile with the SUSPRE simulated profile (see section 5.2.2.1).

The ratio of energy thickness of the target to the total width of the resonance state, *i.e.*, $\Delta E/\Gamma$ is $\simeq 21$. Now, in Ref. [1], it has been shown that if the target thickness is $\simeq 20$ times higher than the total width of the resonance, the maximum yield at the plateau is $\geq 95\%$ of the yield for an infinitely thick target. And the FWHM of the yield curve is equal to the target thickness within 0.5%. This factor has been taken into account at the time of calculation of absolute resonance strength ($\omega\gamma$).

The uncertainty in the reported absolute resonance strength ($\omega\gamma$) value has been attributed to a combination of both statistical and systematic sources. The systematic uncertainty is composed of the total accumulated charge, target stoichiometry, the effective energy and the branching ratio of the corresponding γ-ray, *etc*. After including all the uncertainties, the present value of the resonance strength is, $\omega\gamma = 12.78 \pm 0.29$(stat.) ± 0.92(sys.) meV. The measured value has been compared with the previous literature values in Table 6.1.

Table 6.1: *Comparison of experimental resonance strength determined in the present work with earlier literature values with uncertainties.*

References	$\omega\gamma$ (meV)	Error	Weighted average (Error)
1) Present work [48]	12.8	0.9	
2) Daigle *et al.* [39]	12.6	0.3	
3) Bemmerer *et al.* [21]	12.8	0.6	
4) Imbriani *et al.* [19]	12.9	0.9	12.7±0.2
5) Runkle *et al.* [20]	12.4	0.9	
6) Becker *et al.* [66]	13.7	1.0	

The weighted average of the resonance strength ($\omega\gamma_{average}$) value is 12.7 (2) meV.

6.2 Lifetime estimation

The lifetimes of nuclear levels range from $\approx 10^{-20}$s to $>10^{15}$years. There are several techniques to measure the lifetimes of the nuclear states. However, no such technique is there to cover the entire time scale. So, the techniques vary depending on the values of interested level lifetimes. The Doppler Shift Attenuation Method (DSAM) is applied for measuring lifetimes of excited

states that decay via γ-emission, in the range from 10^{-11} to 10^{-15} s, that is 10 ps to 1 fs. The interested level lifetimes of ^{15}O nucleus in the present work is of the order of fs. So, DSAM technique has been adopted here to determine the lifetimes of the excited states of ^{15}O.

6.2.1   Doppler Shift Attenuation Method (DSAM)

Doppler shifts can be seen in light as γ-rays emitted from moving nuclei in excited states that decay to lower lying states. One can use this information to measure lifetimes of these excited states via the DSAM technique. In the DSAM, an excited state of a nucleus is populated through a nuclear reaction and after that the recoil nucleus slows down in a stopping medium. So, this method relies on the Doppler shift of γ-rays and the attenuation of recoil speeds through stopping media to infer lifetimes of excited nuclear states. The DSAM only works for lifetimes that are comparable to the slowing down time of the recoil in the stopping medium.

The Doppler shifted energy depends on the initial recoil velocity (v_0), angle between the detector detecting the γ-ray and the recoiling nucleus (θ), velocity attenuation factor ($F(\tau)$) and the correction factor (P) for the finite size of the detector. The attenuation factor, ($F(\tau)$), is a function of the lifetime of the nuclear level emitting the γ-ray and the recoiling medium. The relation between the energy of the γ-ray detected by the detector at an angle, θ, designated as (E_γ^θ) and actual energy of the γ-ray (E_γ^o) is given by,

$$E_\gamma^\theta = E_\gamma^o \left[1 + \beta_0 F(\tau) P cos\theta\right] \tag{6.3}$$

where, $\beta_0 = v_0/c$.

6.2.2   Stopping power

Stopping power plays an important role in determining the lifetime via DSAM technique. The energy loss of an ion in a medium is dependent on three factors: 1) the energy of the ion, 2) the characteristic stopping power of the medium, and 3) its density. The characteristic slowing down time is defined as the time in which the initial recoil speed reaches to its 1/e value. Solid target DSAM measurements choose stopping materials such that the characteristic slowing down

time is comparable to the lifetime of the excited state. The ratio of differential energy loss and differential path length is called linear stopping power, and is defined by –

$$S_L(E) = -\frac{dE}{dx} \qquad (6.4)$$

The linear stopping power depends on the number density of electrons in the absorber or, equivalently, the absorber mass density ρ. Now, for nonrelativistic projectile energies, the electronic stopping power (*i.e.*, the contribution due to inelastic collisions between projectile and atomic electrons) is given by –

$$-\frac{dE}{dx} \approx \frac{4\pi e^4}{m_e} \frac{Z_p^2}{v^2} \left(N_A \rho \frac{Z_t}{M_t} \right) ln \left(\frac{2m_e v^2}{I} \right) \qquad (6.5)$$

Where Z_p, v, Z_t, M_t are the charge and velocity of the projectile, the atomic number and the relative atomic mass of the absorber, respectively; N_A, ρ are the Avogadro number and target density; m_e is the electron rest mass, e is the electron charge, and I represents an average excitation and ionization potential of the absorber. The equation holds if the projectile velocity is large compared to the electron velocities in the absorber atoms. Over a wide energy range, excluding very high energies where the logarithmic term in Eq. 6.5 dominates, the magnitude of the stopping power decreases with increasing projectile energy as $1/v^2$ or 1/E. A schematic diagram of stopping power vs. energy is given below.

From this Fig. 6.1 we can see that at very low energies, it is influenced by the nuclear component (dotted line) and, with increasing energy, follows the $\sqrt{E}$ behaviour predicted by the LSS (Lindhard, Scharff and Schiott) theory (dashed–dotted line) [1]. A maximum occurs when the velocities of the projectile and the atomic electrons of the absorber are comparable. For higher energies beyond the maximum, the stopping power is given by the Bethe–Bloch formula (dashed line). For nonrelativistic projectile energies, the stopping power is dominated by the 1/E dependence and decreases until v $\approx$ 0.96c, where a minimum is reached. At this point, the projectiles are called minimum ionizing. This minimum value of $-dE/dx$ is approximately constant for all particles of the same charge Z_p. Beyond this point, the stopping power increases due to the logarithmic term in the Bethe–Bloch formula.
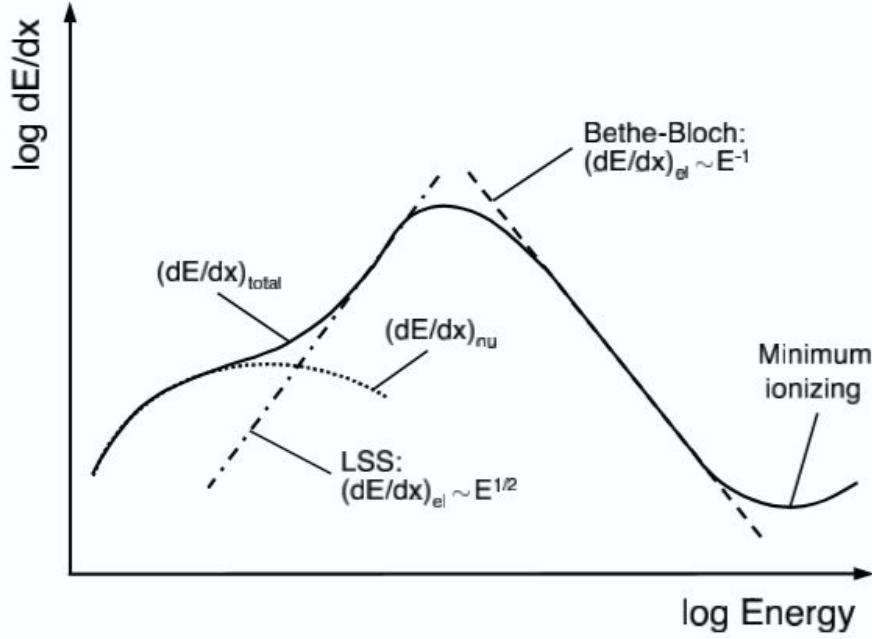
Figure 6.1: *Schematic representation of total stopping power (solid line) and different components (dashed or dotted lines) versus particle energy (adopted from Ref. [1]).*

In case of electronic stopping, it is quite easily measured. But in case of nuclear stopping, it is hard to measure especially at low recoil velocities. The main uncertainty in the lifetime estimation comes from the value of nuclear stopping power. Here, the stopping power values from the SRIM 2013 software have been taken which includes $\sim 5\%$ of uncertainty in the lifetime values.

6.2.3   Experimental F(τ) determination

To acquire the DSAM data for lifetime measurement, the proton energy was kept fixed at 293 keV. Seven different angles have been covered to take the lifetime data using both the BEGe and HPGe detector. The spectra acquired at different angles using two detectors for 6172 keV and 6792 keV have been shown in Fig. 6.2. As the reported width of the 7556 keV state (259 keV resonance state) is 0.99(10) keV [67], the associated lifetime of the state is thus 6.6×10^{-19} s. The lifeime of this state is too small compared to the stopping time of the recoiling nucleus in the backing medium. Thus, the recoil velocity is not attenuated at all during this small lifetime,
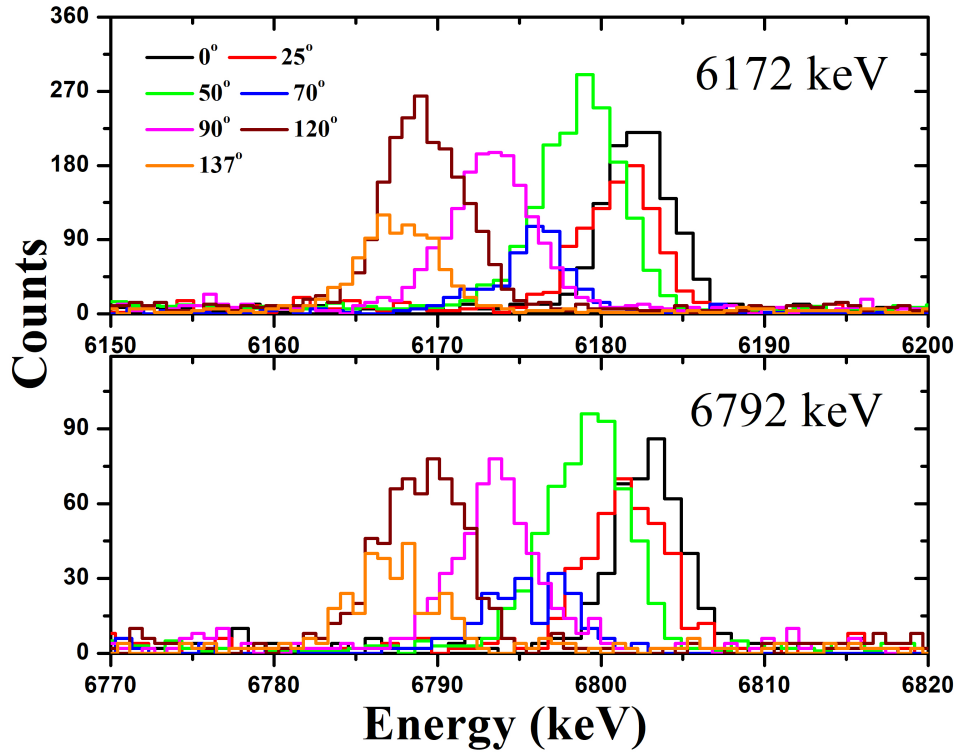
Figure 6.2: *Full energy peaks for (a) 6172 keV and (b) 6792 keV γ-rays at seven different angles of the BEGe (0°, 25°, 50° and 70°) and HPGe (90°, 120° and 137°) detector respectively.*

i.e., F(τ) = 1. Due to this reason, the lifetime of the resonance state could not be determined by the DSAM technique. However, we can utilize the shifts in the primary γ-rays emitted from this resonance level to determine the factor β_oP mentioned in Eq. 6.3. The shifts of 1384 keV γ-ray at different angles are plotted with cosθ. It has been shown in Fig. 6.3. After performing a linear fit to the data points considering F(τ) = 1, the obtained value of the factor, β_oP = 0.001738 ± 0.000343.

After that, we have used the DSAM technique to determine the lifetime of the lower excited states of ^{15}O, from where the secondary γ-rays originated. At first, the centroids of the three secondary γ-rays 5181 keV, 6172 keV, and 6792 keV at seven different angles have been determined. The Doppler shifted energies for the three secondary γ-rays have been plotted against cosθ. As I mentioned earlier, there is a shift of the beam spot from the centre of the target flange. So, the angle (θ) values have been corrected accordingly. The plots for the 5181 keV,
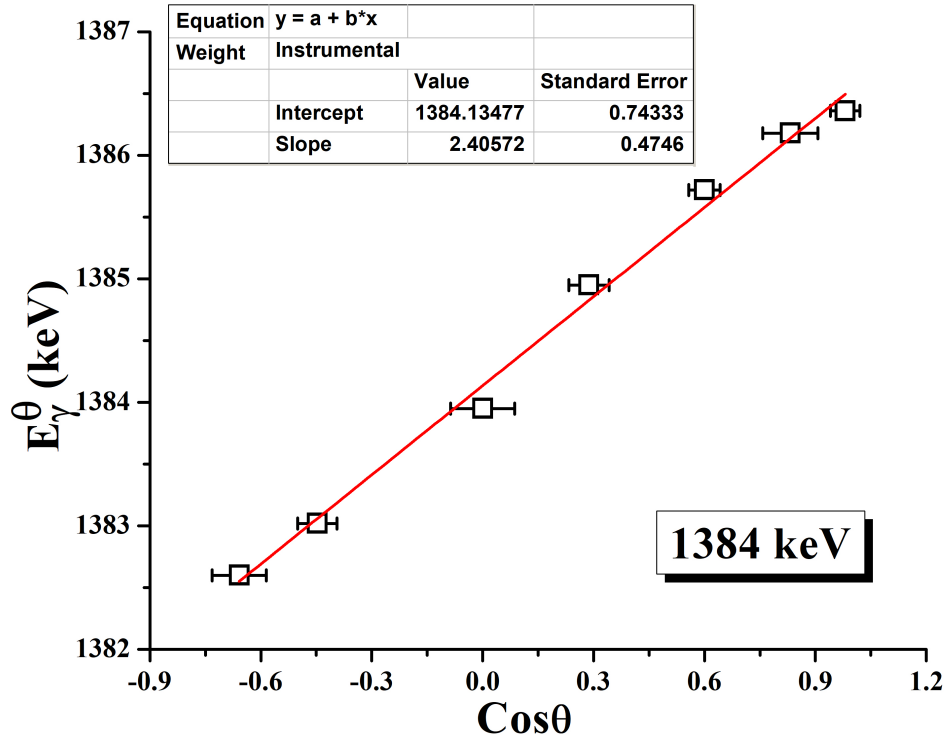
Figure 6.3: *Doppler shifted γ-ray energy (E_γ^θ) of 1384 keV γ-line plotted against cosθ, where θ is the detection angle. The solid red line corresponds to fit according to Eq. 6.3.*

6172 keV and 6792 keV γ-rays are shown in Fig. 6.4, Fig. 6.5 and Fig. 6.6 respectively. All the data points have been fitted using Eq. 6.3 including the factor β_oP which was obtained from the linear fit shown in Fig. 6.3. Next, the experimental F(τ) values for the three secondary γ-rays have been obtained (see Table 6.2).

6.2.4   Theoretical F(τ) vs. τ curve

In general, the recoil velocity at an instant t is given by $\beta(t)$. That will differ from that of $\beta(0)$ (at time t = 0) due to scattering of the recoil nuclei as a consequence of losing energy in the target medium. So, one have to include these changes in the direction of motion in the definition of F(τ). The instantaneous angle of $\beta(t)$ to the beam direction axis (z-axis, say) is $\phi(t)$, such that $\beta_z(t) = \beta(t)cos\phi(t)$, and $\beta_z(0) \equiv \beta(0)$. As, F($\tau$) is an attenuation coefficient, so that its value lies between 0 and 1. One can determine the lifetime of the γ-emitting level if $F(\tau)$ differs
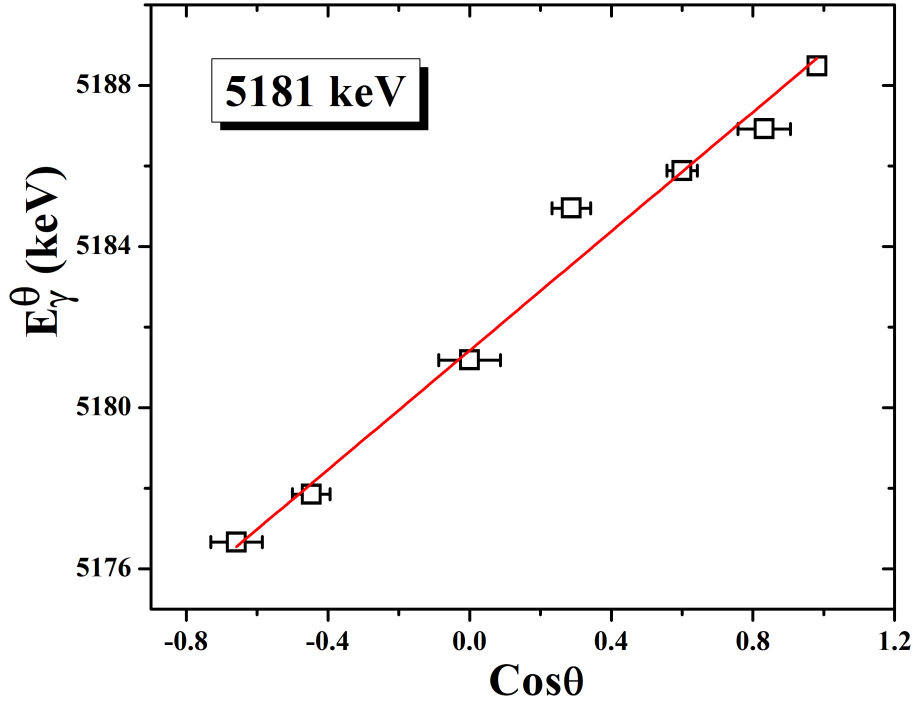
Figure 6.4: *Doppler shifted γ-ray energy (E_γ^θ) of 5181 keV γ-line plotted against cosθ, where θ is the detection angle. The solid red line corresponds to fit according to Eq. 6.3.*

from 0 and 1. Otherwise, a limiting value can be obtained for the mean lifetime.

The velocity attenuation factor F(τ) can be expressed as,

$$F(\tau) = \frac{1}{v_0\tau} \int_0^\infty \overline{v(t)cos\phi}\, e^{-t/\tau} dt \qquad (6.6)$$

where, τ is the mean lifetime of the excited states, $v(t)$ is the velocity of the recoil nuclei at time t, ϕ is the scattering angle, and $\overline{v(t)cos\phi}$ is the time dependent averaged projection of the recoil velocity distribution. The z-component of ion velocity is changing with time as functions of the characteristic slowing down time of the ions due to electronic processes, the initial velocity of the ions $v(0)$, the electronic and the nuclear stopping and scattering parameters. The stopping powers have been taken from SRIM 2013 software [53] in the present calculations. As discussed in Ref. [64], the nitrogen atoms take the interstitial positions rather than the substitutional positions inside the Ta lattice, so that we have taken the target density as of pure Ta for the
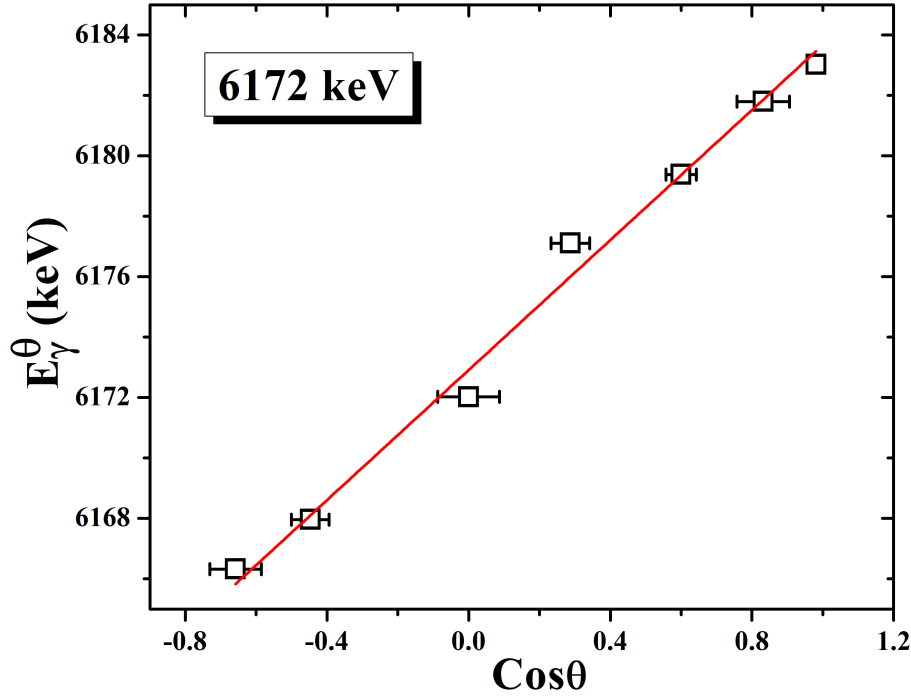
Figure 6.5: *Doppler shifted γ-ray energy (E_γ^θ) of 6172 keV γ-line plotted against cosθ, where θ is the detection angle. The solid red line corresponds to fit according to Eq. 6.3.*

calculation.

To calculate the time dependent averaged projection of the recoil velocity distribution, *i.e.*, $\overline{v(t)cos\phi}$, the collision details of large number of ^{15}O recoiling nuclei have been calculated using TRIM software [53]. The recoil velocity distribution, $\overline{v(t)cos\phi}$ has been plotted as a function of recoiling time inside the Ta backing. Next, the recoil velocity distribution has been fitted with a sixth order polynomial function. The plot is shown in Fig. 6.7. After that, the Eq. 6.6 has been solved by replacing the $\overline{v(t)cos\phi}$ with the fitted polynomial function. The numerical integration is performed with the help of Mathematica [68] computation program. The theoretical F(τ) values have been calculated for various values of τ.

- We have already calculated the experimental F(τ) values for the three secondary γ-rays. Now, for convenience of extracting corresponding τ value, F(τ) values have been plotted as an independent variable in Fig. 6.8. The curve is fitted with a fourth order polynomial
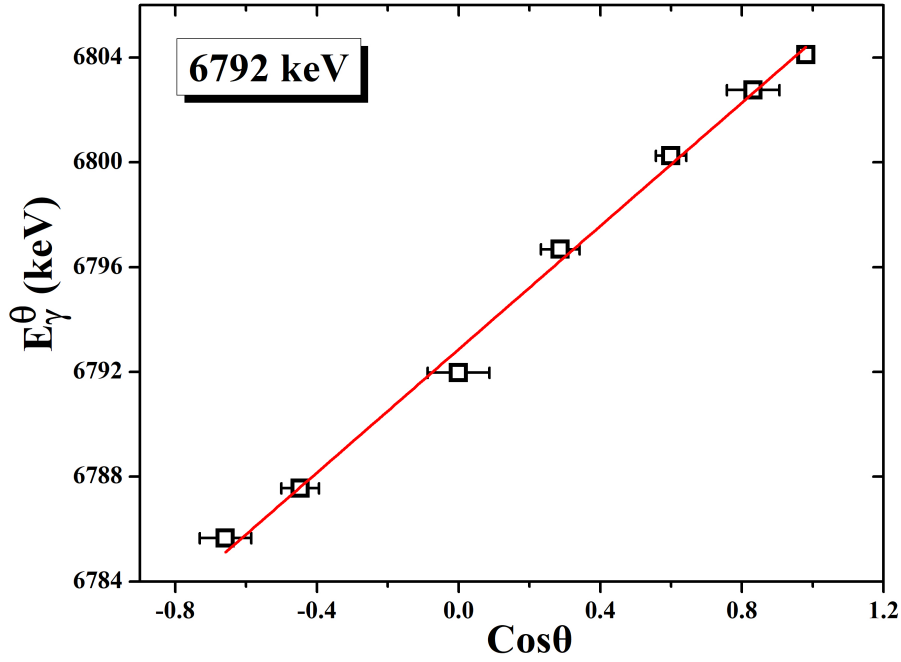
Figure 6.6: *Doppler shifted γ-ray energy (E_γ^θ) of 6792 keV γ-line plotted against $\cos\theta$, where θ is the detection angle. The solid red line corresponds to fit according to Eq. 6.3.*

function with 95% confidence level (C.L.) that expresses τ as a function of F(τ). At first, the mean lifetime value of 5181 keV γ-ray has been determined from the F(τ) vs. τ fitted curve with the corresponding experimental F(τ) value. But, in case of 6172 keV and 6792 keV γ-rays, the experimental F(τ) values are very close to 1. So, we can set only the upper limits of the mean lifetimes for the 6172 keV and 6792 keV levels of ^{15}O. The experimental F(τ) and τ values have been given in Table 6.2 with the previous literature values for comparison. The errors in the lifetime values are due to the uncertainties in the stopping power value taken from SRIM 2013 software [53], angle measurement and target stoichiometry, *etc.*
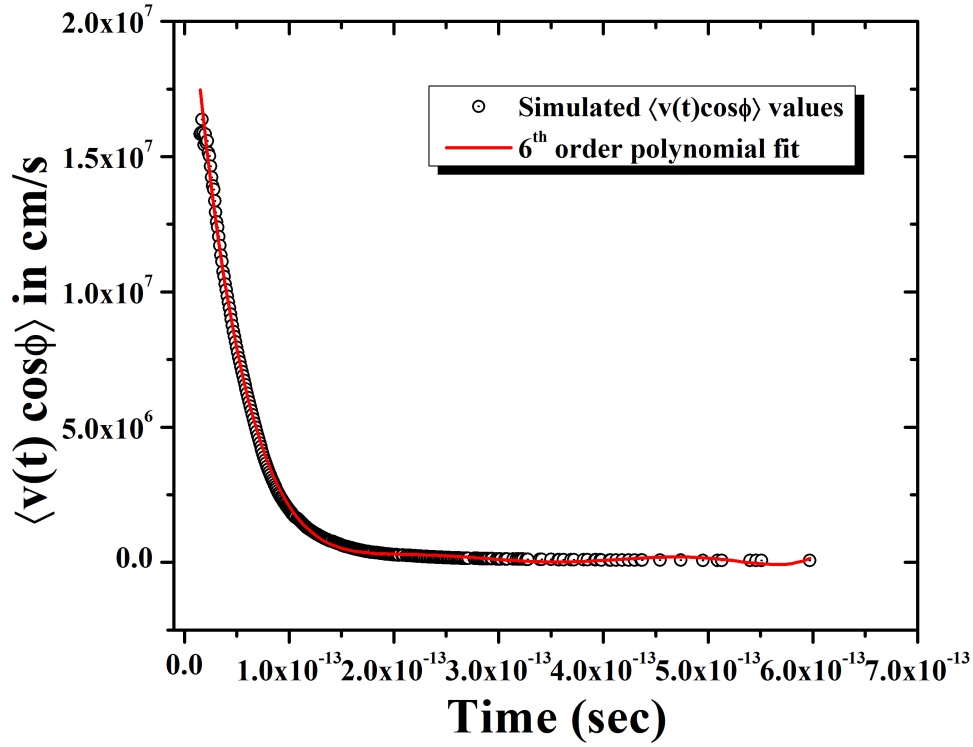
Figure 6.7: *The time dependent averaged projection of the recoil velocity distribution of ^{15}O nuclei as a function of characteristic slowing down time in the target backing medium (Ta). The red solid line shows the sixth order polynomial fit to the simulated velocity distribution data points.*

6.3   Summary and discussions

The $^{14}N(p,\gamma)^{15}O$ resonance reaction at E_p^{lab}= 278 keV has been utilized to populate few astrophysically important states of ^{15}O. An implanted target has been used for the present experiment.

The proton energy was varied from 278 keV to 312 keV to scan the implanted target. The strength of the resonance has been evaluated using thick target approximation as, $\Delta E >> \Gamma$ (using Eq. 6.2). The effective stopping power (ϵ_r) has been calculated using the SRIM 2013 software [53] considering the target density as of pure Ta. The obtained value of the resonance strength is 12.8 (9) meV, which is compared with the previous literature values in Table 6.1. The present value is in good agreement with the previous values. The weighted average value of the resonance strength ($\omega\gamma_{average}$) is 12.7 (2) meV.

The lifetime values of the secondary γ-rays 5181 keV, 6172 keV and 6792 keV have been
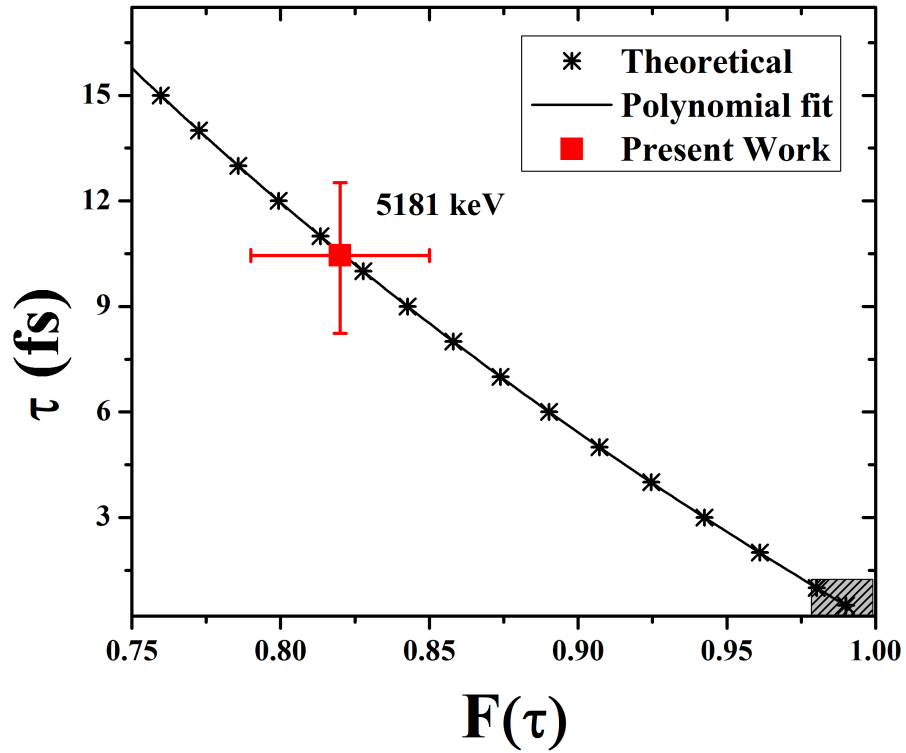
Figure 6.8: *The solid black line corresponds to F(τ) vs. τ curve according to Eq. 6.6. The theoretical data points have been obtained from Eq. 6.6 with the help of TRIM software [53]. The grey color shaded area corresponds to the allowed region for the 6172 keV and 6792 keV γ- rays for the present work. The red square corresponds to the 5181 keV γ- ray. The errors associated with the F(τ) and τ values for the 5181 keV γ-ray has also been shown in the figure.*

Table 6.2: *Experimental F(τ) and lifetime values obtained in the present work and their comparison with previous results.*

E_x (keV)	$F(\tau)$	Lifetime (τ) in fs				
		Present	Ref. [25]	Ref. [26]	Ref. [63]	Ref. [27]
5181	0.82±0.03	$10.45^{+2.07}_{-2.21}$	$9.67^{+1.34}_{-1.24}$	8.40±1.00	8.20±1.00	–
6172	1.00±0.03	<1.22	$2.10^{+1.33}_{-1.32}$	<0.77	≤2.5	<2.5
6792	0.99±0.02	<1.18	$1.60^{+0.75}_{-0.72}$	<0.77	≤28	<1.8

determined using DSAM technique. The centroid shift method has been adopted here to obtain the lifetimes of the states. We have used the target density of pure Ta to calculate the velocity attenuation profile. In the present thesis work, we do not get finite values of lifetimes for the 6172 and 6792 keV states as the F(τ) values approached to value of 1. The lifetime of the sub-threshold resonance state, *i.e.*, 6792 keV has been found to be $\tau < 1.18$ fs. So, the lower limit on the level width, Γ is > 0.56 eV. The measurement by Galinski *et al.* [27] gave the upper limit of the lifetime for 6792 keV state as $\tau < 1.84$ fs. So, the present measurement further constrained the lifetime value of the sub-threshold 6792 keV state. The obtained upper limit of the lifetime of the 6172 keV state is $\tau < 1.22$ fs. In case of 5181 keV state, we got a finite lifetime value of $10.45^{+2.07}_{-2.21}$ fs, which is in good agreement with the previous measurements [25, 26].

Chapter 7

Theoretical calculations

The reactions of interest in nuclear astrophysics mostly have very small cross-sections over the Gamow energy range. Due to this reason, these kinds of measurements have large uncertainty. However, the reaction rates depend critically on the nuclear properties of these nuclei which are produced in such astrophysical reactions. So, we need more direct and indirect measurements as well as theoretical calculations to reduce the errors or uncertainties in the nuclear physics inputs like reduced γ-ray transition strengths, level lifetimes, branchings, spectroscopic factors and level widths, *etc.*, in the stellar model calculations. Here, we have used the WSPOT code [9] to determine the energy width of the resonance state utilizing the partial wave analysis technique. The strengths of resonances and their widths are directly related to the spectroscopic factors of the states. Shell Model calculations have been performed long back to study the structural properties of some of these resonant states in light mass nuclei. Unfortunately, there are a very few microscopic large basis theoretical calculations in previous years even for the sd shell nuclei [69]. So, here, we have performed Large Basis Shell Model calculations of low lying energy levels, level lifetimes, proton spectroscopic factors of ^{15}O nucleus up to the resonance state at

7556 keV. The results of the calculation have been compared with the existing experimental data to provide better estimates of the widths and spectroscopic strengths of these states [70].

7.1 Partial wave analysis

One of the important parameters of resonance reaction is the width of the unbound state. In the present work, the width of the 7556 keV resonant state has been determined theoretically. The partial wave analysis technique is well-established for studying nuclear radiative capture resonances. This analysis is useful to search for new resonances and to predict their quantum numbers (nlj). It is also useful to estimate the spectroscopic factor of the resonance state.

7.1.1 The WSPOT code

The code WSPOT [9] has been utilized for the partial wave analysis. This program utilizes Woods-Saxon potential as the phenomenological one body potential. It gives well accepted results for the properties of bound state and continuum single particle wavefunctions. The parameters of the potential have been chosen to have a best fit of nuclear single particle energies and nuclear radii. This potential is composed of the sum of a spin independent central potential, a spin orbit potential, and the Coulomb potential. Thus the code gives single particle energies and single particle radial wavefunctions for the bound states of Woods-Saxon potential with quantum numbers (nlj). The nucleon scattering cross-sections for given l and j values, also have been calculated using the code. The set of parameters used in the present calculation are V_o(central part) = - 53 MeV, V_1(isospin dependent part) = - 30 MeV and V_{so} = 22 MeV for the potential strengths. The radii parameters are r_o(radius parameter-central) = r_{so}(radius parameter-spin orbit) = 1.25 fm and a_o(diffuseness-central) = a_{so}(diffuseness-spin orbit) = 0.65 fm for diffuseness. The radius for the Coulomb term is smaller with r_c = 1.20 fm.

7.1.2 Cross-section and phase shift

When an incident particle is captured by a target nuclei, it will form a metastable bound state which subsequently decays by emission of γ or by release of a particle. For a given (l, j) value the program calculates the phase shift $\delta(E)$ or phase difference between the incoming and outgoing wave functions. The phase difference or the shift in phase is basically dependent on the energy (E) of the incident particle. The program also calculates the cross-section ($\sigma(E)$) as a function of energy. The scattering cross-section is expressed as,

$$\sigma(E) = \frac{4\pi}{k^2} \sum_{l=0}^{l_{max}} (2l + 1) sin^2 \delta_l \tag{7.1}$$

where, k = $2\pi/\lambda$, λ is the wavelength of the incoming wave, δ_l is the phase shift of the lth partial wave.

7.1.3 Resonance energy and level width

By varying the energy of the incoming particle the relative phase of the inner and outer wavefunctions have been changed. The energy E_0 where the amplitude of inside and outside wavefunctions match, cross-section has maximum value. This energy E_0 is known as the resonance energy. Only one partial wave 'l' is necessary to have the occurrence of a resonance state corresponding to the energy E_0. At resonance energy (E_0), the phase shift is equal to, $\delta_l(E) = \pi/2$. The width of the resonance (Γ) is determined from the energy (E), where cross-section reduces to half of a central value, *i.e.*, (E - E_0) = $\pm$ $\Gamma/2$ [71].

7.2 Results

Theoretically, the one proton $1/2_2^+$ resonant state at 7556 keV is populated through a pure $l = 0$, *i.e.*, s wave capture. By varying the energy of the incoming proton, the width of the resonance is obtained. The results of the given cross-section and phase shift as a function of energy have been plotted in Fig. 7.1. From the theoretical calculation, we get the width of the unbound state of 1.2 (12) keV which is close to the experimental width of 0.99(10) keV [67]. Now, the ratio of

Table 7.1: *Results of the WSPOT calculations for the 7556 keV resonance state of ^{15}O.*

E_x	E_R	Width (Γ)		Spectroscopic factor	Single particle
(keV)	(keV)	$\Gamma^{Expt.}$ (keV)	$\Gamma^{Theo.}$ (keV)	($\Gamma^{Expt.}/\Gamma^{Theo.}$)	orbital (nlj)
7556	259	0.99(10)	1.2 (12)	0.82 (9)	$2s_{1/2}$
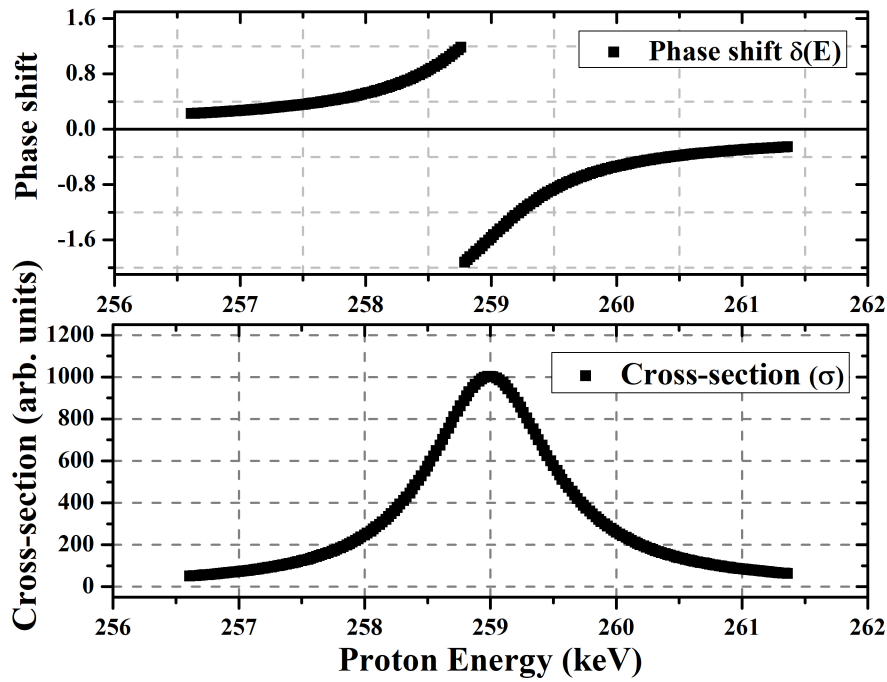
Figure 7.1: *Results of the WSPOT [9] calculations of the $E^r_{c.m.} = 259$ keV resonance of $^{14}N(p,\gamma)^{15}O$ reaction. The top plot corresponds to the phase shift ($\delta(E)$) as a function of incident proton energy (in keV) which is equal to $\pi/2$ at resonance energy. The bottom plot corresponds to the cross-section variation as a function of proton energy. The experimental resonance energy is nicely reproduced in WSPOT calculations. The cross-section takes the maximum value at resonance energy which has been clearly seen in the bottom figure.*

experiment over theory provides a measure of the spectroscopic factor, S = 0.82(9). This value agrees well with the reported experimental value of 0.82(18) [28]. However, it deviates by a factor of ≈ 0.6 from the value reported by Ref. [16] . The results have been given in Table 7.1.

7.3   The Shell model

Atomic theory based on the shell model provides remarkable clarification of the complicated details of atomic structure. Now, to resolve the problem of nuclear structure, a similar kind of shell model theory has been adopted by the nuclear physicists. In the atomic shell model, the potential is supplied by the Coulomb field of nucleus, the subshells or orbits are established by an external agent [2] here. One can solve the Schrödinger equation for this potential and then calculate the energies of the subshells where electrons can then be placed. The shells have been filled up with electrons in order of increasing energy obeying the Pauli Exclusion Principle. Thus one can have an inert core of filled shells and some number of valence electrons that primarily determine the atomic properties. In case of the nucleus, there is no such external agent to create the potential, the nucleons move in a potential that they create by themselves. Another important fact is that, unlike to Coulomb potential, the nuclear interaction is very different and, moreover, the nature of the nucleon-nucleon interaction is not precisely known. There are two kinds of elementary particles, *i.e.*, protons and neutrons as opposed to the atomic case (*i.e.*, only electrons) and there is no heavy centre of force for the nucleons. Despite of these complicated facts, the nuclear shell model has been highly successful in describing many properties of nuclei [1].

The basic assumption of nuclear shell model is that the interaction of each nucleon with all the other protons and neutrons in the nucleus is well approximated by some average potential $V(r_i)$. A single nucleon moves independently in this potential and can be described by a single particle state of discrete energy and constant angular momentum.

The Hamiltonian (H) of A nucleon system is written as a sum of one body kinetic energy part and a two body potential energy term,

$$H = \sum_{i=1}^{A} T_i + \frac{1}{2} \sum_{i,j=1}^{A} V_{i,j} = \sum_{i=1}^{A} -\frac{\hbar^2}{2m_i} \nabla_i^2 + \frac{1}{2} \sum_{i,j=1}^{A} V_{i,j} \tag{7.2}$$

The Hamiltonian can be rewritten after adding and subtracting an one body term $V(r_i)$ as,

$$H = \sum_{i=1}^{A} [T_i + V(r_i)] + \left(\frac{1}{2} \sum_{i,j=1}^{A} V_{i,j} - \sum_{i=1}^{A} V(r_i) \right) = H_0 + H_{res} \qquad (7.3)$$

where, H_0 is the one body part of the Hamiltonian which describes the motion of A nucleons in the mean field $V(r_i)$ and H_{res} is the residual interaction which is basically two body part of the Hamiltonian. The one body part $V(r_i)$ in H_0 has to be chosen in such a way that the residual interaction part H_{res} becomes small enough to be treated as a non-relativistic perturbation.

Now, the initial step in developing the shell model is the choice of the correct form of the average potential V(r). At first, two form of potentials have been chosen – the infinite square well and harmonic oscillator to solve the three dimensional Schrödinger equation for the motion of nucleons. The solutions of the Schrödinger equation for such potentials are bound single particle states that are characterized by the values of the radial quantum number (n), orbital angular momentum quantum number (l) , and total angular momentum quantum number (j) respectively. These two forms of potentials are able to reproduce the magic numbers like, 2, 8 and 20, but the higher levels do not correspond at all to the observed magic numbers. The single particle energies of a harmonic oscillator potential as a function of the oscillator quantum number, N = $2(n$ - $1) + l$, corresponding to the total number of oscillator quanta excited, have been shown in Fig. 7.2. Now, to improve the model into a more realistic and intermediate to the previously used potentials, have been used to solve the Schrödinger equation. This potential is known as Woods-Saxon potential which is more realistic but mathematically less tractable. It is defined by,

$$V(r) = -\frac{V_0}{[1 + exp(r - R)/a]} \qquad (7.4)$$

where, V_0 denotes the potential depth, R $\approx$ 1.2 A$^{1/3}$ fm is the potential radius, and a is the diffuseness parameter, respectively. In case of harmonic oscillator potential, each single particle state of given N consists in general of states with different values of l. These single particle states have the same energies and are thus called degenerate. The degeneracy has been lifted for the more realistic Woods–Saxon potential, *i.e.*, states with different values of l possess different energies. But the calculations again failed to reproduce the higher magic numbers (only 2, 8 and

20 values are reproduced in case of Woods-Saxon potential).

In 1949, Goeppert-Mayer [72] and Haxel, Jensen and Suess [73] came with their idea of adding a strong spin-orbit coupling term with the Woods-Saxon potetial that could account for the observed magic numbers. The spin-orbit potential has the form, $V_{so}(r)\ \vec{l}.\vec{s}$, where $\vec{l}$ is the orbital angular momentum and $\vec{s}$ is the intrinsic spin angular momentum of the nucleon. This interaction splits up the degeneracy in $j = l \pm 1/2$ levels. After adding the spin-orbit coupling term to the Woods-Saxon potential all the magic numbers 2, 8, 20, 28, 50, 82 and 126 have been reproduced successfully (see Fig. 7.2). In the extreme single particle shell model, the properties of the nucleus have been determined by the outermost valence nucleon only. The properties of the ground state and low energy excited states have been correctly predicted by this extreme single particle model. This model has very limited applicability and can be only expected to work in immediate vicinity of the major shell closures in nuclei and one can observe a breakdown of the nuclear extreme shell model power to predict the structure of the excited states. The reason behind the discrepancies between the experimental data and shell model predictions is basically due to the negligence of the residual interaction term. So, to explore more nuclear properties, one needs to include the residual interaction term in the total Hamiltonian.

7.3.1   Effective residual interaction : Two body matrix elements (TBMEs)

The residual interaction is the key to understand the nuclear structure beyond the extreme single particle shell model. The interaction results in correlations in the nuclear wave function beyond the mean field. There are different kinds of effective interactions which can be categorized basically in two groups. The first group deals with the realistic potentials which are determined by fitting the experimental two nucleon data. But these potentials should not be used as such in nuclear structure calculations as the scattering behaviour of the free two nucleons is quite different from that of the two nucleons inside a nucleus. One typical example of such kind of potential is Hamada-Johnston potential [74]. The second one is of semi-phenomenological type. Here, the effective interaction is described by a small number of parameters to be determined
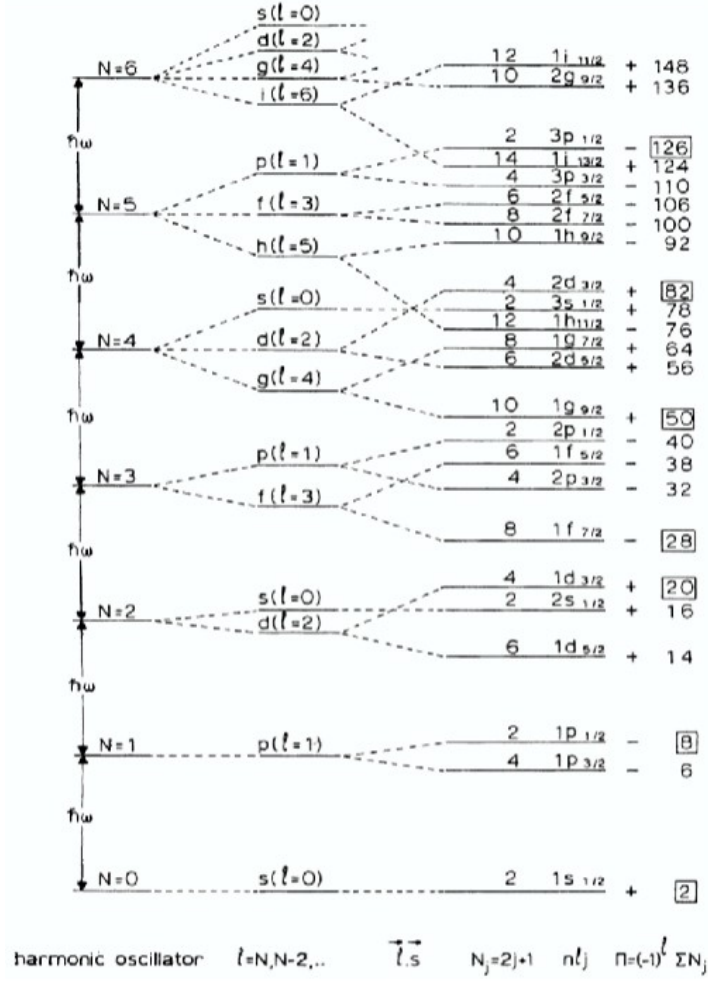
Figure 7.2: *Approximate sequence of single particle states for identical nucleons (protons or neutrons). The magic numbers are indicated by open rectangular boxes. The level pattern basically explains the qualitative features only. From the figure, it is clear that the magic numbers are reproduced after using the Woods-Saxon potential with spin orbit coupling. The picture is taken from Ref. [1].*

by fitting a large number of experimental results like nuclear level energies, electromagnetic moments, transition rates, *etc*. The parameter values are sensitive to the single particle levels included in the calculation and also to the way in which core contributions are treated. This effective interaction also depends on the extent of the configurations considered in the calculation. This kind of empirical interactions are like Brussaard-Glaudemans and Cohen-Kurath interactions for the p shell, Wildenthal-Brown for the sd shell and Brown-Ritcher for the fp shells. The two body matrix elements (TBMEs) are deduced using the empirical effective interactions for different configurations of the nuclei. The choice of the residual interaction depends on the

choice of active orbitals.

7.3.2   Configuration mixing

In the shell model the particle wave function is a pure (nlj) configuration, assuming that the inter nucleon (residual) interaction is weak and not disturbing the states predicted by the effective single particle Hamiltonian. However, in the presence of strong inter nucleon interaction, the shell model wave function is basically a superposition of two or more configurations whose energies are close to one another. This is basically known as configuration mixing. If the basis state is denoted by $|\phi_k^{(0)}>$ (k = 1,2,..., n), the total wavefunction can be expanded as,

$$|\phi_p> = \sum_{k=1}^{n} a_{kp}|\phi_k^{(0)}> \tag{7.5}$$

where, a_{kp} have to be determined by solving the Schrödinger equation,

$$H|\phi_p> = E_p|\phi_p>, \tag{7.6}$$

$$(H_0 + H_{res})\sum_{k=1}^{n} a_{kp}|\phi_k^{(0)}> = E_p \sum_{k=1}^{n} a_{kp}|\phi_k^{(0)}> \tag{7.7}$$

The eigenvalue equation may be written in matrix equation also (see [75]) like,

$$[H][A] = [E][A] \tag{7.8}$$

After diagonalising the Hamiltonian, one get n energy eigenvalues. The complexity increses with the increase in number of basis states, *i.e.*, with the n value. There are number of algorithms to diagonalise the [H] matrix. In large basis shell model calculations, the Lanczos algorithm have been used to diagonalise the matrix. Whenever, the non-diagonal matrix elements are of the order of the unperturbed energy differences, large configuration mixing will take place and the final energy eigenvalues can be very different from the unperturbed spectrum. If, the non-diagonal matrix elements are small then the energy shifts will be small and even perturbation theory may be applied [75].

7.3.3   Predictions from nuclear shell model

The properties of the closed shell nuclei as well as the properties of nuclei with partly filled shells are well predicted by the nuclear shell model. The nuclear properties depend on the configuration of the nucleons. Different nuclear properties like excitation energies of nuclear levels, total angular momentum (j) and parity of the ground state as well as the excited states, transition probabilities, level lifetimes, branching and mixing ratios, and spectroscopic factors, have been determined from the nuclear shell model.

7.3.3.1   Level energy, angular momentum and parity

The binding energies or level energies of the nucleus has been determined by the single particle energies due to the independent motion of the nucleons in an average potential and by the mutual interaction of the valence nucleons. Usually, the ground state energy is rescaled to a value of zero and the energies of the excited states have been changed accordingly. The total angular momentum (j) of the nucleus or the nuclear spin has been obtained by coupling the angular momenta of the independent single particle states according to the quantum mechanical rules for vector addition. The total parity of the nucleus is calculated by taking the product of the parities for all nucleons.

7.3.3.2   Transition probability

The interaction of the electromagnetic field with the nucleons might be expressed in terms of a sum of electric and magnetic operators with tensor rank (*) λ,

$$\mathcal{O} = \sum_{\lambda,\mu} [\mathcal{O}(E\lambda)_\mu + \mathcal{O}(M\lambda)_\mu] \tag{7.9}$$

The electromagnetic transition rate or transition probability ($W_{M_i,M_f,\mu}$) for the transition between specific M states (*) is written as [76],

$$W_{M_i,M_f,\mu} = \left(\frac{8\pi(\lambda+1)}{\lambda[(2\lambda+1)!!]^2} \right) \left(\frac{k^{2\lambda+1}}{\hbar} \right) |< J_f M_f | \mathcal{O}(\lambda)_\mu | J_i M_i >|^2 \tag{7.10}$$

where, k is the wave number for the electromagnetic transition of energy E_γ.

The elctric transition operator has the form,

$$O(E\lambda) = r^\lambda Y_\mu^\lambda(\hat{r})e_{t_z}e \tag{7.11}$$

where, Y_μ^λ are the spherical harmonics, e_{t_z} are the electric charges for the proton and neutron in units of e. For the free nucleon charge one would take $e_p = 1$ and $e_n = 0$, for the proton and neutron, respectively.

The magnetic transition operator has a form like,

$$O(M\lambda) = \left[\vec{l}\frac{2g_{t_z}^l}{(\lambda+1)} + \vec{s}g_{t_z}^s \right] \vec{\nabla} \left[r^\lambda Y_\lambda^\mu(\hat{r}) \right] \mu_N \tag{7.12}$$

where, μ_N is the nuclear magneton, $\mu_N = \frac{e\hbar}{2m_p c} = 0.0105$ efm [76] with m_p is the proton mass. The g-factors $g_{t_z}^l$ and $g_{t_z}^s$ are the orbital and spin g-factors for the proton and neutron, respectively. In case of free nucleons the values of the g-factors are $g_l^p = 1$, $g_l^n = 0$, $g_s^p = 5.586$ and $g_s^n = -3.826$ respectively.

Now, to obtain the total rate for a specific set of states and a given operator, one have to average over the M_i states and to sum over M_f and μ,

$$W_{i,f,\lambda} = \left(\frac{8\pi(\lambda+1)}{\lambda[(2\lambda+1)!!]^2} \right) \left(\frac{k^{2\lambda+1}}{\hbar} \right) \frac{|< J_f|\mathcal{O}(\lambda)_\mu|J_i >|^2}{(2J_i+1)} \tag{7.13}$$

The last factor in Eq. 7.13 is referred to as reduced transition probability (B) which is defined by,

$$B(i \rightarrow f) = \frac{|< J_f|\mathcal{O}(\lambda)_\mu|J_i >|^2}{(2J_i+1)} \tag{7.14}$$

7.3.3.3 Level lifetimes

The level lifetimes (τ) are directly related to the reduced transition probabilities (B). The theoretical level lifetimes of nucleus have been calculated by using theoretical reduced transition probabilities (B) and experimental γ-ray energy values and branching ratios, wherever needed. The relation between reduced transition probability (B) and level lifetimes (τ) for most common type of transitions are given below, for electric transitions [76],

$$B(E1) = \frac{0.629}{E_\gamma^3 \tau}e^2 fm^2 MeV^3 fs \tag{7.15}$$

$$B(E2) = \frac{816}{E_\gamma^5 \tau} e^2 fm^4 MeV^5 ps \qquad (7.16)$$

$$B(E3) = \frac{1760}{E_\gamma^7 \tau} e^2 fm^6 MeV^7 \mu s \qquad (7.17)$$

$$B(E4) = \frac{5882}{E_\gamma^9 \tau} e^2 fm^8 MeV^9 s \qquad (7.18)$$

and for magnetic transitions [76],

$$B(M1) = \frac{56.8}{E_\gamma^3 \tau} \mu_N^2 MeV^3 fs \qquad (7.19)$$

$$B(M2) = \frac{74.1}{E_\gamma^5 \tau} \mu_N^2 fm^2 MeV^5 ns \qquad (7.20)$$

$$B(M3) = \frac{0.1585}{E_\gamma^7 \tau} \mu_N^2 fm^4 MeV^7 s \qquad (7.21)$$

$$B(M4) = \frac{0.533 \times 10^6}{E_\gamma^9 \tau} \mu_N^2 fm^6 MeV^9 s \qquad (7.22)$$

In case of mixed transitions, the mixing ratio has been incorporated properly in order to determine the correct level lifetime.

7.3.3.4   Spectroscopic factor

Spectroscopic factor is defined as the square of the overlap integral of the initial and final channel wavefunctions. It is basically connected with the removal or addition of nucleon from a specific initial state to a specific final state and directly related to the matrix elements of the creation and destruction operators [76]. The spectroscopic factor (S) is defined in terms for the reduced matrix elements of the creation operator (a^+) by,

$$S = \frac{| < \phi^A \omega J || a_k^+ || \phi^{A-1} \omega' J' > |^2}{2J + 1} \qquad (7.23)$$

where, the (2J + 1) factor is by convention associated with the heavier mass A, ω corresponds to all the quantum numbers associated with a particular level and S implicitly depends upon all the quantities in the expression. Whenever the wavefunction is restricted to only one orbital k with the angular momentum j, the spectroscopic factor is then related to the coefficients of fractional parentage by the equation,

$$S = n| < j^n \omega J |\} j^{n-1} \omega' J' > |^2 \qquad (7.24)$$

The cross-section for reactions involving the addition of a particle to nucleus A is derived from the full matrix element of a^+ summed over m and M_f and averaged over M_i like,

$$\sigma^+ \sim \frac{1}{2J_i + 1} \sum_{M_i, M_f, m} | < \phi_f^{A+1} \omega_f J_f M_f | a_{k,m}^+ | \phi_i^A \omega_i J_i M_i > |^2 \qquad (7.25)$$

$$= \frac{1}{2J_i + 1} | < \phi_f^{A+1} \omega_f J_f || a_k^+ || \phi_i^A \omega_i J_i > |^2 = \frac{2J_f + 1}{2J_i + 1} S \qquad (7.26)$$

where, S is the spectroscopic factor associated with the removal of a particle from A + 1 to A. So, the cross-section for the addition of a particle is written as,

$$\sigma^+ = \frac{2J_f + 1}{2J_i + 1} S \sigma_{sp} \qquad (7.27)$$

where, σ_{sp} is the single particle cross-section assuming S = 1.

Similar to addition, the relation between the spectroscopic fator and cross-section for removing a particle (proton or neutron) is given as,

$$\sigma^- = S \sigma_{sp} \qquad (7.28)$$

Here, the J factors take into account the different M states averaging for the two type of reactions (*i.e.*, removal or addition of a particle).

The particle addition sum rule for spectroscopic factors is obtained by summing over all states in the (A - 1) nucleus (denoted by f^-),

$$\sum_{f^-} S_{i,j,k} = < n_k >_i \qquad [A \to (A - 1)] \qquad (7.29)$$

and in case of particle addition the expression is obtained by summing over all states in the (A + 1) nucleus (denoted by f^+),

$$\sum_{f^+} \frac{2J_f + 1}{2J_i + 1} S_{i,j,k} = (2j + 1) - < n_k >_i \qquad [A \to (A + 1)] \qquad (7.30)$$

where, $<n_k>_i$ is the average occupation of protons or neutrons in orbit k in the initial state i with maximum possible value of $(2j + 1)$. The total sum rule is given as,

$$\sum_{f^-} S_{i,j,k} + \sum_{f^+} \frac{2J_f + 1}{2J_i + 1} S_{i,j,k} = (2j + 1) \qquad (7.31)$$

7.4   The NuShellX code

NuShellX is basically a set of computer codes written by Bill Rae [77]. The codes have been used to obtain exact energies, eigenvectors and spectroscopic overlaps for low lying states of nuclei. Here, one can perform the shell model Hamiltonian matrix calculations with very large basis dimensions. It uses a J coupled proton-neutron (p-n) basis for the calculations. The code handles J scheme matrix dimensions of up to the order of 100 million [8]. NuShellX@MSU is a set of wrapper codes which is written by Alex Brown [78]. It uses data files for model spaces and Hamiltonians to generate input for NuShellX. The codes also transformed the NuShellX output into figures and tables for energy levels, gamma decay and beta decay, *etc*. The details formalism of the NuShellX code has been given in [8].

7.5   Large basis shell model (LBSM) calculations

Here, the large basis shell model (LBSM) calculation using the NuShellX code has been performed for the ^{15}O nuclei which is populated through ^{14}N(p,γ) reaction. The rate of the ^{14}N(p,γ)^{15}O resonance capture reaction depends on the structural properties of the low lying states in ^{15}O. According to Ref. [79], the proton spectroscopic factors for states in ^{15}O populated by ^{14}N(^{3}He,d)^{15}O reaction and neutron spectroscopic factors for ^{15}N populated by ^{14}N(d,p)^{15}N reaction deviate by factors of 0.65 and 0.63 for $l = 0$ and $l = 2$ components, respectively. Fortune *et al.* [79] addressed the problem and found that the actual $l = 0$ spectroscopic factors for two $3/2^{+}$ states are significantly smaller than those recently reported. Thus, it is essential to perform theorerical calculations within the large basis shell model to extract the absolute spectroscopic strengths of the states of ^{15}O.

Now, to calculate the wavefunction and energy spectra, the ZBM (Zuker-Buck-McGroy) model space has been used [8]. ZBM model space consists of ^{12}C core and $1p_{1/2}$, $1d_{5/2}$ and $2s_{1/2}$ as the valence orbitals. The available interactions in this ZBM model space in the NuShellX code are – a) ZBMI [80], b) ZBMII [80], c) REWIL [81], and d) ZWM [82], respectively.

These available interactions have been used for the calculations. The energy spectra have been calculated till 20 MeV using full valence space, without any subshell restrictions. The theoretical energy levels up to 8 MeV have been compared with the experimental data in Fig. 7.3. In Fig. 7.3, the results using the interactions ZBMII, ZWM, REWIL have been shown in comparison with experimental energy levels. In case of ZBMI interaction the ground state spin of ^{15}O has not been reproduced, so the results from the ZBMI interaction have been excluded from the Fig. 7.3.

Figure 7.3: *Comparison of experimental energy levels with theoretical calculations of ^{15}O.*

The reduced transition probabilities for E2 and E1 transitions have been calculated with effective charges e_p=1.35e and e_n=0.35e, respectively. In the case of M1 and M2 transitions, standard values of intrinsic magnetic moments have been used. The level lifetimes of the ^{15}O nucleus have been calculated by using theoretical reduced transition probabilities and experimental γ-ray energy values and branching ratios, wherever needed. Another critical parameter for astrophysical model calculations is the spectroscopic factor. As the astrophysical reaction rate of ^{14}N(p,γ)^{15}O reaction depends on the proton spectroscopic factors of the ground

state (g.s.) wavefunction for initial nucleus (^{14}N) and also for final nucleus (^{15}O) with the same interaction. So, after calculating the wavefunctions for both the nuclei, the overlap integral for ^{14}N g.s. with all the states of ^{15}O have been calculated.

7.5.1   Results

All the positive and positive and negative parity states are reproduced reasonably well except the $3/2^-_1$ state, *i.e.*, 6172 keV state which is overpredicted (see Table 7.2). As the results using the REWIL interaction agree better with the experiment compared to other interactions, only the results from this interaction have been given in Table 7.2.

Table 7.2:   *Comparison of experimental level energies and lifetimes of ^{15}O with the shell model predictions.*

Expt.			Theo.	
Energy	Lifetime (τ)		Energy	τ
(keV)	Present	Prev.[67]	(keV)	
5181	$10.45^{+2.07}_{-2.21}$ fs	5.7(7) fs	5192	0.82 fs
5240	–	2.25 (21) ps	5276	1.2 ps
6172	<1.22 fs	<1.74 fs	8920	1.5 fs
6792	<1.18 fs	<20 fs	7318	0.07 fs
6859	–	11.1(17) ps	7631	30.46 ps
7276	–	0.49(11) ps	7199	0.42 ps

The level lifetime values are compared with the experimental data from the present and previous work [67]. Theory predicts the lifetime values quite well in most of the cases. The proton spectroscopic factors of ^{15}O have been calculated theoretically and compared with experimental values from the literature [16, 28]. The comparison between theory and experiment is given in Table 7.3.

In most of the cases, the calculated values are closer to the experimental data reported in Ref. [16]. However, for 6792 keV state, the calculated value disagrees with the experimental data. The absence of $1d_{3/2}$ orbit in the model space may be one of the reasons for this discrepancy. Interestingly the spectroscopic factor for 7556 keV from shell model agrees with the value

Table 7.3: *Comparison of proton spectroscopic factors of previous experimental data with the shell model predictions.*

| | | | | C^2S | |
| | | | Theo. | Expt. | |
E_x (keV)	J^π	nl_j	Present	Schröder *et al.* [16]	Bertone *et al.* [28]
0	$1/2^-$	$1p_{1/2}$	1.23	1.29 (18)	1.7(4)
5181	$1/2_1^+$	$2s_{1/2}$	0.01	0.004 (1)	0.0049(15)
5240	$5/2_1^+$	$1d_{5/2}$	0.1	0.06 (1)	0.094(20)
6172	$3/2_1^-$	$1p_{1/2}$	0.001	0.038 (16)	0.050(11)
6792	$3/2_1^+$	$2s_{1/2}$	0.96	0.49 (1)	0.51(11)
		$1d_{5/2}$	0.004	-	0.16(3)
6859	$5/2_2^+$	$1d_{5/2}$	0.74	0.37 (1)	0.61(13)
7276	$7/2_1^+$	$1d_{5/2}$	0.99	0.35 (1)	0.66(14)
7556	$1/2_2^+$	$2s_{1/2}$	0.56	≈ 0.49	0.82(18)

reported in Ref. [16] which deviate by a factor of ≈ 0.6 from that reported by Ref. [28] as well that predicted by partial wave analysis (see Table 7.1).

It has been discussed earlier that the energy of the $3/2_1^-$ state is overpredicted and the spectroscopic factor is underpredicted. To reproduce a negative parity state $3/2_1^-$, only a single negative parity orbital $1p_{1/2}$ is present in the ZBM model space. The $1p_{3/2}$ orbital is absent in the ZBM space, which may cause the discrepancy for $3/2^-$ state. Thus, another model space PSD has been considered with PSDMK interaction. The PSD model space, consists of $1p_{3/2}$, $1d_{3/2}$ as well as $1p_{1/2}$, $1d_{5/2}$ and $2s_{1/2}$ orbitals with a ^{4}He core. In this case, full space calculations were beyond the present computational capacity. Thus a suitable truncation scheme has been adopted to perform the calculations. Sub-shell restrictions – with six particles and two holes in the $1p_{3/2}$ orbital, zero occupancies in the $1d_{3/2}$ orbital and no restrictions to the other orbitals have been adopted. The ground state spin is reproduced, but the energy values are overpredicted (see Fig. 7.3). The ZBME model space ($1p_{1/2}$, $1d_{3/2}$, $1d_{5/2}$, $2s_{1/2}$) with REWILE interaction have also been used. However, the changes in the energy eigenvalues are less than 1% compared to ZBM+REWIL calculations. The inclusion of $1d_{3/2}$ orbital does not improve the results.

7.6   Summary and discussions

The partial wave analysis was used to calculate the resonance width of the 7556 keV resonant state. The calculated width of the 7556 keV state and its spectroscopic factor are in good agreement with the literature values [28]. The theoretical calculations using large basis shell model with ZBM model space and REWIL interaction reproduced the experimental data well in most of the cases. The resonance state at 7556 keV is reproduced theoretically at 7646 keV using the shell model calculation. The calculated spectroscopic factor for 7556 keV state agrees with that reported in Ref. [16]. However, it disagrees with the data from Ref. [28] and the calculated value from partial wave analysis. The lifetimes and spectroscopic factors for other observed states are also calculated and compared with present and previous data, wherever available. However, some disagreements of the theoretical results with experimental data for a few states, indicate the need of improved interactions in the lighter mass region.

Chapter 8

Estimation of background γ-radiation

8.1 Introduction

Natural γ-ray emitters contained in indoor and outdoor surrounding materials have significant contributions to the background of the γ-ray spectra. To improve the minimum detection level in the γ-ray spectrum, measurement and reduction of the background events are essential. Now, due to this reason, any γ-ray spectroscopy laboratory pays special attention to minimize the radiation background of detectors to improve the Minimum Detectable Activity (MDA) of the detection system. The MDA of the detection system is defined as [83],

$$MDA \simeq \frac{\sqrt{Background\ Counts}}{Detection\ Efficiency},$$

(8.1)

Whenever the size of the detector increases, the efficiency will increase to provide a limit in minimum detectable activity (MDA), but it is not always an economically viable solution. Bigger detectors also face the problem of increasing summing effects. They are also much efficient in detecting background radiation. So, it is necessary to optimize the parameters related to background suppression [84] to minimize the MDA.

Omnipresent background radiation is generally emitted from a variety of natural and artificial radiation sources in the Earth, and its atmosphere and from cosmic rays originated from space. The energies of γ-rays coming from natural radioactive elements are generally up to 3 MeV. The background in the γ-ray spectrum is primarily due to cosmic ray interactions within the upper atmosphere at energies above 3 MeV.

To study the rare nuclear physics processes, low background γ-ray spectroscopy is an essential tool. The meter water equivalent (often m.w.e.) is a standard unit to measure the effectiveness of shielding for cosmic ray attenuation in underground laboratories. Laboratories at the same depth of overburden can have different degrees of penetration of cosmic rays depending on their composition. The m.w.e. thus provides a convenient and consistent way of comparison of background suppression at different low background laboratories at overground and underground locations. These kind of low background γ-ray spectrometers are either operated in standard overground laboratories in buildings under a low overburden (< 1 m water equivalent (m.w.e.)), or at specialized underground laboratories with high (> 1000 m.w.e.) overburden. Even with a few meters water equivalent shielding, the soft component of cosmic rays can be shielded.

All the relevant reactions take place far below the Coulomb barrier in nuclear astrophysics. Thus the reaction cross-sections are very small. The cross-sections are typically in the nanobarn - picobarn range [85]. So, the reduction of events arising from background radiation is necessary for these kind of measurements. In case of an underground laboratory, the huge overburden shield the facility from the cosmic radiation that can interfere with these experiments. It is always advantageous to work in an underground laboratory when the energies of γ-rays of interest are higher than 3 MeV. However, if the γ-ray energies of interest are less than 3 MeV, then the underground facility does not provide any additional advantage [85]. Additional shielding arrangements are needed to reduce the γ-rays originated from natural radioactivity.

In general, the radiation shieldings are of two types – a) passive and b) active shieldings, which are used to suppress the background γ-radiation. In case of passive shielding arrangement, one generally covers the detector system with high Z elements, like lead (Pb, Z=82) with adequate thickness for the absorption of the highest energy environmental γ-ray radiation background.

Layers of gradually decreasing Z cover the inner side of the shielding. The active shielding method includes sophisticated anti-correlation techniques in data acquisition. To stop the neutrons, which may give rise to subsidiary γ-ray radiation, low Z materials like paraffin, high-density polyethylene (HDPE), and concrete shielding have been used. To optimize the shielding configuration, both the experimental technique and Monte Carlo modelling are necessary.

A low energy accelerator-based Facility for Research in Experimental Nuclear Astrophysics (FRENA) is in the process of installation at the Saha Institute of Nuclear Physics, Kolkata. The accelerator hall and beam hall in the building are shielded by a 1.2 m thick concrete wall to reduce the radiation dose outside these rooms to permissible limits. Nearly 60 cm ($\simeq$ 1.5 m.w.e.) of the concrete ceiling reduces the cosmic muons by a significant amount. The energy loss of muons in concrete is nearly 4 MeV/cm [86], so muons with the energy of 240 MeV are entirely absorbed within the concrete shielding. However, these concrete walls work not only as shields but are also sources of background γ-ray radiation originated from natural radioactivity. So, it is essential to evaluate the extent of the contribution of these walls in the indoor environment of FRENA halls, especially in the γ-ray spectrum below 3 MeV.

So, in the present work, we have measured the background γ-ray spectra at several positions of the FRENA accelerator building like accelerator hall and beam hall with a bare HPGe detector without any additional temporary shielding. Background spectra have been acquired at two other nuclear physics laboratories (Lab I and II) bounded by standard brick walls. The energy spectra at the positions mentioned above have been compared to understand the shielding effect and the contributions from the concrete walls. Additionally, some passive and active shieldings have been arranged surrounding the bare HPGe detector. The suppression induced by these shieldings has been quantified. The preliminary results have been reported in Ref. [87].

Here, we have used Monte Carlo simulation to evaluate the contribution of these concrete walls in the indoor environment of FRENA halls, especially in the γ-ray spectrum below 3 MeV. A spherical layer of concrete shielding have considered as the simulation model geometry. The radioactive elements are isotropically distributed within the concrete walls. Similar 4π-geometry irradiation has been suggested for the radiation field in the buildings constructed with concrete

walls by Tsutsumi *et al.* [88]. The effects of variations of different parameters like wall thickness, the radius of the spherical shell have been tested in the recent work. Simulations have been performed to optimize the shielding arrangements.

8.2   Sources of background radiations

A variety of natural and artificial radioactive sources emit background γ-ray radiation. The primary natural sources are cosmic rays originated from space and sources in the Earth's crust, and its atmosphere. A tiny fraction of background γ-ray radiation generated from man-made sources.

Natural deposits of uranium, potassium, and thorium are contained in the Earth's crust. The ^{238}U, ^{40}K and ^{232}Th nuclei are radioactive and release ionizing radiation. Uranium, thorium, and potassium are omnipresent, *i.e.*, these nuclei are basically found everywhere. These elements have been found in building materials. The γ-ray spectrum up to 3 MeV is mainly dominated by the radiation emitted by ^{40}K and the nuclei in the decay chains of ^{238}U and ^{232}Th, *etc.*, [89]. Natural potassium contains 0.012% of ^{40}K which decays with $T_{1/2} = 1.248(3) \times 10^9$ y [89] and emits a γ-ray of 1.460 MeV energy [89, 90]. The decay chain of daughters of ^{238}U ($T_{1/2} = 4.468(6) \times 10^9$ y) and ^{232}Th ($T_{1/2} = 1.40(1) \times 10^{10}$ y) emit a long series of γ-rays [89]. The highest energy intense γ-ray at energy 2.615 MeV, originates from the decay of ^{208}Tl, a progeny of ^{232}Th. One of the daughters of ^{238}U, ^{226}Ra ($T_{1/2}$ = 1600 (7) y) has a long half-life which enhances the concentration of ^{222}Rn and its progenies in the environment. ^{222}Rn is an odourless and colourless radioactive gas. Radon (Rn) is an inert gas and thus does not react with surrounding matter. It can readily move up through the ground and accumulate in the ambient air of a closed room. Presence of ^{222}Rn also gives rise to radiation background.

The impact of cosmic rays in Earth's environment acts as an extraterrestrial source of high energy γ-ray background. Primary cosmic rays originate outside Earth's atmosphere. They contain about 99% simple protons (*i.e.*, hydrogen nuclei) and alpha particles, around 1% of the nuclei of heavier elements and a tiny fraction of antimatter. Secondary cosmic rays are generated

when primary cosmic rays interact with Earth's atmosphere. They generally consist of γ-rays and a large variety of elementary particles, including mesons, protons, neutrons, electrons, and positrons [91]. High energy γ-rays (E > 3 MeV) and bremsstrahlung are produced when cosmic rays interact with the atmosphere of Earth and collide with ordinary matters.

In the present thesis work, we have concentrated on the environmental γ-ray radiation background till 3 MeV.

8.3 Experimental details

8.3.1 Venues of measurement

The Facility for Research in Experimental Nuclear Astrophysics (FRENA) laboratory is basically a surface laboratory at SINP, Kolkata. It is dedicated to perform low energy nuclear astrophysics experiments. It is a three storey building with four rooms at the ground floor : accelerator hall (27.300 m × 11.856 m), beam hall (22.600 m × 15.000 m), control room (7.200 m × 4.575 m), and data room (9.000 m × 6.000 m), respectively. On the other floors, the associated laboratories are being developed. The accelerator hall and beam hall are well shielded with a 1.2 m thick concrete wall (Fig. 8.1). The ground floor has a roof made of 60 cm thick concrete material.

The γ-ray radiation background has been measured at different locations (Fig. 8.1), in the accelerator (A) and beam halls (B and C) as well as in the control room (C) to get the integral background count rate at each place.

To compare the effect of concrete shielding in the accelerator and beam halls, we have chosen two nuclear physics laboratories (Lab I and II) with nearly 25 cm thick standard brick walls (Fig. 8.2) in our present work. The rooms are situated on the first floor and second floor of a separate four - storey office building. The sizes of the laboratories are approximately one-third of the accelerator hall in the FRENA building.
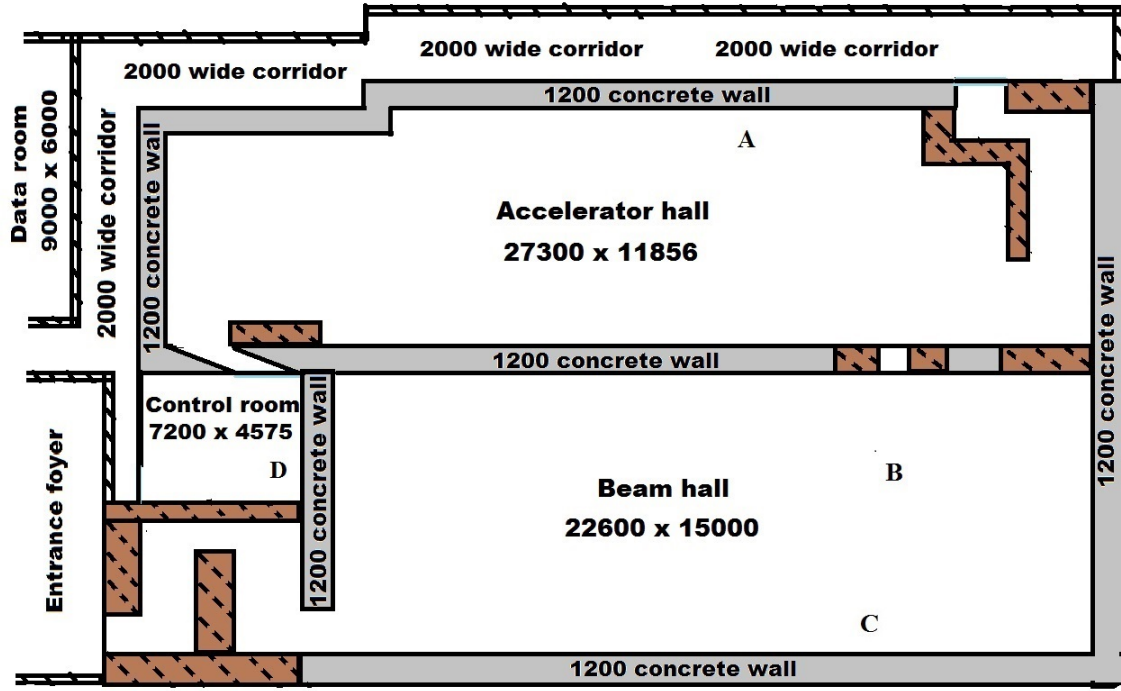
Figure 8.1: *The schematic diagram of the FRENA building ground floor. A, B, C, and D are the locations of measurements. The boundaries with no hatched lines are permanent concrete shielding walls, and the hatched line ones are the temporary shielding walls. All measurements are shown in mm.*

8.3.2   The detector and the data acquisition system

We have used an n-type coaxial HPGe detector with 80 cm^3 active volume and 20% relative efficiency [92] for the measurement of γ-ray background at all the venues described earlier. The relative efficiency of the HPGe detector, quoted by the manufacturer, refers to the relative full energy photopeak (FEP) efficiency with respect to the absolute FEP efficiency of a $3^"$ $\times$ $3^"$ (7.62 cm $\times$ 7.62 cm) (diameter $\times$ height) NaI(Tl) crystal, for the 1.33 MeV peak of a ^{60}Co source placed 25 cm from the detector. The HPGe detector crystal has a diameter of 5.1 cm and a length of 4.2 cm. To take the experimental data, we have used a CAEN 5780M [93] desktop digitizer (14 bit, 16k channel, and 100 MS/s). The digitizer has been equipped with DPP-PHA (Digital Pulse Processing-Pulse Height Analyzer) firmware that enables it to provide not only precise energy and timing information but also a portion of waveform and the other traces for fine-tuning of PHA settings [93].
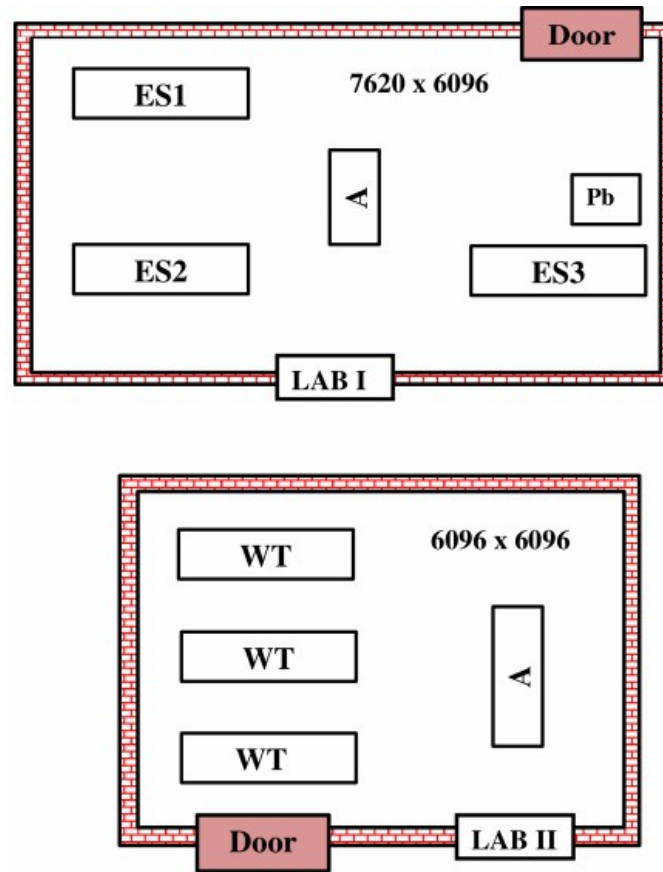
Figure 8.2: *The schematic diagram of the two laboratories, Lab I and Lab II, where A in each lab indicates the location of measurement. The working tables are indicated as WT, other experimental setups as ES1, ES2, and ES3. Pb indicates the Pb castle used for storing radioactive sources.*

8.3.3 Experimental setups

8.3.3.1 Setup at FRENA lab

To check the effectiveness of the concrete wall and also its contribution in background γ-ray radiation, at first, the HPGe detector has been placed at several locations in the FRENA accelerator building. Data have been taken with a bare HPGe detector without any additional passive or active shielding. The measurement time has been varied from several hours to days to have reliable counting statistics.

8.3.3.2   Setups at nuclear physics laboratory

The measurements of ambient γ-ray radiation background have also been carried out at the nuclear physics laboratories (Lab I and Lab II). These laboratories are situated at the second (Lab I) and first floor (Lab II) of a neighboring four-storey building. Data have acquired with a bare detector without and with passive and active shielding at each location. The different setups are discussed below one by one.

- **Setups at Lab I**

  - **No shielding:**

    The ambient γ-ray radiation background has been acquired with the bare HPGe detector. The detector was placed away from the walls (marked as A in Lab I of Fig. 8.2). This laboratory has a few nuclear γ-ray spectroscopy setups (indicated as ES in Fig. 8.2). The regularly used laboratory radiation sources also have been stored in this laboratory in a Pb castle (indicated as Pb in Fig. 8.2). Thus the ambient background is comparatively higher than in the other neighboring rooms.

  - **With passive shielding:**

    The detector has been placed inside a 2 cm thick square box made of lead (Pb: Z=82). Additional 40 lead rectangular blocks, each with 2.5 cm thickness, have been used to cover the box from all sides. The effective thickness of Pb bricks is nearly 7 cm. The detector encasing has been covered with 0.1 cm of Cu liner to cut the Pb X-rays. The inner, top and total view of the shielding arrangement are shown in Fig. 8.3.

- **Setups at Lab II**

  - **No shielding:**

    The ambient γ-ray radiation background have been acquired with the bare HPGe detector by placing it distant from the walls (marked as A in Lab II of Fig. 8.2).

  - **With passive shielding:**

    A NaI(Tl) cylindrical SUM spectrometer consisting of six large sectors of NaI(Tl)
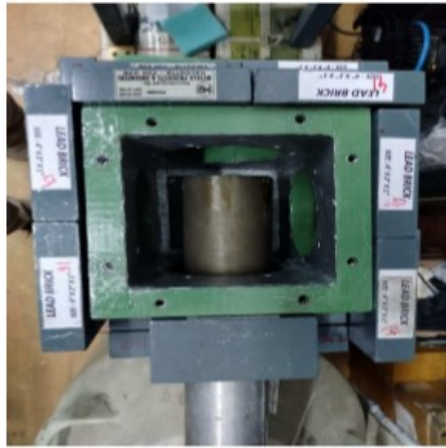
(a) Inner view (1 mm Cu liner and lead square box)
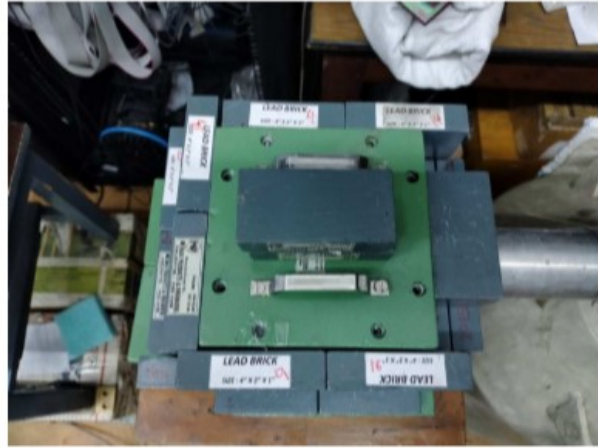
(b) Top view

(c) Total view

Figure 8.3: *(a) Inner view (0.1 cm Cu liner and lead square box), (b) top view, and (c) total view of Setup at Lab I with passive shielding.*

detectors is available at Lab II. The length of the SUM spectrometer is 46 cm, and the diameter is 30 cm (Fig. 8.4). Here, each of the detector modules is coupled with one photomultiplier tube (PMT) at one end. There is a borehole of 8 cm in diameter at the center of the cylindrical assembly. The HPGe detector used by us has a long neck and the neck has been inserted inside the borehole. The SUM spectrometer has been utilized here as passive as well as active shielding for the HPGe detector.

The experimental setup has been shown in Fig. 8.5. Additional Pb bricks have been inserted in the borehole to fill the gaps to improve the passive shielding effect further.
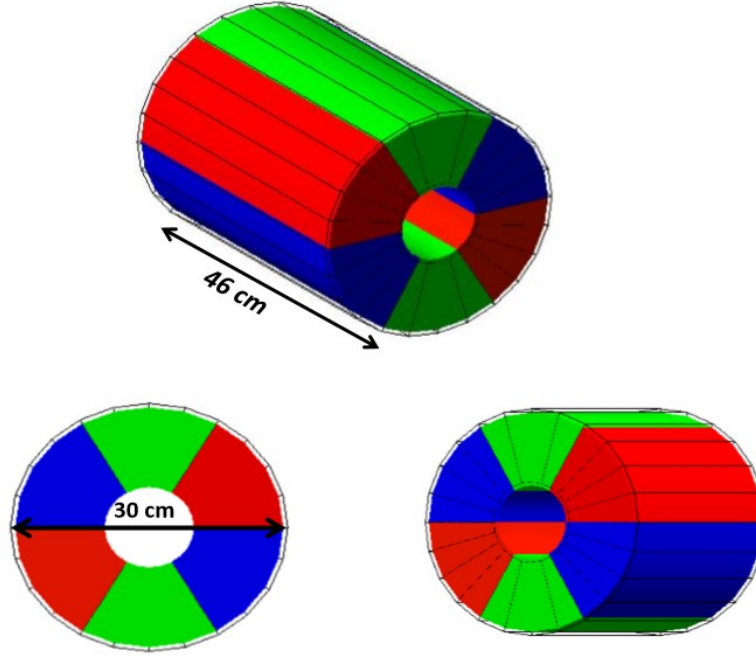
Figure 8.4: *The schematic diagram of the SUM spectrometer with six sectors of NaI(Tl) detectors shown from different angles. The dimensions are indicated in the diagram.*

– **With active shielding:**

   The SUM spectrometer has also been used as an active shielding for the HPGe detector. The positive bias voltage (+1000V) of the SUM spectrometer has been provided from the DT5533EM modules developed by CAEN for the six PMTs of the six sectors of NaI detectors. The CAEN DT5780M desktop digitizer module provided the negative bias voltage (-3000V) of the HPGe detector. The HPGe data have been acquired, ensuring anti-coincidence with the SUM spectrometer signals. The improvement in the background suppression has also been studied by changing the anti-coincidence time window from 1 μs to 1.5 μs, and finally to 2 μs. We have obtained the best suppression at time window of 1 μs. Our group has reported the preliminary results in Ref. [94].

Figure 8.5: *The shielding arrangements at Lab II with SUM spectrometer for the same 20% relative efficiency HPGe detector. The empty space in the SUM spectrometer borehole has been blocked with Pb blocks from one end and the HPGe detector is inserted from the other end.*

8.4 GEANT4 simulation

Simulation tools have been widely used along with the experimental measurements, to understand the effectiveness of the radiation shielding. In the present work, the simulations have been carried out using the GEANT4 Monte Carlo toolkit [47]. It enables accurate simulation of the passage of particles through matter. Here, I have used the low energy electromagnetic physics models (valid from 250 eV to 100 GeV) to model the photon interactions with the detector throughout the simulations. The simulation basically consists of a series of classes like detector construction and building material, particle and physics process definition, particle tracking, stepping action and event action, *etc*. To create the γ-photons, I have used the General Particle Source (GPS) module in GEANT4. The energy deposition is recorded step-by-step and after that added for each event in event action class. The energy resolution and cut off values are incorporated properly in the simulation. Two simulation model geometries have been used to optimize the shielding. They

are discussed one by one below.

8.4.1 Model Geometry 1

In the case of outdoor open fields, the assumption of an infinite half-space source, which means a 2π-source geometry can reliably simulate the natural background radiations. But, the indoor source geometry is not easy to be realistically modelled through simulation. The authors in Ref. [88] have used an approximate 4π-geometry irradiation source for the radiation field in the buildings surrounded by concrete walls.
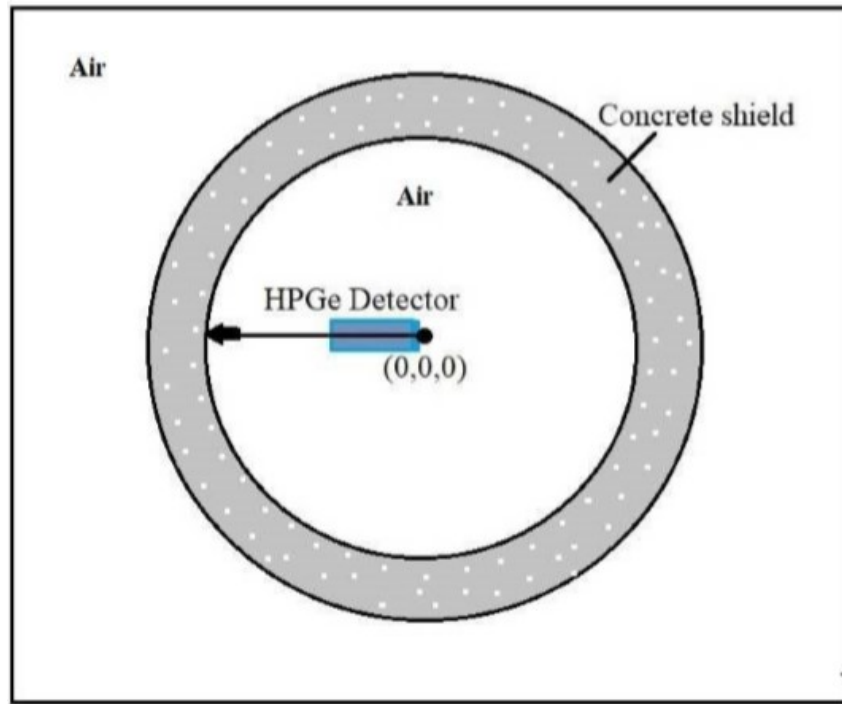
Figure 8.6: *A cross-sectional view of spherical shell geometry model showing the concrete shield. The HPGe detector is placed at the centre of the sphere. The radioactive particles are isotropically distributed within the concrete material. The entire design is enclosed in a box, filled with air. The figure is drawn not to scale.*

In the present work, we have assumed a spherical concrete layer with an isotropic distribution of natural radioactive nuclei. The HPGe detector with 20% relative efficiency has been placed in the middle of the spherical shell. The spherical layer is made out of concrete with a density of 2.35 g/cm^3. I have considered the composition by weight of ordinary concrete as provided in Ref. [95] in the present simulation (see Table 8.1).
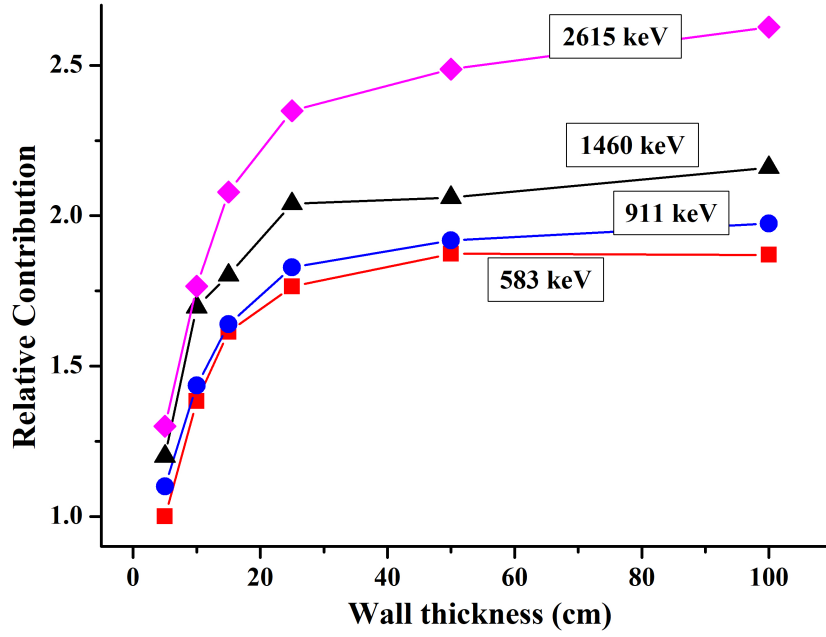
Figure 8.7: *Variation in the yield of γ-rays originating from different radionuclides (583 keV, 911 keV and 2615 keV from ^{232} Th and 1460 keV from ^{40} K) as a function of the concrete wall thickness. From the figure, it is clear that the contribution from different γ-rays saturate after a certain thickness. The yields for 5 cm wall thickness have been considered as 1 for all the γ-rays. However, for better clarity of the figure, a factor of 0.1 has been added to the ratio for 911 keV, 0.2 for 1460 keV and 0.3 for 2615 keV.*

The model geometry has been shown in Fig. 8.6. The γ-ray photons are generated using the GPS module. The concrete wall acts as an isotropic extended γ-ray radiation source. The photon energy spectra have been simulated for intense γ-rays emitted by long-lived radioactive nuclei, like ^{40}K, ^{232}Th and ^{226}Ra or their progenies, which are typically found in room background radiation spectra. Then, the variation of photopeak areas of γ-rays of various energies have been plotted as a function of concrete wall thickness (see Fig. 8.7).

8.4.2 Model Geometry 2

In the second case, the model geometry is built with a Pb shielding layer surrounding the HPGe detector with 20% relative efficiency. A point source is placed at 30 cm from the detector front face (Fig. 8.8). The highest energy γ-ray available in the room background is 2.615 MeV coming
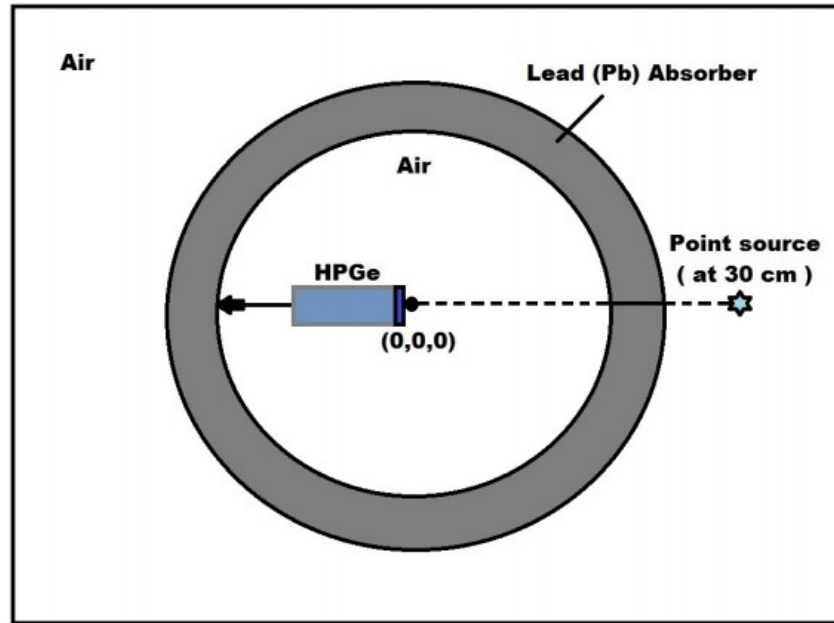
Figure 8.8: *A cross- sectional view of spherical shell geometry model showing the Pb shield. The HPGe detector is placed at the centre of the sphere. The point radioactive source is placed at a distance of 30 cm (from the centre) outside the Pb shield. The entire design is enclosed in a box, filled with air. The figure is drawn not to scale.*

from ^{208}Tl. Now, to check the effectiveness of the lead shielding, 5×10^6 γ-ray photons of 2.615 MeV energy have been thrown isotropically from the point source in 4π-direction. The total numbers of photons reaching the detector have been recorded. The thickness of the lead shield is varied from 0 cm to 16 cm. Percentage of the initial count of γ-ray photons, which are finally detected by the detector is plotted in Fig. 8.9.

8.4.3   Model Geometry 3

Similar to model geometry 2, an HPGe detector has been placed at the middle of a spherical shell like Fig. 8.8. In spite of lead, the shell has been made with concrete material. A point source is placed at a distance of 150 cm from the detector front face in the air outside the shell. 10^7 gamma-photons are thrown isotropically from the point source in 4π-direction. The thickness of the concrete shield has been varied from 0 to 120 cm untill the gamma-rays are fully stopped in the concrete shielding wall. We basically want to check the effectiveness of thick concrete wall as a shielding for the outdoor gamma-radiation.
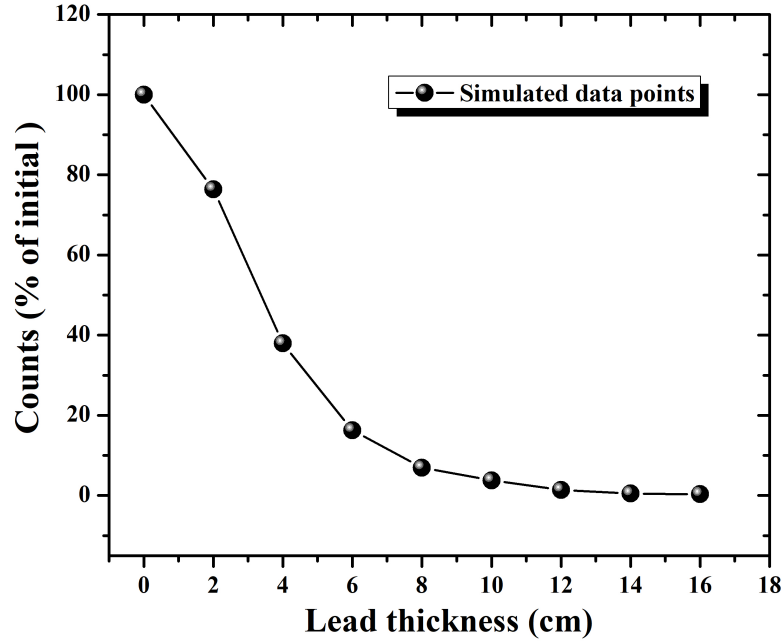
Figure 8.9: *The percentage of total counts detected in the detector with respect to the incident flux as a function of lead shielding thickness. The energy spectrum in each case is simulated at a fixed source position with 5×10^6 incident γ-ray photons with energy 2.615 MeV. The number of photons reaching the detector in the absence of a Pb absorber (0 cm of Pb thickness) has been normalized to a value of 100 % detection.*

8.5 Results and discussions

8.5.1 Experimental results

We have been measured the indoor background spectra at different locations of the FRENA building like accelerator hall (A), beam hall middle (B), near beam hall wall (C) and control room (D) as shown in Fig. 8.1. As per expectation, the photopeak count rates of relatively low energy (< 1.5 MeV) γ-rays are highest in the counting room (D). However, the variation of the photopeak count rate of 2.615 MeV γ-ray is within 4% between different measurement positions (B, C, and D). Interestingly, the photopeak count rate of 2.615 MeV γ-ray in the accelerator hall near the concrete wall (A) is 25% less than the other locations. The background spectrum which has been measured in the FRENA accelerator hall, is shown in Fig. 8.10 in comparison with the data acquired in the two nuclear physics laboratories (Lab I and II) [96].

Table 8.1: *Elemental composition of ordinary concrete [95] which has been considered in the present simulation.*

Element	Amount (g in each 2.35 g)	Weight fraction
Hydrogen	0.013	0.005
Oxygen	1.165	0.496
Silicon	0.737	0.314
Calcium	0.194	0.083
Sodium	0.04	0.017
Magnesium	0.006	0.002
Aluminium	0.107	0.046
Sulphur	0.003	0.001
Potassium	0.045	0.019
Iron	0.029	0.012
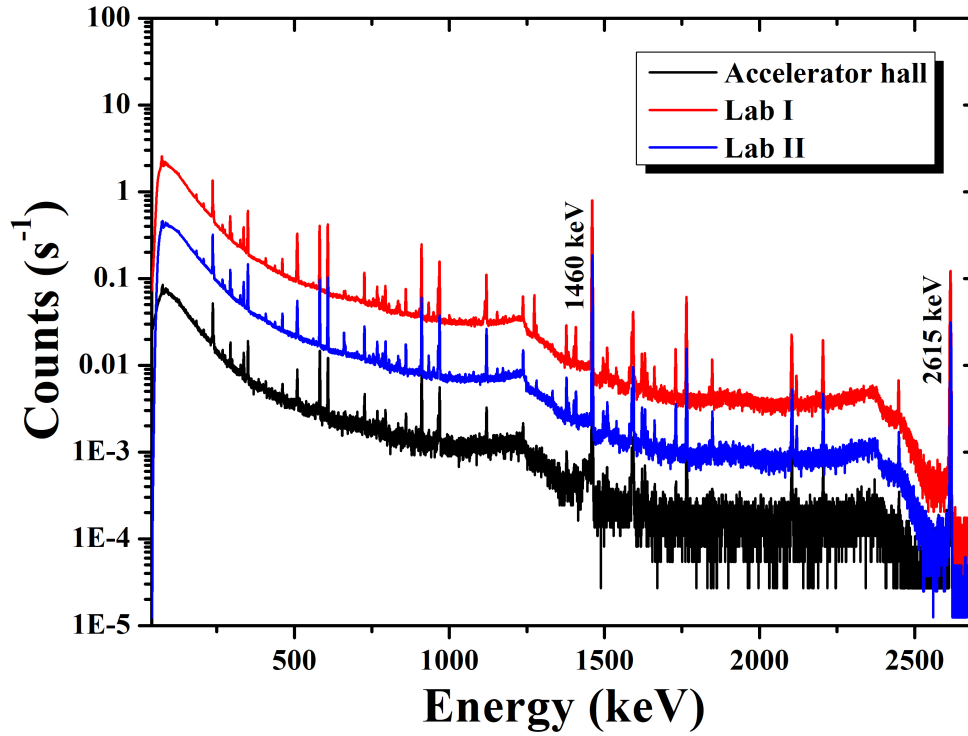
Figure 8.10: *Comparison of normal γ-ray background at FRENA building accelerator hall, Lab I and Lab II respectively. The two intense photo-peaks of 1460 keV and 2615 keV γ-rays are shown in the figure.*

It is clear from Fig. 8.10 that the count rate at FRENA accelerator hall is lower than the rate at Lab I and II. The sizes of the FRENA hall, Lab I and Lab II are not similar [96]. The Lab I and Lab II are surrounded by standard red brick walls ($\approx$ 25 cm thickness), while the FRENA hall is enclosed by 1.2 m thick concrete walls. Due to this, the number of radioactive nuclei present in the walls is also different. The thick concrete walls contain more radioactivity in itself as it has larger volume. But they also shield the environmental radiation generated from surroundings from reaching the HPGe detector. The red brick walls are not so effective as a shield as the concrete walls. Moreover, the background radiation also varied at FRENA accelerator hall and the two laboratories due to the larger distance of the detector from the surrounding walls at FRENA. The detection efficiency of a detector decreases sharply with the square of the distance from the source [96].

The HPGe detector has been placed at the nuclear physics laboratories, to test the effectiveness of passive and active shieldings. The results are discussed below.

To check the shielding effect of Pb bricks, the spectra have been taken with two different conditions, *i.e.*, normal room background spectrum without any shield and the spectrum with the effective Pb shield (see Fig. 8.3), respectively, at Lab I. The comparison between the two spectra have been plotted in Fig. 8.11. In the presence of Pb shield, the photopeak areas of the most intense peaks in the γ-ray background spectrum, 1.460 MeV and 2.615 MeV, are reduced by a factor of 45 and 36, respectively.

The passive and active shielding setup at Lab II (shown in Fig. 8.5) can be utilized for background suppression. After placing the HPGe detector inside the borehole of the SUM spectrometer, the total integral count rate is reduced by a factor of 10. The amount of reduction factor increases to 15 after adding some additional Pb blocks inside the borehole. After that, we have used the SUM spectrometer both as a passive and active shield. Compared to the normal room background, it improves the suppression further by a factor of 22. The comparison between the spectra have been shown in Fig. 8.12. The integral count rate have been checked by varying the anti-coincidence time window from 1 μs to 2μs. The best suppression is with the lowest, *i.e.*, 1 μs time window [96].
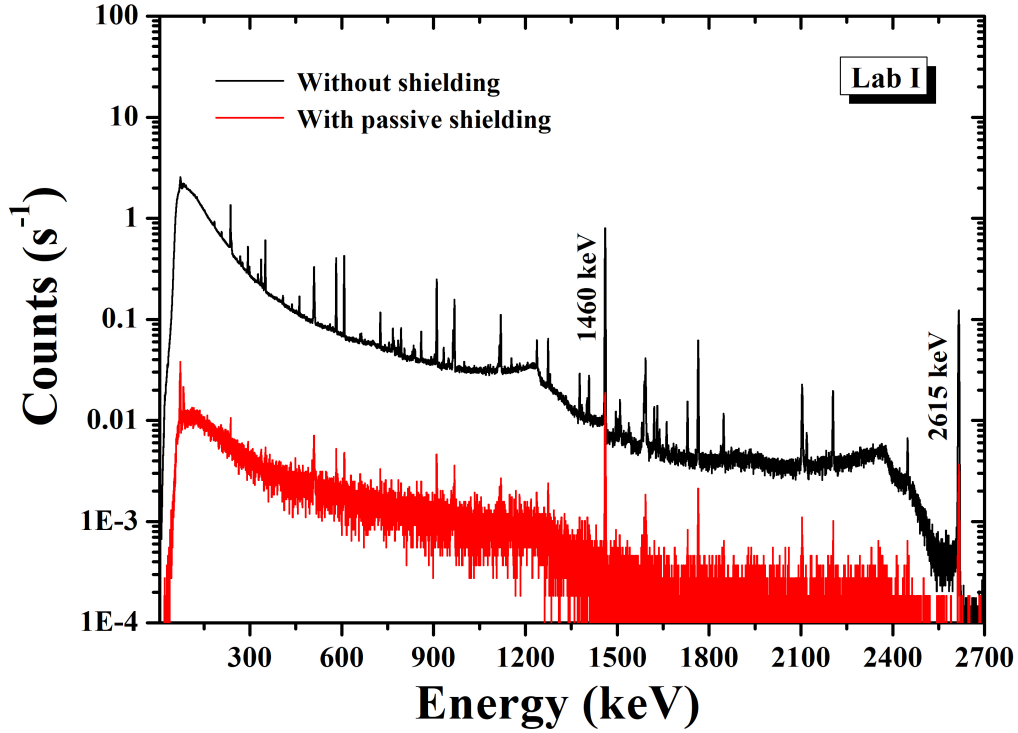
Figure 8.11: *The spectra drawn with a black line correspond to room background without any shield at Lab I, and that with a red line correspond to data acquired with the HPGe in a Pb shielding. The overall background suppression is ten-fold in the presence of a passive Pb shield.*

A detailed analysis of the spectra covering the entire range (50-3000 keV) has been performed by dividing the spectra in four parts – (a) 50-500 keV, (b) 500-1000 keV, (c) 1000-2000 keV, and (d) 2000-3000 keV. The count rates (s^{-1}) for all setups discussed above are given in Table 8.2.

To get an idea about the activity concentrations in the measurement places, we have plotted the values of the ratios of the background count rates to the intensities of decay γ-rays of ^{214}Bi, ^{214}Pb of ^{238}U decay series and ^{228}Ac, ^{208}Tl, ^{212}Pb of ^{232}Th decay series as a function of energy, similar to Ref. [83] for accelerator hall and Lab I. Both the plots are given in Fig. 8.13.

At each location, data for ^{232}Th and ^{238}U decay series follow similar shaped efficiency function. It indicates that the long-lived ^{232}Th and ^{238}U radionuclides are distributed similarly in the FRENA hall. It is also true for the Lab I. As the same detector has been used in both the locations, the efficiency curves generated for FRENA accelerator hall and Lab I are quite
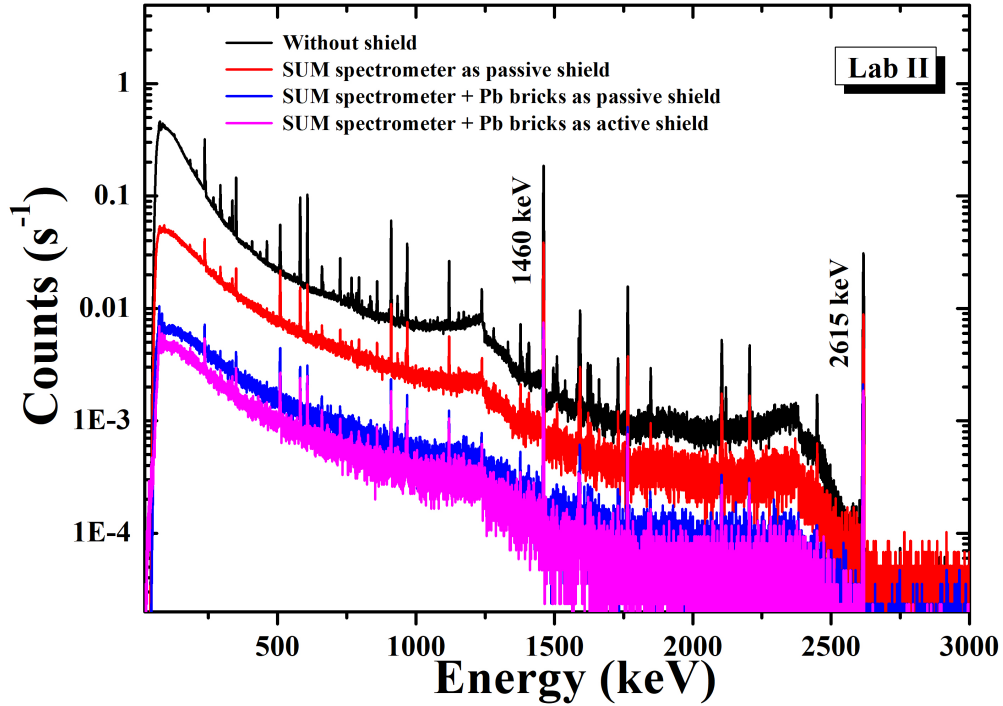
Figure 8.12: *The spectra drawn with (i) black line corresponds to room background without any shield at Lab II, (ii) red line corresponds to SUM spectrometer as passive shielding, (iii) blue line corresponds to SUM spectrometer as passive shielding + additional Pb bricks and (iv) magenta line corresponds to SUM spectrometer with extra Pb bricks + active shielding with 1 μs time window. The total background suppression using this set up is 22 fold.*

similar. The smaller distance of the walls of Lab I from the detector resulted in higher efficiency of detecting background γ-ray radiation compared to the FRENA halls [96].

8.5.2 Simulation results

The simulated photon energy spectra with model geometry 1 are shown in Fig. 8.14. The spectra have been obtained for various wall thicknesses, 5, 10, 15, 20, 25, 50 and 100 cm, respectively. We have considered only the 1.460 MeV γ-ray from a ^{40}K source with the same concentration per unit thickness of the wall in each cases. The Compton scattered part of the 1.460 MeV γ-ray has been shown in the inset of Fig. 8.14(a). As the wall thickness increases, the Compton scattered part increases sufficiently. However, the FEP count saturates beyond 25 cm of wall

Table 8.2: *The count rates (s^{-1}) for all configurations in energy range 50-3000 keV. The configurations in detail are mentioned in the footnote below the table (taken from Ref. [96]).*

Energy range	Configurations						
	C1[1]	C2[2]	C3[3]	C4[4]	C5[5]	C6[6]	C7[7]
(keV)							
50-500	1207.94	10.47	42.08	253.68	43.69	7.04	4.71
500-1000	126.10	3.15	4.47	28.15	9.58	1.93	1.26
1000-2000	68.77	1.95	2.49	15.54	4.95	1.00	0.69
2000-3000	9.98	0.31	0.38	2.28	0.83	0.17	0.12

[1]Lab I: without any shielding
[2]Lab I: with nearly 7 cm of Pb shielding
[3]FRENA Accelerator hall (A) without shielding
[4]Lab II: without any shielding
[5]Lab II: SUM spectrometer as passive shield
[6]Lab II: SUM spectrometer as passive shield + Pb bricks
[7]Lab II: SUM spectrometer as both passive shield + active shield + Pb bricks
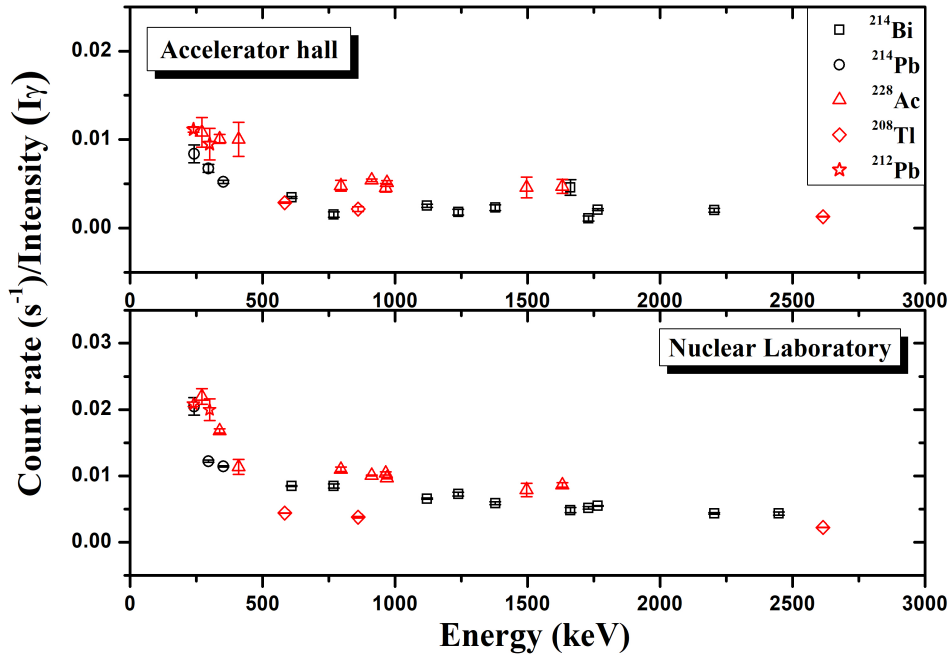
Figure 8.13: *.The ratio of the background count rates (s^{-1}) to the intensities of γ-rays emitted by radioactive progenies ^{214}Bi, ^{214}Pb of ^{238}U decay series and ^{228}Ac, ^{208}Tl, ^{212}Pb of ^{232}Th decay series have been plotted as a function of energy. Data have been acquired at accelerator hall of the FRENA building and Lab I. The nature of the plots, indicates a similar distribution of the long-lived radionuclides in both the indoor environments.*
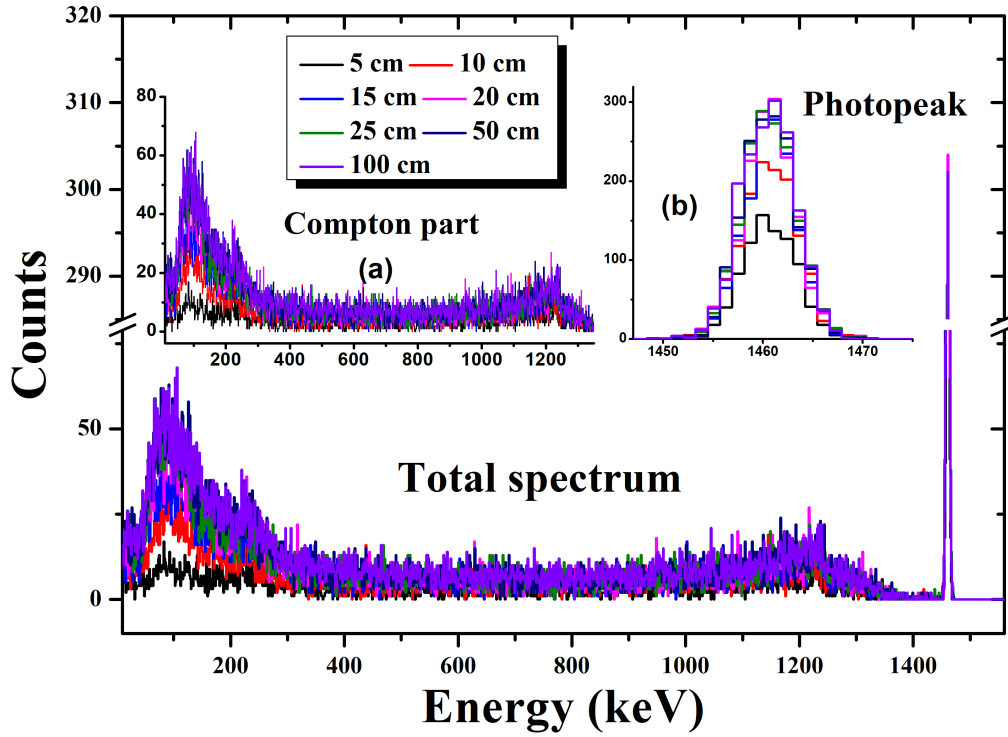
Figure 8.14: *Energy distribution spectra of 1.460 MeV at different concrete wall thicknesses with same activity concentration of ^{40}K - (a) in case of scattered part of γ-ray radiation, it increases as the wall thickness becomes thicker, (b) the saturation in full energy photopeak (FEP) height beyond 25 cm is seen.*

thickness (Fig. 8.14(b)).

The relative contribution of γ-rays originated from different progenies of long-lived radioiso-topes are plotted as a function of wall thickness in Fig. 8.7. From Fig. 8.7, it is clear that the saturation in FEP area can be achieved earlier at smaller wall thicknesses for lower FEP energy. So, γ-rays coming beyond 25 cm of the wall do not contribute to the indoor energy spectrum because they are scattered and absorbed within the wall. With the 1.2 m thick concrete wall, the γ-rays coming from outside environment till 3 MeV, are almost completely absorbed [96].

The percentage of the total initial counts of 2.615 MeV γ-ray photons, which are finally detected by the detector, has been plotted in Fig. 8.9 as a function of the thickness of the lead absorber. The initial γ-ray flux is reduced to 0.33% after passing through nearly 16 cm of a lead shield with the geometry model 2 (see Fig. 8.8).

With model geometry 3, 10^7 gamma photons with energy 2.615 MeV have been thrown towards the detector front face from a point source at a distance of 150 cm from centre position. The gamma-rays of 2.615 MeV energy are almost completely absorbed within the wall With 120 cm or 1.2 m thick concrete wall. Therefore, no gammas will reach the detector from the outdoor environment. In case of 10 MeV gamma-ray, only 3% of gamma- photons are able to reach the HPGe detector with 1.2 m thick concrete wall (considering the total number of events in presence of no absorber is equal to 100%). Thus the concrete walls also serve as a shielding for the high energy gammas, which originates from the interaction of the cosmic rays with the atmosphere of the earth.

8.6   Summary and future plan

Background spectra have been taken at different positions of the FRENA building and also at our nuclear physics laboratories with the help of an HPGe detector. The count rate in the FRENA experimental hall is lower than at our nuclear physics laboratory due to the differences in size and construction materials. After that, the integral count rates have been calculated for various energy regions in different shielding configurations. The shielding arrangements at our laboratory using different accessories will be useful to decrease the indoor background further at FRENA building. The experimental data confirms that long-lived uranium and thorium are uniformly distributed inside the laboratory environment. Simulations have been done to understand and study the shielding arrangements further. The effectiveness and the contribution of the concrete shielding in the natural γ-ray background has also been studied using the 4π-geometry source irradiation. From the simulation, it is clear that the 1.2 m thick concrete shielding protects the inside from the outside environmental radiation. Only radionuclides distributed up to 25 cm inside the wall contribute to the indoor γ-ray background. The simulation is also really useful to estimate the passive shielding thickness of the real experimental setup. The initial γ-ray flux reduces to 0.33% in the presence of 16 cm thick lead absorber (in case of a 2.615 MeV γ-ray).

The background study is truly beneficial to plan the low energy astrophysical experiments at FRENA. In the future, we will use the shielding setups in the in-beam experiments at FRENA to eliminate the unwanted background γ-ray events from the actual events.

Chapter 9

SUM spectrometer characterization

9.1   Introduction

Sum spectroscopy or total absorption spectroscopy (TAS) method has been used basically to measure the β-decay branching ratios, half-lives of neutron rich nuclei and very weak nuclear cross-sections for nuclear astrophysics. These kinds of neutron rich nuclei can be artificially produced in the nuclear fission reactor. In case of nucleosynthesis, the neutron rich nuclei have been produced through neutron capture reactions. So, β-decay feeding pattern, β-decay half-lives play significant role in understanding the nucleosynthesis processes in stellar sites beyond the iron (Fe) nuclei. For β-decay studies, along with high resolution gamma spectroscopy, high efficiency total decay heat measurements are also essential to reduce the chances of missing transitions and weak β-feeding branches. This kind of high efficiency detector is also useful to measure very low cross-sections precisely which are important in the astrophysical scenario. So, TAS or γ-summing method is useful for such kind of studies. But, these kinds of detectors are really difficult to handle and rely largely upon Monte Carlo simulations to interpret the

experimental data. So, one have to characterize the SUM spectrometer precisely before using it in actual measurements. After that, the measurements will provide data both for the decay heat calculations used to take care of the nuclear waste from the fission reactors and on nuclei approaching the r-process for astrophysics community and new nuclear structure information for the basic nuclear physics community.

9.2   The Total Absorption Spectroscopy (TAS) method

When we move far away from the line of stability, the Q-value for β-decay becomes large. Thus the daughter nuclei which follow the β-decay can be populated in regions of high level density and at high excitation energy. It basically results to a fragmented decay with many weak β-decay branches. Then, it corresponds to the multiple γ-ray decay pathways from each of the higher lying daughter levels to the daughter ground state. The identification of these weak branches is almost impossible with the conventional high resolution γ-spectroscopy technique, as suggested by Hardy *et al.* [97]. Hardy and his co-workers introduces a term "Pandemonium effect" which basically stands for the problems someone faces when constructing a complex level scheme from high resolution data in a β-decay experiment. The main difficulty is the poor efficiency of the Ge detectors. If some γ-ray has poor intensity then we may miss the particular γ-peak in our spectrum. So, our level scheme is incomplete and the feeding pattern is not correctly determined.

Due to this the total absorption spectroscopy method has been adopted to study the β-decay of the neutron rich nuclei. This method is based on the γ-summing technique. For this purpose, large NaI(Tl) scintillator detectors covering a solid angle of almost 4π for photons to be emitted from the target placed at the centre, have been used. The large response time of the NaI(Tl) detector (~ 100 ns) helps in full absorption of the photons emitted from the cascade. This is due to the fact that the photomultiplier is unable to distinguish between different photons that are emitted within small interval of time (smaller than the decay time of the detector ~ 250 ns). In case of ideal 4π - TAS detector, we get only one peak (known as the sum peak) which has the energy equal to the level of excitation (E_x). The advantage of the γ-summing technique is that
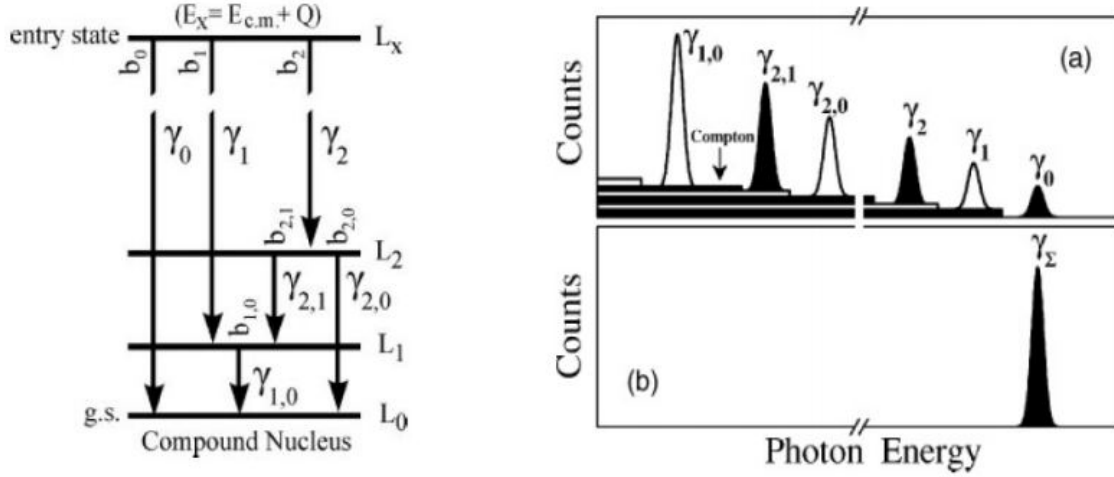
Figure 9.1: *Decay scheme of the compound nucleus produced in a capture reaction at an excited state E_x (left side). Typical γ-spectra for the de-excitation of compound nucleus by using small NaI(Tl) crystal (right side marked as 'a') and a large volume 4π - summing detector (right side marked as 'b'). In case of ideal 4π - detector, we get only one sum peak with energy equal to E_x. The difference between a single crystal detector and a summing detector has been clearly seen in this figure.*

one has to analyze the sum peak only, not the individual γ-lines from the de-excitation. The TAS method or γ-summing technique has been illustrated through a schematic representation in Fig. 9.1. But, in real situation no TAS detector is 100% efficient. So, the intrinsic detector properties, combined with the large number of β-feeding levels, produces a complex detector response. Thus the TAS method depends heavily on the Monte Carlo simulation for the unfolding of the individual β-feeding level signatures from the observed spectrum.

9.3 Neutron capture: r-process

The astrophysical r-process is a process of rapid sequence of successive neutron captures, followed by β-decays. The processes occur in explosive stellar events such as supernovae, and are behind the formation of many heavy nuclei above iron (Fe). The informations of masses and lifetimes are necessary for our general understanding of the r-process. As well as the measurements of β-decay feeding pattern, well-understood level schemes, for which TAS method will play an important role, will be very effective for making detailed predictions of the r-process.

9.4   The decay heat

The decay heat in nuclear fuel is the heat energy produced in a radioactive decay of products resulting from fission. For the design and operation of nuclear reactors, the time behaviour of this quantity is critical. It affects the fuel removal and reloading processes, safety after accidents (such as a loss of coolant incident), as well as the storage, transport and reprocessing requirements for the spent fuel. Now, to calculate the time evolution of the decay heat, one requires the informations related to the fission yields, β-decay lifetimes, the β and γ-ray decay schemes for all of the fission products and their subsequent daughter which are decaying back to the stability line. But, it is difficult to get all the informations for these neutron rich fission fragments with conventional γ-spectroscopy experiments. So, the decay heat calculations mostly rely on the theoretical estimates which have been suffering from inaccuracy in most of the cases. So, these kind of total absorption spectroscopy measurements are necessary to improve the design of the nuclear reactors.

9.5   TAS or SUM spectrometer at SINP

We have a SUM spectrometer at our laboratory which has been used as a passive shielding in a previous work (discussed in chapter 7). Now, we want to use the detector for β-decay, r-process capture reaction measurements. It is basically a cylindrical shaped detector with six sectors of NaI(Tl) detectors. The SUM spectrometer has a length of 46 cm and a diameter of 30 cm. But, only one PMT is attached with each of the six sectors at one end of the detector. There is borehole at the centre of the cylindrical assembly which has a diameter of 8 cm. The sources have been placed along the axis of the summing detector. Due to unavailability of the user manual of the detector, it is of utmost importance that the details of each NaI(Tl) crystal have been studied individually with proper care. The SUM spectrometer has been shown in Fig. 9.2.
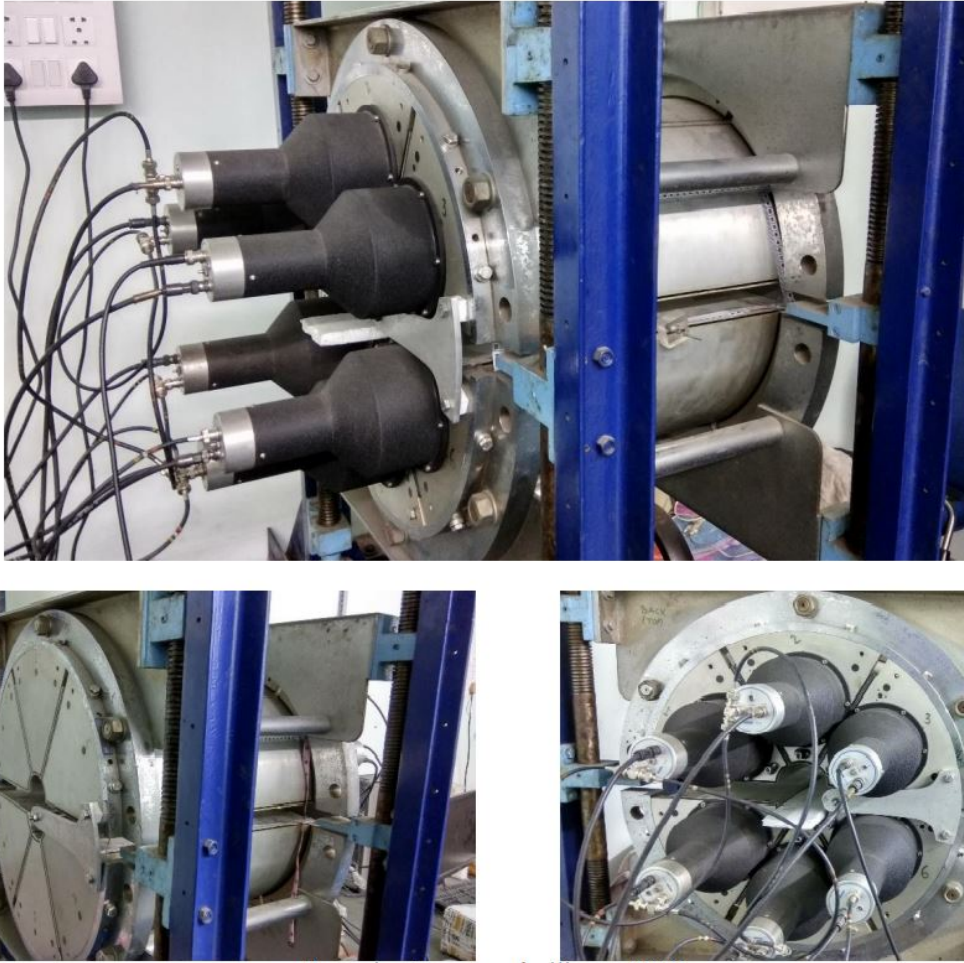
Figure 9.2: *The SUM spectrometer facility at SINP, Kolkata. The six detectors with six PMTs have been seen in the figure clearly.*

9.6 Observed characteristics of the SUM spectrometer

We have used CAEN DT5780M desktop digitizer [45] to give the bias voltage to the individual crystal and to acquire the energy spectra with ^{60}Co and ^{137}Cs sources. Here, I have discussed the observed characteristics only for one of the detectors. Similar kinds of properties have been followed by the other detectors.

9.6.1 Resolution

The performance of the γ-ray spectrometers depend on the resolution of the detector. The resolution of a detector depends on different parameters like bias voltage to the detector, op-
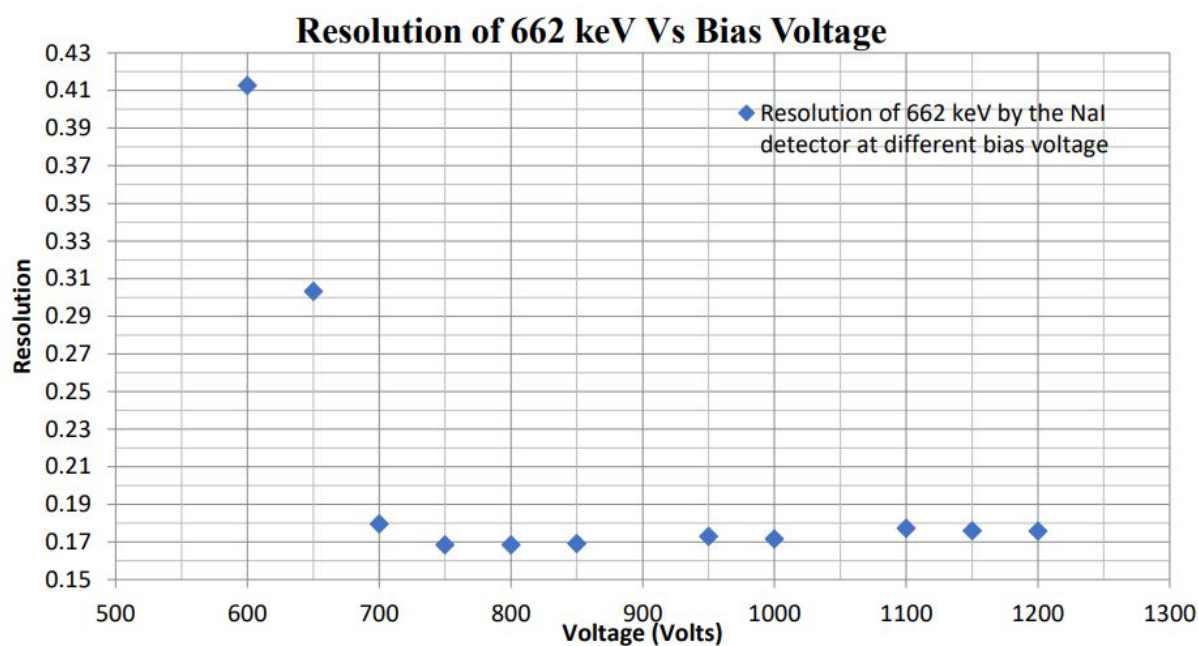
Figure 9.3:   *The resolution vs. bias voltage for 662 keV peak from the* ^{137}Cs *source for one of the detector among the six.*
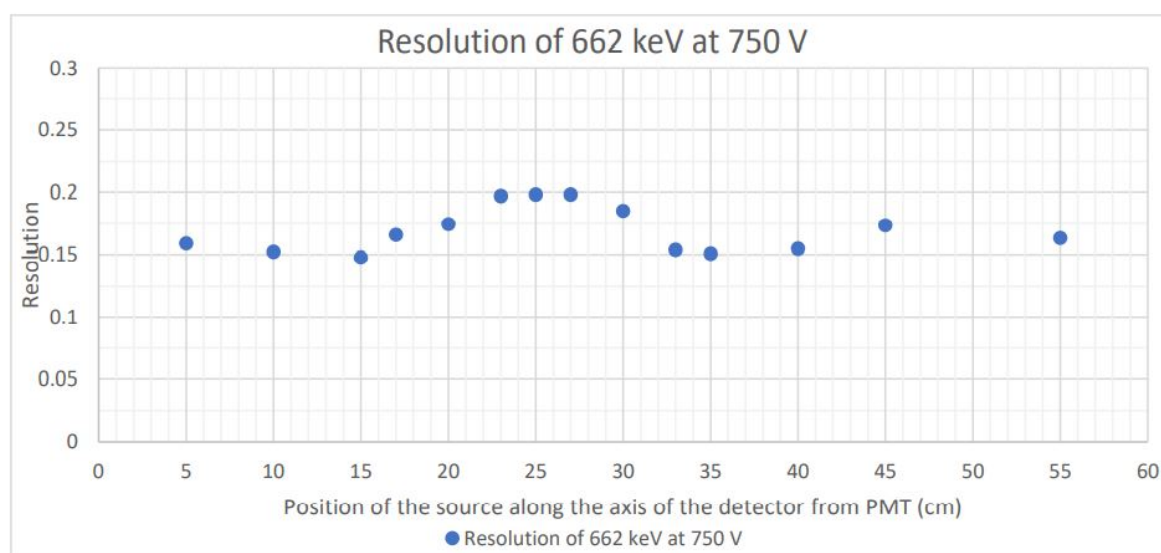
Figure 9.4:   *The resolution at different source positions along the central axis for 662 keV peak from the* ^{137}Cs *source for one of the detector among the six. The gradual increment in the resolution value from 20 to 30 cm has been clearly seen in the figure. The resolution is poorest at a distance of 25 cm from PMT.*
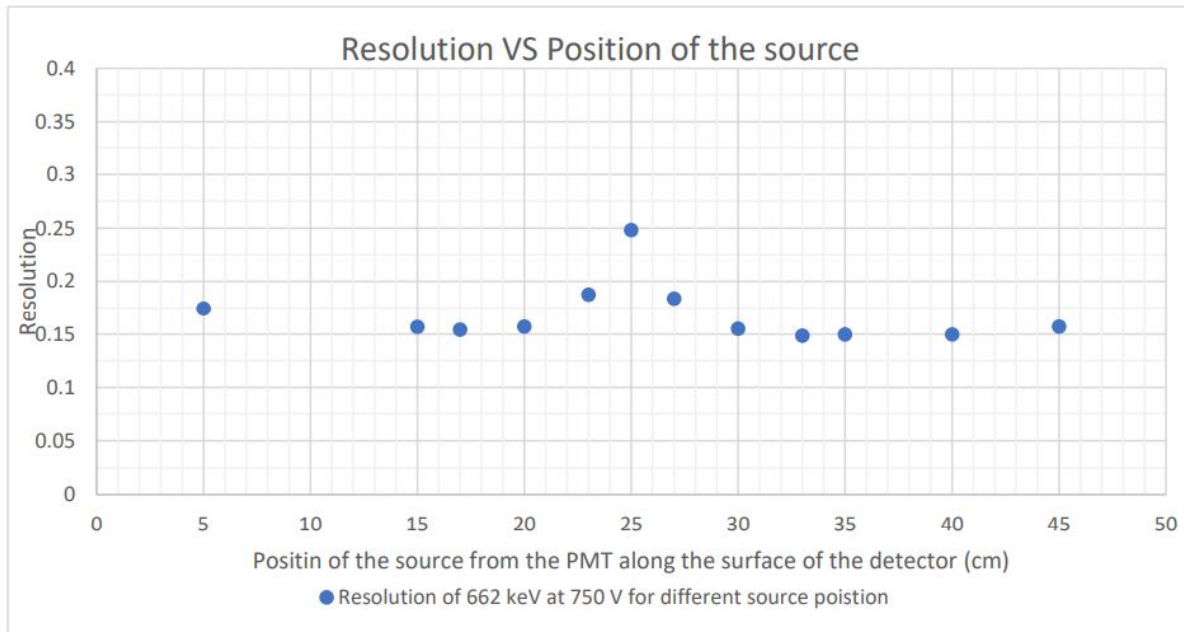
Figure 9.5: *The resolution at different source positions on the surface for 662 keV peak from the ^{137}Cs source for one of the detector among the six. The sudden rise and fall in the resolution value from 20 to 30 cm has been clearly seen in the figure. The resolution is poorest at a distance of 25 cm from PMT similar to Fig. 9.4 .*

timization of the data acquisition parameters (such as shaping time, pole zero, *etc.*) and the position of the source (in case of such summing detectors with long crystals). Here, we have checked the resolution of each individual crystal one by one as a function of varying bias voltage, source position. To check the resolution of the detector, ^{137}Cs source has been used during the measurements. The plot of resolution (R = $\frac{FWHM}{E_\gamma}$) vs. bias voltage for one crystal has been given in Fig. 9.3. As seen from the Fig. 9.3, the resolution is best at bias voltage 750 V and almost constant up to 1200 V. The observed optimum resolution was 16.8 % for 662 keV.

The resolution of the crystal also has been plotted as a function of different source positions. The data has been taken in two conditions – (1) by changing the source position along the axis of the detector, and (2) by changing the source position along the surface of the detector. The plots in two different conditions have been shown in Fig. 9.4 and Fig. 9.5. It can be observed from Fig. 9.4 that the resolution of the detector is almost the same around 15% at 662 keV, but gradually increases when the source's position is varied from 20 cm to 30 cm. The resolution is poorer at 25 to 27 cm. However, the resolution beyond 30 cm, decreases gradually and behaves
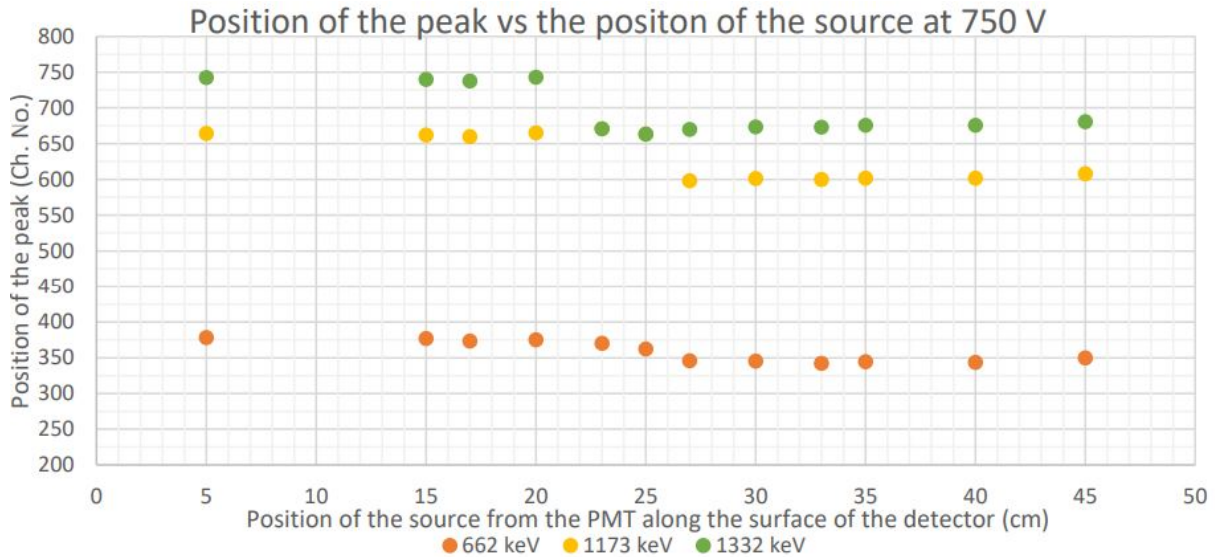
Figure 9.6: *Position of the photopeak for different energies vs. the distance of source from the PMT. As the distance of the source from the PMT increases, the peak position shifts to left in the energy spectrum, i.e., the channel number decreases.*

in a same manner as it does before 20 cm. In case of Fig. 9.5, the resolution is almost constant at distance less than 20 cm and greater than 30 cm. It shows the poorest resolution at around 25 cm. The nature of the resolution plot at two conditions are quite similar. Here, all the distances measured from the face where the PMTs are attached to the detector.

9.6.2   Peak position

As the PMT are only at one end of the big SUM spectrometer, the light collection to the PMT varies largely as a function of the source position. Thus, the photopeak position varies depending on the source position. We have fixed the bias voltage to 750 V for this measurement. The photopeak positions of 662 keV from ^{137}Cs source and 1173 and 1332 keV from ^{60}Co have been plotted as a function of the position of the source from PMT (see Fig. 9.6). From Fig. 9.6, it can be observed that the variation of the photopeak position is more in the higher energies compared to lower energies. The photopeak shifts towards left side, *i.e.*, at lower channel number with the increase in the distance of the source from the PMT, especially after 25 cm.

However, there is some anomalous behaviour of the detector response at around 25 cm. The energy spectra of ^{60}Co and ^{137}Cs at 20 cm, 23 cm and 27 cm have been compared in Fig. 9.7. It
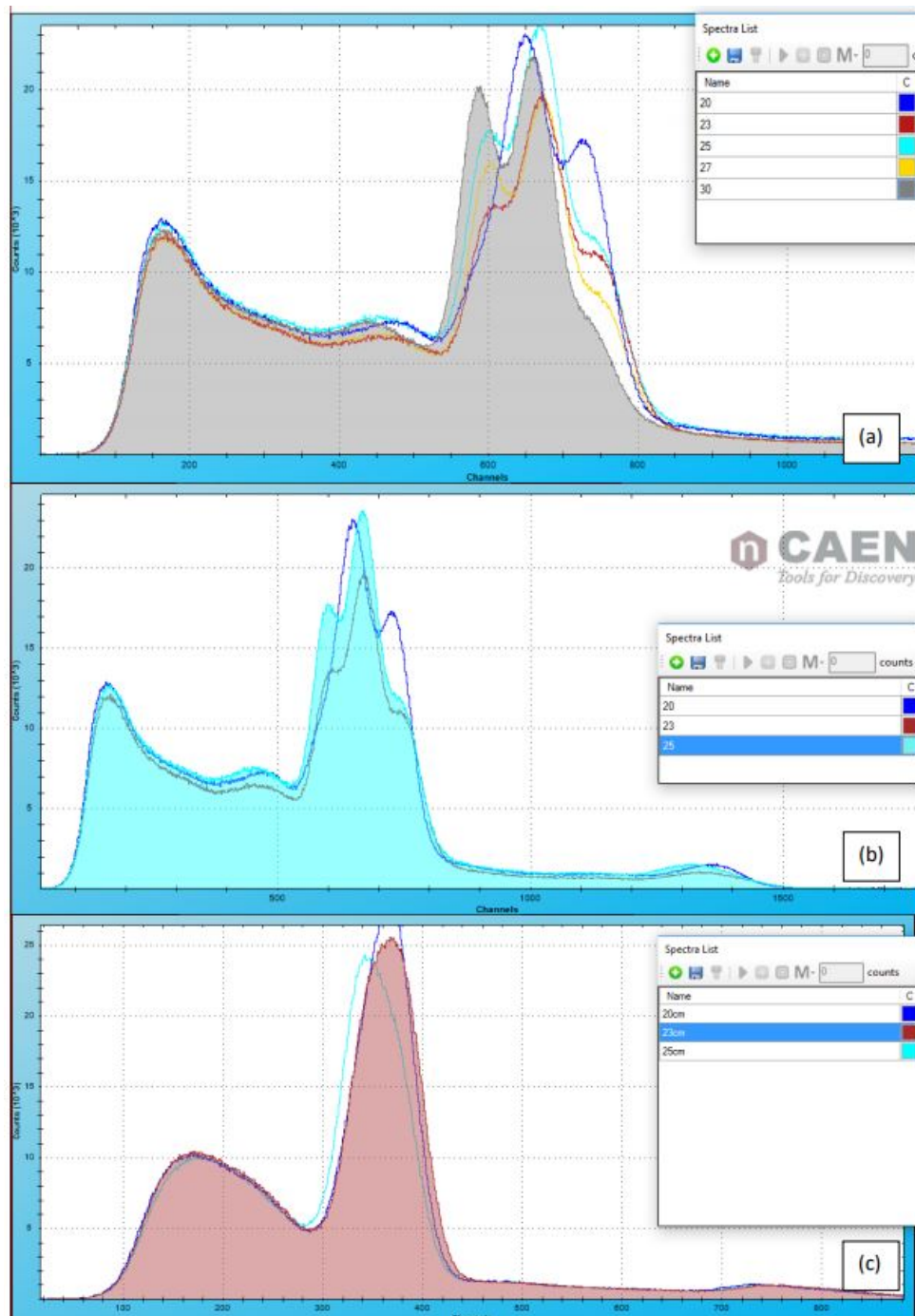
Figure 9.7: *Energy spectra of (a) and (b) ^{60}Co when the source is varied from 20 cm - 30 cm, (c) ^{137}Cs when placed at 20 cm, 23 cm and 25 cm respectively from PMT. In Fig. 9.7(a), one can observe the appearance of three humps or peaks at distances 23 - 27 cm. In Fig. 9.7(c), the 662 keV peak becomes non gaussian and broad at 25 cm distance.*

can be observed that the peaks corresponding to the 1173 keV and 1332 keV are not properly resolved and distorted as shown in Fig. 9.7. At 25 cm, we get three humps or peaks in case of ^{60}Co source. In case of 662 keV, the peak is broad and not perfectly gaussian.

9.7   PMT gain matching

The response of a PMT is strongly dependent on the applied bias voltage. In case of a detector with single PMT, this is less than of an issue. However, for large detectors which comprises of multiple PMTs, the final signal is the summed response of the individual sectors. Whenever, one tube has higher or different gain than the rest, the total response will result in a poor resolution or, in the extreme case, an unrecognisable spectrum. So, it is important to gain match all the PMTs before taking the total response of the detector.

We have used a monoenergetic source ^{137}Cs to gain match the six PMTs to align the single peak positions for a fixed bias. Two power supply module made by CAEN – DT5533EM and DT5533EP have been used to give the bias to each individual PMTs. The high voltage was varied to match the photopeak positions of the six sectors of the SUM spectrometer. The source was placed at 12 cm distance from the PMT at the central axis of the SUM spectrometer. The data have been acquired with DT5730 CAEN digitizer (8 channels, 14 bit, 500 MS/s) with COMPASS software [98].

9.8   Total spectrum of the SUM spectrometer

The total spectrum of the SUM spectrometer was taken in two mode – (1) add mode and (2) addback mode. In add mode, the signals from six sectors are added like a daisy chain to get the added spectrum of the whole array. In addback mode, we take the data of individual detectors in OR condition and then perform the virtual addback in COMPASS software with 400 ns time window. At the time of data acquisition, the source has been placed at a distance of 12 cm from the PMT. The advantage of taking the data in OR condition is that we can make the addback with different conditions like as per time window, multiplicity, *etc*. The total spectra in both
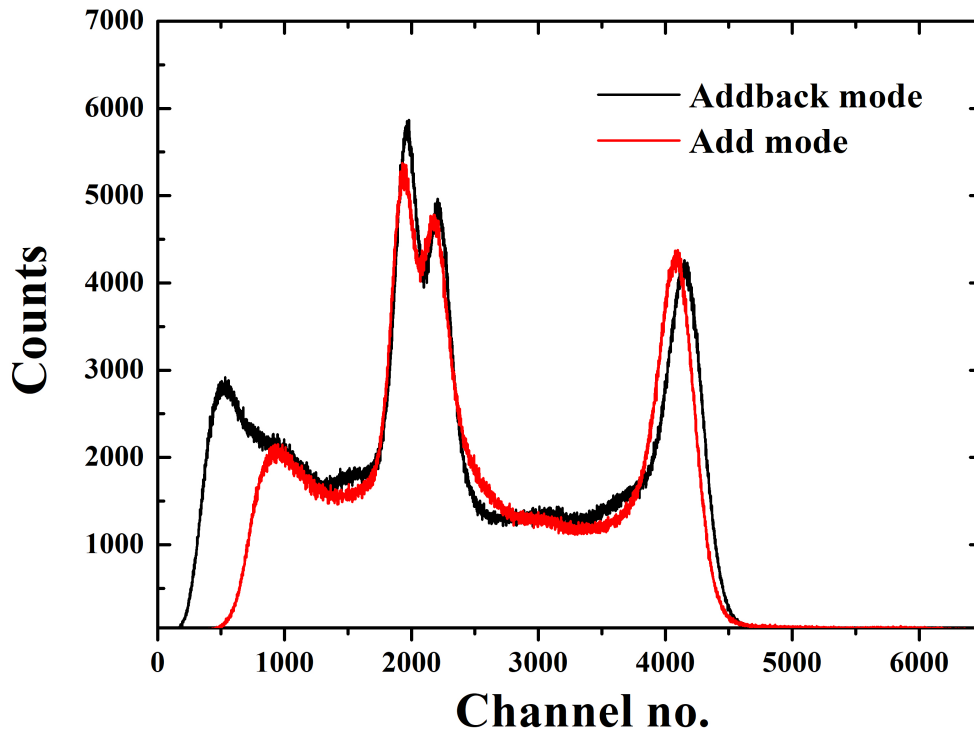
Figure 9.8: *The total summed spectra of the SUM spectrometer at addback mode (black color) and in add mode (red color). The sum peak at (1173+1332) keV has been clearly observed at both the conditions.*

conditions have been shown in Fig. 9.8 for ^{60}Co source. In Fig. 9.8, the summing of 1173-1332 keV peaks, *i.e.*, sum peak of ^{60}Co is clearly observed.

- The behaviour of the SUM spectrometer is not completely clear at certain positions of the source. Now, the sudden change in the resolution and the peak position (as shown in Fig. 9.4, 9.5, 9.7) of different energies may be due to the presence of two crystals in a single detector. When a source is placed at 25 cm or in the middle of the detector (approximately), if it consists of two crystals then it is possible that some of the photons goes in both the crystals leading to shift in the peak position towards the left. So, to resolve this anomalous behaviour or better understanding of the SUM spectrometer characteristics at certain length interval of the detector, we take the help of Monte Carlo simulation which is described in the next section in details.

9.9   GEANT4 simulation model

The GEANT4 simulation toolkit [47] has been used to simulate the response of the SUM spectrometer as accurately as possible. As this model will be used to interpret the experimental data (like energy spectrum, efficiency, *etc*.), so that it needs to reproduce as many features of the detector as possible. The different components of the simulation code have been described briefly below.

9.9.1   DetectorConstruction

In DetectorConstruction class, all the elements and materials used in the simulation are described and built. Starting from the elements such as Na and I, the materials or compounds in the detector have been described (NaI). However, the main problem with building the models of detectors is related to the inability to measure the internal components, especially when there is no documentation. In our case, we have no manual for the SUM spectrometer so that we have to give extra efforts to construct the SUM spectrometer to match the experimental response of the detector. Here, the bulk of the detector volume is consists of NaI material. Then, we have a MgO reflector which surrounds the crystal surface. The detector has a quartz window at one end of the detector. After that, a bialkali photocathode has been attached with the quartz PMT window. The properties of the NaI crystal like scintillation yield, time constant have been included in the simulation code. The optical properties like refractive index, absorption length also have been included in the code to directly simulate the optical photons from scintillation light. The optical physics parameters used in the GEANT4 simulation have been tabulated in Table 9.1. A schematic GEANT4 SUM spectrometer geometry has been given in Fig. 9.9.

9.9.2   PhysicsList and PrimaryGenerationAction

The PhysicsList class basically helps the user to define the properties and behaviour of the particles or photons which will be used in the simulation. There are a wide variety of physics modules

Table 9.1: *List of optical physics parameters which have been used in the present simulation.*

Material	Parameters	Values
NaI(Tl)	Density	3.67 g/cm^3
	Refraction index	1.85
	Absorption length	42.9 cm
	Peak emission	415 nm
	Light yield	38000 photons/keV
	Decay time	230 ns
MgO Reflector	Density	2.0 g/cm^3
	Refraction index	1.0
	Absorption length	1 nm
Bialkali photocathode	Density	2.0 g/cm^3
	Refraction index	1.47
	Absorption length	1 nm
Quartz PMT window	Density	2.20 g/cm^3
	Refraction index	1.47
	Absorption length	3 cm
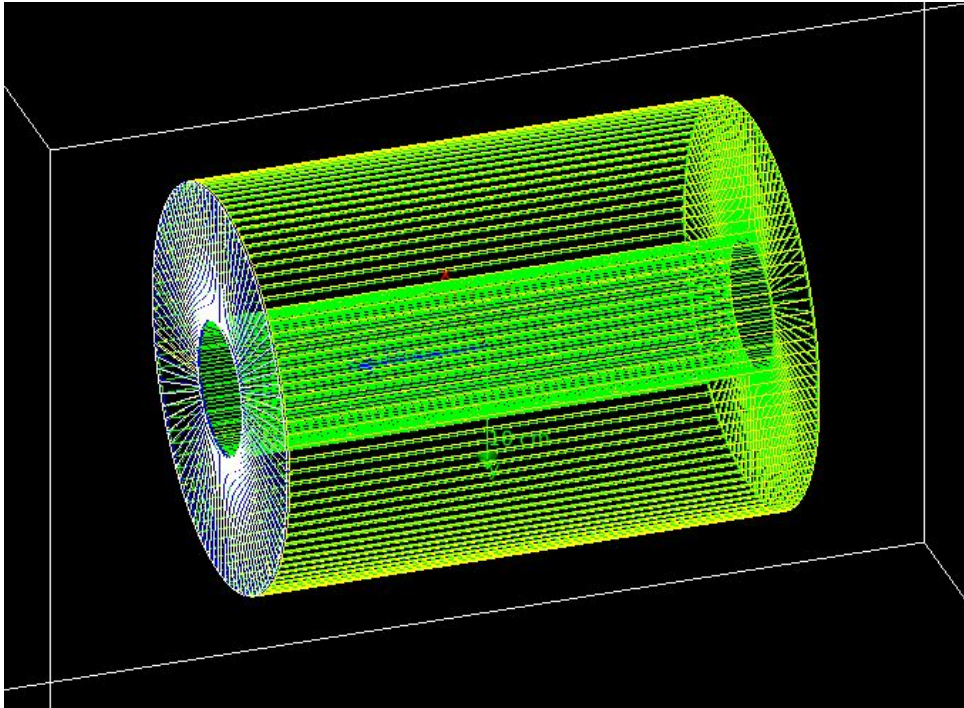
Figure 9.9: *A schematic of the SUM spectrometer geometry which have been used in the GEANT4 [47] simulation.*

available in the GEANT4 toolkit. Here, we have used the standard low energy electromagnetic (EM) physics module. We have also included the Radioactive Decay Module (RDM) and optical physics processes here. The RDM module allows the creation of a radioactive ion as the source of particles. The data contained in the RDM input files are basically from the ENSDF database of NNDC [67]. In this class, we can incorporate the threshold values in terms of default cut value.

The PrimaryGeneratorAction is a mandatory class that defines the method by which particles are generated. There are different classes to define the particles – particle gun and general particle source (GPS). The basic class particle gun can be used to define only monoenergetic particles in a defined direction. However, in GPS class, one can define the energy and direction of the emitted particles fully.

These previously mentioned classes are followed by SteppingAction and EventAction classes. And finally in the RunAction class, the data has been collected and written to an output file.

9.9.3 Simulation of optical photon

To investigate the fundamental reason for the observed characteristics of the SUM spectrometer (like shifting of the photopeak with different source position, anomalous behaviour in between certain length of the detector), two methods have been adopted – (1) energy deposition method, and (2) optical photon method. The optical photon model follows the light produced in the scintillator crystal. Then it tracks the photons until they hit the PMT photocathode. The photocathode is basically used to count the amount of light (number of absorbed photons) that reach the material.

The first observed characteristic, *i.e.*, the shifting of the photopeak positions as a function of source position has been simulated using the optical photon model. It is shown in Fig. 9.10.

But, the second observed property, *i.e.*, the appearance of three humps in between 20 - 30 cm distance cannot reproduce through the simulation till now. As mentioned above, I have considered the single detector is consists of two parts, separated by some optical mediums to
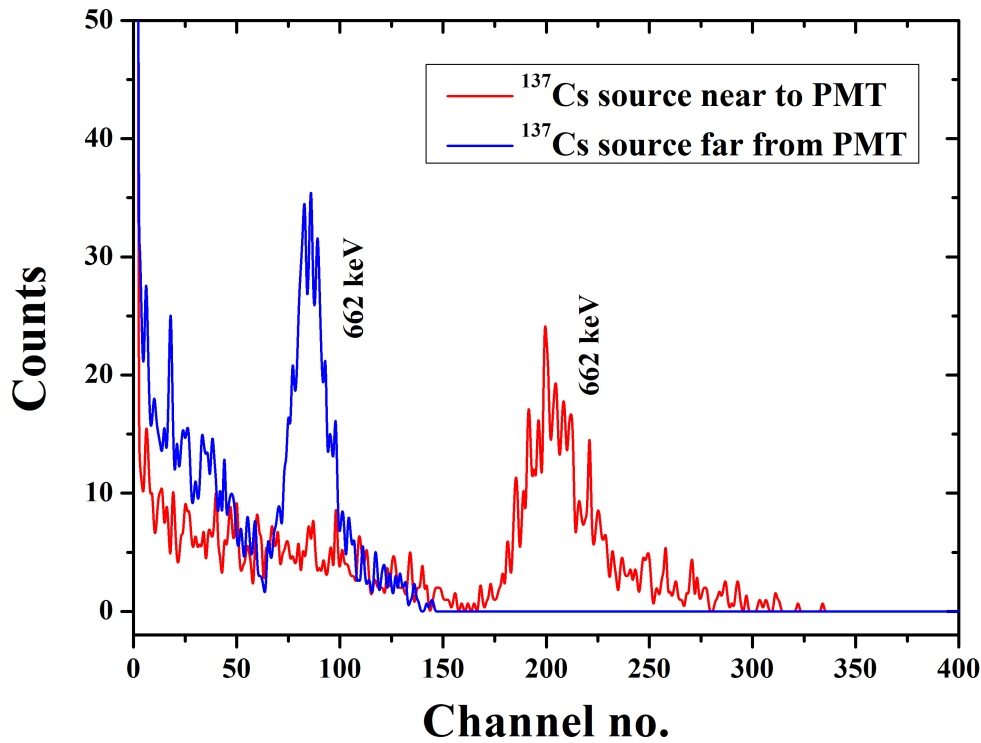
Figure 9.10: *The shifting of the photopeak positions as a function of source position has been simulated using the optical photon model in GEANT4 [47] using the ^{137}Cs source. The source has been placed at two positions near and far from the PMT.*

resolve the anomalous behaviour of the SUM spectrometer. This part of my work is still under process. I am trying to modify the simulation code specially the DetectorConstruction part to reproduce the mentioned characteristics.

9.10 Summary and future plan

Different properties of the SUM spectrometer have been checked through experiment as well as simulation. Few observed properties have to be checked through simulation to properly understand the actual internal geometry of the detector. After resolving this part, our next work is to obtain the correlation between the sum peak efficiency with energy and multiplicity using simulation and experimental data. After getting the efficiency information using laboratory standard sources and well known in-beam reactions, the SUM spectrometer will be effectively

used to study the β-decays for the total decay heat measurements and also for the astrophysical r-process nuclei.

Bibliography

[1] Christian Iliadis, Nuclear Physics of Stars, WILEY-VCH Verlag GmbH $\&$ Co. KGaA, Weinheim, 2007.

[2] kenneth S. Krane, Introductory Nuclear Physics, John Wiley $\&$ Sons Inc., 1988.

[3] Solar fusion cross sections. II. The pp chain and CNO cycles, E. G. Adelberger *et al.*, *Rev. Mod. Phys.*, **2011**, *83*, 195.

[4] C. A. Bertulani *et al.*, Nuclear Reactions, arXiv:0908.3275.

[5] S. M. Daigle, Low energy proton capture study of the ^{14}N(p,γ)^{15}O reaction, PhD thesis, University of North Carolina, Chapel Hill, 2013.

[6] Claus E. Rolfs and William S. Rodney, Cauldrons in the Cosmos, The University of Chicago Press, Chicago and London, 1988.

[7] Thermonuclear Reaction Rates, W. A. Fowler, G. R. Caughlan, and B. A. Zimmerman, *Annu. Rev. of Astron. and Astrophys.*, **1967**, *5*, 525-570.

[8] The Shell-Model Code NuShellX@MSU, B. A. Brown and W. D. M. Rae, *Nuclear Data Sheets*, **2014**, *120*, 115-118.

[9] B. A. Brown *et al.*, http://www.nscl.msu.edu/∼brown/reaction-codes/home.html.

[10] M. Zeilik and S. A. Gregory, Introductory Astronomy & Astrophysics, Harcourt Brace, San Diego, 1998.

[11] Globular cluster ages, R. Jimenez *et al.*, *Proc. Natl. Acad. Sci. USA*, **1998**, *95*, 13-17.

[12] `https://chandra.harvard.edu/edu/formal/variable_stars/bg_`
     `info.html`

[13] Age Estimates of Globular Clusters in the Milky Way : Constraints on Cosmology, L. M. Krauss, B. Chaboyer, *Science*, **2003**, *299*, 65-69.

[14] Planck 2015 results, XIII. Cosmological parameters, Planck Collaboration *et al.*, *Astronomy and Astrophysics*, **2016**, *594*, A13.

[15] CN Cycle Solar Neutrinos and the Sun's Primordial Core Metallicity, W. C. Haxton and A. M. Serenelli, *Astrophysical Journal*, **2008**, *687*, 678-691.

[16] Stellar reaction rate of ^{14}N(p,γ)^{15}O and hydrogen burning in massive stars, U. Schröder, H. W. Becker, G. Bogaert, J. Görres, C. Rolfs, H. P. Trautvetter, R. E. Azuma, C. Campbell, J. D. King, and J. Vise, *Nucl. Phys. A*, **1987**, *467*, 240-260.

[17] The ^{14}N(p,γ)^{15}O low-energy S-factor, C. Angulo and P. Descouvemont, *Nucl. Phys. A*, **2001**, *690*, 755-768.

[18] Astrophysical S-factor of ^{14}N(p,γ)^{15}O, A. Formicola, G. Imbriani, H. Costantini, C. Angulo, D. Bemmerer, R. Bonetti, C. Broggini, P. Corvisiero, J. Cruz, P. Descouvemont, Z. Fülöp, G. Gervino, A. Guglielmetti, C. Gustavino, G. Gyürky, A. P. Jesus, M. Junker, A. Lemut, R. Menegazzo, P. Prati, V. Roca, C. Rolfs, M. Romano, C. R. Alvarez, F. Schümann, E. Somorjai, O. Straniero, F. Strieder, F. Terrasi, H. P. Trautvetter, A. Vomiero, and S. Zavatarelli, *Phys. Lett. B*, **2004**, *591*, 61-68.

[19] S-factor of ^{14}N(p,γ)^{15}O at astrophysical energies*, G. Imbriani, H. Costantini, A. Formicola, A. Vomiero, C. Angulo, D. Bemmerer, R. Bonetti, C. Broggini, F. Confortola, and P. Corvisieros, *Eur. Phys. J. A*, **2005**, *25*, 455-466.

[20] Direct Measurement of the ^{14}N(p,γ)^{15}O S Factor, R. C. Runkle, A. E. Champagne, C. Angulo, C. Fox, C. Iliadis, R. Longland, and J. Pollanen, *Phys. Rev. Lett.*, **2005**, *94*, 082503.

[21] Low energy measurement of the ^{14}N(p,γ)^{15}O total cross section at the LUNA underground facility, LUNA Collaboration, D. Bemmerer, F. Confortola, A. Lemut, R. Bonetti, C. Broggini, P. Corvisiero, H. Costntini, J. Cruz, A. Formicola, Zs. Fülöp, G. Gervino, A. Guglielmetti, C. Gustavino, Gy. Gyürky, G. Imbriani, A. Jesus, M. Junker, B. Limata, R. Menegazzo, P. Prati, V. Roca, C. Rolfs, D. Rogalla, M. Romano, C. Rossi-Alvarez, F. Schümann, E. Somorjai, O. Straniero, F. Strieder, F. Terrasi, H. P. Trautvetter, *Nucl. Phys. A*, **2006**, *779*, 297-317.

[22] First measurement of the ^{14}N(p,γ)^{15}O cross section down to 70 keV, LUNA Collaboration, A. Lemut, D. Bemmerer, F. Confortola, R. Bonetti, C. Broggini, P. Corvisiero, H. Costntini, J. Cruz, A. Formicola, Zs. Fülöp, G. Gervino, A. Guglielmetti, C. Gustavino, Gy. Gyürky, G. Imbriani, A. P. Jesus, M. Junker, B. Limata, R. Menegazzo, P. Prati, V. Roca, C. Rolfs, D. Rogalla, M. Romano, C. Rossi Alvarez, F. Schümann, E. Somorjai, O. Straniero, F. Strieder, F. Terrasi, H. P. Trautvetter, *Phys. Lett. B*, **2006**, *634*, 483-487.

[23] Precision study of ground state capture in the ^{14}N(p,γ)^{15}O reaction, M. Marta *et al.* (LUNA Collaboration), *Phys. Rev. C*, **2008**, *78*, 022802(R).

[24] Cross section measurement of ^{14}N(p,γ)^{15}O in the CNO cycle, Q. Li, J. Görres, R. J. deBoer, G. Imbriani, A. Best, A. Kontos, P. J. LeBlanc, E. Uberseder, and M. Wiescher, *Phys. Rev. C*, **2016**, *93*, 055806.

[25] Lifetime of the 6793-keV State in ^{15}O, P. F. Bertone, A. E. Champagne, D. C. Powell, C. Iliadis, S. E. Hale, and V. Y. Hansper, *Phys. Rev. Lett.*, **2001**, *87*, 152501.

[26] Lifetime measurement of the 6792 keV state in ^{15}O, important for the astrophysical S factor extrapolation in ^{14}N(p,γ)^{15}O, D. Schürmann, R. Kunz, I. Lingner, C. Rolfs, F. Schümann, F. Strieder, and H.-P. Trautvetter, *Phys. Rev. C*, **2008**, *77*, 055803.

[27] Lifetime measurements of states in ^{15}O, N. Galinski, S. K. L. Sjue, G. C. Ball, D. S. Cross, B. Davids, H. Al Falou, A. B. Garnsworthy, G. Hackman, U. Hager, D. A. Howell, M. Jones, R. Kanungo, R. Kshetri, K. G. Leach, J. R. Leslie, M. Moukaddam, J. N. Orce, E. T. Rand, C. Ruiz, G. Ruprecht, M. A. Schumaker, C. E. Svensson, S. Triambak, and C. D. Unsworth, *Phys. Rev. C*, **2014**, *90*, 035803.

[28] ^{14}N(^{3}He,d)^{15}O as a probe of direct capture in the ^{14}N(p,γ)^{15}O reaction, P. F. Bertone, A. E. Champagne, M. Boswell, C. Iliadis, S. E. Hale, V. Y. Hansper, and D. C. Powell, *Phys. Rev. C*, **2002**, *66*, 055804.

[29] E1 strength of the subthreshold 3/2$^+$ state in ^{15}O studied by Coulomb excitation, K. Yamada, T. Motobayashi, H. Akiyoshi, N. Aoi, Zs. Fülöp, T. Gomi, Y. Higurashi, N. Imai, N. Iwasa, H. Iwasaki, Y. Iwata, H. Kobayashi, M. Kurokawa, Z. Liu, T. Minemura, S. Ozawa, H. Sakurai, M. Serata, S. Shimoura, S. Takeuchi, T. Teranishi, Y. Yanagisawa, K. Yoshida, M. Ishihara, *Phys. Lett. B*, **2004**, *579*, 265-270.

[30] An ECR ion source-based low-energy ion accelerator : development and performance, A. N. Agnihotri, A. H. Kelkar, S. Kasthurirangan, K. V. Thulasiram, C. A. Desai, W. A. Fernandez and L. C. Tribedi, *Phys. Scr.*, **2011**, *2011*, 014038.

[31] Characterization of an electrically cooled BEGe detector till E$_\gamma \sim$7 MeV, Sathi Sharma, Arkabrata Gupta, Balaram Dey, M. Roy Chowdhury, A. Mandal, A. Bisoi, V. Nanal, L. C. Tribedi and M. Saha Sarkar, *Nucl. Instrum. Methods Phys. Res. A*, **2020**, *964*, 163810.

[32] Falcon-SS-C0836.pdf, Falcon 5000 Portable HPGe-Based Radionuclide Identifier.

[33] `https://www.mirion.com/products/bege-broad-energy-germanium-detectors`

[34] Characterization of a broad energy germanium detector and application to neutrinoless double beta decay search in ^{76}Ge, M. Agostini, E. Bellotti, R. Brugnera, C. M. Cattadori, A. D'Andragora, A. di Vacri, A. Garfagnini, M. Laubenstein, L. Pandola, and C. A. Ur, *JINST*, **2011**, *6*, P04005.

[35] Characterization of Broad Energy Germanium Detector (BEGe) as a candidate for the GERDA Experiment, Assunta di Vacri, Matteo Agostini, Enrico Bellotti, Carla M. Cattadori, Alessio D'Andragora, Alberto Garafagnini, Matthias Laubenstein, Luciano Pandola, A. Calin Ur, *2009 IEEE Nuclear Science Symposium Conference Record (NSS/MIC), Orlando, FL*, **2009**, 1761-1767.

[36] Najat Ali, Improvement of the Performance of Broad Energy Germanium Detectors for Gamma-ray Spectroscopy, PhD Thesis, University of Liverpool, 2017.

[37] A gamma-ray spectrometry analysis software environment, G. Lutter, M. Hult, G. Marissens, H. Stroh, F. Tzika, *Appl. Radiat. and Isot.*, **2018**, *134*, 200-204.

[38] INGASORT - a new program for the analysis of multi-clover array, Ranjan Bhowmik, S. Muralithar and R. P. Singh, *Proc. DAE-BRNS Symp. Nucl. Phys. (India)*, **2001**, *44B*, 422-423.

[39] Measurement of the $E_r^{c.m.} = 259$ keV resonance in the ^{14}N(p,γ)^{15}O reaction, S. Daigle, K. J. Kelly, A. E. Champagne, M. Q. Buckner, C. Iliadis, and C. Howard, *Phys. Rev. C*, **2016**, *94*, 025803.

[40] G. F. Knoll, Radiation Detection and Measurement, 2nd Edition, John Wiley, New York, 1989.

[41] Evaluated nuclear structure data file, J. K. Tuli, *Nucl. Instrum. Methods Phys. Res. A*, **1996**, *369*, 506-510.

[42] T. K. Alexander *et al.*, Lifetime Measurements of Excited Nuclear Levels by Doppler-Shift Methods, In:Baranger M., Vogt E. (eds) Advances in Nuclear Physics. Springer, Boston, MA.

[43] Proton induced reactions of ^{27}Al at low energies, Sathi Sharma, Arkabrata Gupta, Sangeeta Das, Anik Adhikari, Yajnya Sapkota, Ananya Das, Rajan Paul, Dibyadyuti Pramanik, Abhijit Bisoi, S. Sarkar, and M. Saha Sarkar, *Proceedings of the DAE-BRNS Symp. on Nucl. Phys.*, **2017**, *62*, 280-281.

[44] http://www.gammadata.se/assets/Uploads/BEGe-SS-C49318.pdf

[45] C. Tintori, WP2081 Digital Pulse Processing in Nuclear Physics, Rev. 2.1, (2011); UM2606 DT5780 Dual Digital MCA User Manual, Rev. 4.

[46] https://www.caen.it

[47] GEANT4–a simulation toolkit, S. Agostinelli *et al.*, *Nucl. Instrum. Methods Phys. Res. A*, **2003**, *506*, 250-303.

[48] Proton capture resonant state of ^{15}O at 7556 keV, Sathi Sharma, Arkabrata Gupta, M. Roy Chowdhury, A. Mandal, A. Bisoi, V. Nanal, L. C. Tribedi, M. Saha Sarkar, *Phys. Rev. C*, **2020**, *102*, 024308.

[49] http://cdm-optics.com/e-beam-evaporation-explained/

[50] Rainer Behrisch, Sputtering by Particle Bombardment I, Springer-Verlag Berlin Heidelberg, 1981.

[51] https://www.intechopen.com/online-first/
introductory-chapter-basic-theory-of-magnetron-sputtering

[52] A supersonic jet gas target for γ-ray spectroscopy measurements, H. W. Becker, L. Buchmann, J. Görres, K. U. Kettner, H. Kräwinkel, C. Rolfs, P. Schmalbrock, H. P. Trautvetter, A. Vlieks, *Nucl. Instrum. Methods Phys. Res.*, **1982**, *198*, 277-292.

[53] J. F. Ziegler and J. P. Biersack, computer program SRIM, version 2013 (2013).

[54] Production and characterization of oxygen-reduced ^{21}Ne targets, H. Y. Lee, J. Görres, H.-W. Becker, E. Stech, E. Strandberg and M. Wiescher, *Nucl. Instrum. Methods Phys. Res. B*, **2009**, *267*, 3539-3544.

[55] Production and properties of implanted targets, S. Seuthe, H. W. Becker, A. Krauss, A. Redder, C. Rolfs, U. Schröder, H. P. Trautvetter, K. Wolke, S. Wüstenbecker, R. W. Kavanagh, F. B. Waanders, *Nucl. Instrum. Methods Phys. Res. A*, **1987**, *260*, 33-42.

[56] `http://www.saha.ac.in/web/spd-facilities/`
`spd-ion-beam-systems/spd-isotope-separator-cum-implantor`

[57] `https://srdata.nist.gov/xps`

[58] `http://www.saha.ac.in/web/spd-facilities/spd-microscopy/`
`spd-scanning-electron-microscope`

[59] Bulk characterization of ^{14}N implanted target using Resonance reaction and SIMS measurements, Abhijit Bisoi, L. C. Tribedi, D. Misra, S. Biswas, K. V. Thulasi Ram, M. V. Rundhe, Anoop KV, V. Nanal, and M. Saha Sarkar, *Proceedings of the DAE-BRNS Symp. on Nucl. Phys.*, **2013**, *58*, 994-995.

[60] J. R. Tesmer and M. Nastasi, Eds. Handbook of Modern Ion Beam Materials Analysis. Materials Research Society, Pittsburgh, Pennsylvania, 1995.

[61] Preparation of Gold Target through Electron Vapor Deposition and "Paras" the Rutherford Back Scattering Experimental setup @ IUAC, Sarvesh Kumar, Tulika Sharma, Pranav Bhardwaj, Avnee Chauhan, Shruti Kapoor, and Punita Verma, *National Conference on Inspired Learning (NCIL)*, **2015**, *1*.

[62] M. Mayer, computer program SIMNRA (2011).

[63] Energy levels of light nuclei A = 13-15, F. Ajzenberg-Selove, *Nucl. Phys. A*, **1991**, *523*, 1-196.

[64] Study of ^{14}N(p,γ)^{15}O resonance reaction at E$_p^{lab}$ = 278 keV, Sathi Sharma, A. Gupta, S. Das, M. Roy Chowdhury, A. Mandal, A. Bisoi, V. Nanal, L. C. Tribedi and M. Saha Sarkar, *EPJ Web of Conferences*, **2020**, *227*, 02011.

[65] `http://www.surrey.ac.uk/ati/ibc/files/Suspre.zip`

[66] Resonance strengths of some light nuclei, H. W. Becker, W. E. Kieser, C. Rolfs, H. P. Trautvetter, and M. Wiescher, *Z. Phys. A*, **1982**, *305*, 319-323.

[67] `http://www.nndc.bnl.gov`

[68] Wolfram Research, Inc., Mathematica, Version 12.0.

[69] Shell-model studies of the astrophysical rapid-proton-capture reaction ^{30}P(p,γ)^{31}S, B. A. Brown, W. A. Ritcher, and C. Wrede, *Phys. Rev. C*, **2014**, *89*, 062801(R).

[70] Shell model study of astrophysically important resonant states of ^{15}O, Sathi Sharma and M. Saha Sarkar, *Proceedings of the DAE-BRNS Symp. on Nucl. Phys.*, **2019**, *64*, 588-589.

[71] Study of low energy proton capture resonances in ^{14}N, Rajan Paul, Sathi Sharma, Sangeeta Das, and M. Saha Sarkar, *Student J. Phys.*, **2017**, *6*, 151.

[72] On Closed Shells in Nuclei. II, M. G. Mayer, *Phys. Rev.*, **1949**, *75*, 1969.

[73] On the "Magic Numbers" in Nuclear Structure, O. Haxel, J. Hans, and H. E. Suess, *Phys. Rev.*, **1949**, *75*, 1766.

[74] A potential model representation of two-nucleon data below 315 MeV, T. Hamada, I. D. Johnston, *Nucl. Phys.*, **1962**, *34*, 382-403.

[75] K. Heyde, Basic ideas and concepts in nuclear physics, IOP Publishing Ltd 1994, 1999.

[76] B. A. Brown, Lecture Notes in Nuclear Structure Physics, National Super Conducting Cyclotron Laboratory, 2005.

[77] NuShellX, W. D. M. Rae, `https://www.garsington.eclipse.co.uk`

[78] NuShellX@MSU, B. A. Brown, W. D. M. Rae, E. McDonald and M. Horoi, `http://www.nscl.msu.edu/~brown/resources.html`.

[79] Single-particle $s_{1/2}$ and $d_{5/2}$ states in ^{15}N and ^{15}O, H. T. Fortune, *Phys. Rev. C*, **2016**, *94*, 024339.

[80] Structure of O^{16}, A. P. Zuker, B. Buck and J. B. McGrory, *Phys. Rev. Lett.*, **1968**, *21*, 39.

[81] Shell-Model Calculations for A = 18, 19, and 20 Nuclei with Core Excitation Included Explicitly, *Phys. Rev. C*, **1973**, *7*, 974.

[82] Structure of F^{18} and O^{18}, A. P. Zuker, *Phys. Rev. Lett.*, **1969**, *23*, 983.

[83] Background radiation reduction for a high-resolution gamma-ray spectrometer used for environmental radioactivity measurements, I. Radulescu, A. M. Blebea-Apostu, R. M. Margineanu, and N. Mocanu, *Nucl. Instrum. Meth. A*, **2013**, *715*, 112-118.

[84] Monte-Carlo based background reduction and shielding optimisation for a large hyper-pure germanium detector, R. Britton, J. L. Burnett, A. V. Davies, P. H. Regan, *J Radioanal Nucl Chem*, **2013**, *298*, 1491-1499.

[85] Ultra-sensitive in-beam γ-ray spectroscopy for nuclear astrophysics at LUNA, The LUNA Collaboration, A. Caciolli, L. Agostino, D. Bemmerer, R. Bonetti, C. Broggini, F. Confortola, P. Corvisiero, H. Costantini, Z. Elekes, A. Formicola, Zs. Fülöp, G. Gervino, A. Guglielmetti, C. Gustavino, Gy. Gyürky, G. Imbriani, M. Junker, M. Laubenstein, A. Lemut, B. Limata, M. Marta, C. Mazzocchi, R. Menegazzo, P. Prati, V. Roca, C. Rolfs, C. Rossi Alvarez, E. Somorjai, O. Straniero, F. Strieder, F. Terrasi, and H. P. Trautvetter, *Eur. Phys. J. A* , **2009**, *39*, 179-186.

[86] Muon stopping power and range tables 10 MeV–100 TeV, D. E. Groom, N. V. Mokhov, S. I. Striganov, *Atomic Data and Nuclear Data Tables*, **2001**, *78*, 183-356.

[87] Measurement of gamma radiation background in a low energy accelerator facility, Sathi Sharma, Sangeeta Das, Arkajyoti De, Sudatta Ray, Prajnaparamita Das, Hitesh Rattan, M. Saha Sarkar, *Proceedings of the DAE-BRNS Symp. on Nucl. Phys.*, **2018**, *63*, 1090-1091.

[88] Simulation of the Background for Gamma Detection System in the Indoor Environments of Concrete Buildings, M. Tsutsumi, T. Oishi, N. Kinouchi, R. Sakamoto, M. Yoshida, *J. Nucl. Sci. Tech.*, **2001**, *38*, 1109.

[89] Radioactive atoms: auger-electron, α-, β, γ-, and X-ray data, M. J. Martin and P. H. Blichert-toft, *Nucl. Data Tables A*, **1970**, *8*, 1-12.

[90] Monte Carlo simulations of gamma ray shielding parameters of concretes, Vishwanath P. Singh, A. M. Ali, N. M. Badiger, A. M. El-Khayatt, *Nucl. Eng. Design*, **2013**, *265*, 1071-1077.

[91] https://en.wikipedia.org/wiki/Cosmic_ray

[92] https://www.ortec-online.com/-/media/ametekortec/other/overview-of-semiconductor-photon-detectors.pdf

[93] C. Tintori, WP2081 Digital Pulse Processing in Nuclear Physics, Rev. 2.1 (2011); UM2606 DT5780 Dual Digital MCA User Manual, Rev. 4.

[94] Characterization of NaI(Tl) Sum Spectrometer and its utilization, M. Saha Sarkar, Arkabrata Gupta, Sangeeta Das, Sayantani Datta, Toshali Mitra, Indrani Ray, Yajnya Sapkota, J. Panja, Sujib Chatterjee, *Proceedings of the DAE-BRNS Symp. on Nucl. Phys.*, **2016**, *61*, 1022-1023.

[95] NCRP Report no. 144, Radiation Protection for Particle Accelerator Facilities (2005).

[96] Measurement and simulation of gamma-ray background in a low energy accelerator facility, S. Sharma and M. Saha Sarkar, *JINST*, **2020**, *15*, T09003.

[97] The essential decay of pandemonium: A demonstration of errors in complex beta-decay schemes, J. C. Hardy, L. C. Carraz, B. Jonson, and P. G. Hansen, *Phys. Lett B*, **1977**, *71*, 307-310.

[98] User manual UM5960, CoMPASS, Multiparametric DAQ Software for Physics Applications, Rev. 8 - March 13th, 2019.

[99] Full $0\hbar\omega$ shell model calculation of the binding energies of the $1f_{7/2}$ nuclei, E. Caurier, G. Martinez-Pinedo, F. Nowacki, A. Poves, J. Retamosa, and A. P. Zuker, *Phys. Rev. C*, **1999**, *59*, 2033.

Key word & Thesis Highlight

Every doctoral student needs to submit 'a list of Keywords' & one page Highlight in word document while submitting thesis to HBNI central office for awarding Ph.D. degree.

Highlight needs to have a 'representative colour graphics of the content of the thesis' / 'New Laboratory setup if it is developed as a part of the thesis' with editable caption (Font: Calibri Italics, Size 10). Highlight Text is (Font: Calibri, Size 11) limited to one page with embedded graphics.

Student has to send his/her thesis Keyword (file name: key-enrollment number, eg. key-phys01201404001) and Highlight (file name: high-enrollment number, eg. high-phys01201404001) to HBNI central office by email (Email: highlight@hbni.ac.in) as attachments of two different files with email subject 'keyword and highlight-enrolment number'

A sample page of highlight (with incomplete header) is attached in the next page for convenience.

Student has to submit highlight with completed header.

Thesis Highlights

Name of the Student: Sathi Sharma

Name of the CI/OCC: Saha Institute of Nuclear Physics   **Enrolment No.:** PHYS05201604008

Thesis Title: Study of low energy resonances and β-decay relevant for Nuclear Astrophysics

Discipline: Physical Sciences   **Sub-Area of Discipline:** Nuclear Astrophysics

Date of viva voce: 28-04-2021

My thesis primarily includes both experimental and theoretical studies of low energy resonance reactions. The observed low energy resonance of the $^{14}N(p,\gamma)^{15}O$ reaction is at E_{lab} = 278 keV ($E_{c.m.}$ = 259 keV) which has great influence in the total CNO cycle reaction rate. The largest contribution to uncertainty in the CNO cycle reaction rate is due to the lifetime or energy width of the sub-threshold resonance state of ^{15}O at 6792 keV ($E_{c.m.}$ = - 504 keV). The experiment was performed at TIFR, Mumbai with the proton beam from the ECR machine using an implanted ^{14}N target. In the present work, the implanted target was prepared and characterized (via XPS, SIMS, RBS, etc.) properly before using it at the final experiment. The experimental yield curve has been compared with TRIM and SUSPRE simulation. One of the detectors used in the experiment which is basically an electrically cooled Broad Energy Germanium detector, has been

Figure 1. Full energy peaks for (a) 6172 keV and (b) 6792 keV γ-rays at seven different angles of the BEGe (0°, 25°, 50° and 70°) and HPGe (90°, 120° and 137°) detector respectively.

characterized from 0.122 MeV to 7 MeV using the laboratory standard sources and the in-beam resonance reaction experimental data and also with GEANT4 simulated data. To perform the lifetime measurement, we have adopted the Doppler Shift Attenuation Method (DSAM). The nicely Doppler shifted gamma-rays have been shown in Figure 1. The obtained upper limit of the lifetime of the sub-threshold state 6792 keV is, τ < 1.18 fs and the lower limit of the width of the state is, Γ > 0.56 eV. The lifetime of the other two bound states i.e. at 6172 keV and 5181 keV have also been measured. The evaluated resonance strength (ωγ) value considering the thick target approximation is 12.78 ± 0.29(stat.) ± 0.92(sys.) meV which agrees well with literature value. Theoretical calculations (NuShellX, WSPOT) also have been performed in parallel with the experimental measurements. Theoretical predictions matches well in most of the cases, some disagreements indicate the need of modified interactions in the lower mass regime. The present thesis work also includes the developmental work which has been performed at SINP, Kolkata, India which are directly related to the future experiments using the Facility for Research in low Energy Nuclear Astrophysics (FRENA). The background gamma radiation study will be useful to plan the low energy astrophysics experiments at FRENA. The thesis work includes the characterization of the SUM spectrometer which can be effectively used in β-decay studies of neutron rich nuclei that are produced in the fission reactors and astrophysical r-processes. To understand the observed properties of the SUM spectrometer, Monte Carlo code has been developed using GEANT4 toolkit. Overall, the developmental works will be really effective in designing the future experiments at low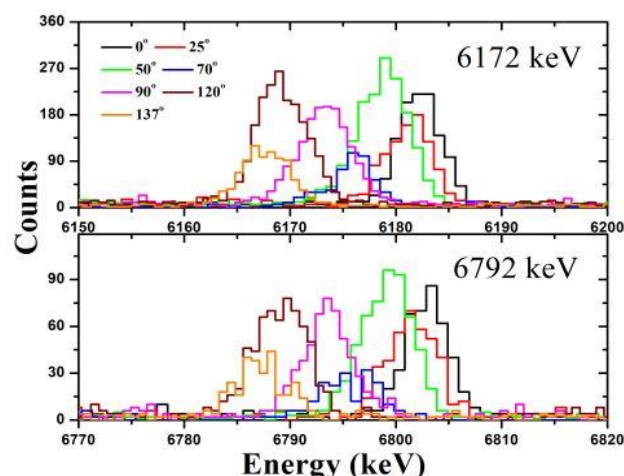 energy accelerator facility FRENA, Kolkata, India.